
Double-Gate Pentacene Thin Film Transistors for Biosensing

Martin Göllner



München 2011

Double-Gate Pentacene Thin Film Transistors for Biosensing

Martin Göllner

Dissertation
an der Fakultät der Physik
der Ludwig-Maximilians-Universität
München

vorgelegt von
Martin Göllner
aus München

München, den 23.12.2011

Erstgutachter: PD. Dr. B. Nickel

Zweitgutachter: Prof. Dr. L. Schmidt-Mende

Tag der mündlichen Prüfung: 29.02.2012

Contents

Zusammenfassung	xiii
Summary	xv
1 Introduction	1
1.1 Motivation and Outline	1
1.2 Basic Principles of Electrochemical Biosensing Devices	2
1.2.1 Devices	3
1.2.2 Surface Architecture	7
2 Organic Field Effect Devices	9
2.1 Basic Principles of Semiconductor Physics	9
2.1.1 The Energy-Band Model	9
2.1.2 Semiconductor Interfaces	12
2.2 The Thin Film Transistor	18
2.2.1 Basic Principle	18
2.2.2 Current-Voltage Characteristics	19
2.2.3 Characteristic Parameters	21
2.3 The Double-Gate Thin Film Transistor	23
2.3.1 Basic Principle	23
2.3.2 Current-Voltage Characteristics	26
2.4 Organic Semiconductors	31
2.4.1 Structural Properties	31
2.4.2 Electronic Properties	32
3 Electrochemistry of Semiconductor-Electrolyte Interfaces	37
3.1 Basic Principles of Electrochemistry	37
3.1.1 The Electrochemical Potential	37
3.1.2 The Potential of Electrodes	38
3.1.3 The Surface of Semiconductor Electrodes	41
3.1.4 Electrode Reactions	43
3.2 Electrochemical Methods	48
3.2.1 The Potentiostat	48

3.2.2	The Current in an Electrochemical Experiment	49
3.2.3	Potential Step Methods	51
3.2.4	Voltammetry	52
3.2.5	Impedance Spectroscopy	54
4	Materials	59
4.1	The Organic Semiconductor Pentacene	59
4.1.1	Structural and Electronic Properties	59
4.1.2	Thin Film Growth	60
4.2	The Alkane Tetratetracontane	63
4.2.1	The TTC-Effusion-Cell	63
4.2.2	Characterization of Tetratetracontane Thin Films	65
4.3	Characterization of the Dielectric Layer	75
5	Electrochemical Characterization of Organic Semiconductor Interfaces	77
5.1	Setup	77
5.2	Transient Measurements	78
5.3	Cyclic Voltammetry Measurements	82
5.3.1	Experimental	82
5.3.2	Discussion	84
5.4	Impedance Measurements	86
6	Transducer Devices based on Double-Gate Thin Film Transistors	89
6.1	Sample Preparation	90
6.1.1	Substrates	90
6.1.2	Cleaning Methods	90
6.1.3	Fabrication of DGTFTs	91
6.2	Setup	94
6.3	Stable Operation in Aqueous Ionic Solutions	95
6.3.1	Performance for Floating Electrolyte Potential	95
6.3.2	Electrolyte Gating of Double-Gate Thin Film Transistors	98
6.4	Sensing of Fatty Acid Molecules	101
6.4.1	Bottom-Gate Voltage Sweep Method	101
6.4.2	Top-Gate Voltage Sweep Method	103
6.4.3	Drain-Voltage Step Method	103
6.4.4	Discussion	105
6.5	Lipid Membranes as a Potential Biofunctionalization Concept	107
6.5.1	Formation of a Lipid Membrane on TTC	107
6.5.2	Sensing of a Lipid Membrane by a DGTFT Transducer	108
7	Conclusion and Outlook	111
	Bibliography	113

Contents	vii
Publications	121
Danksagung	123
Lebenslauf	125

List of Figures

1.1	Schematic of a DGTFT transducer device	2
1.2	Basic principle of a biosensing device	3
1.3	Amperometric techniques	4
1.4	Change of potential in potentiometric devices	6
1.5	Direct and indirect transduction	7
1.6	Adhesion of cells on a lipid membrane	8
2.1	MS junction	13
2.2	Surface space-charge region of a MIS junction	14
2.3	Energy band diagrams of a MIS junction	15
2.4	The surface charge of a MIS junction	16
2.5	Dangling states and ion-induced states	17
2.6	Bottom-contact and top-contact TFT	18
2.7	Linear and saturation regime of a TFT	19
2.8	Characteristic parameters of a TFT	22
2.9	Schematic of a DGTFT	23
2.10	Basic principle of a DGTFT	24
2.11	Operation modes of a DGTFT	24
2.12	Current-voltage characteristic of a DGTFT	25
2.13	Shift of the threshold voltage of a DGTFT	28
2.14	Depletion width and Debye length vs charge carrier concentration	29
2.15	Influence of the depletion width on the threshold voltage shift of a DGTFT	30
2.16	The two threshold voltage regimes of a DGTFT	31
2.17	Chemical structure of common organic semiconductors	32
3.1	Energy level diagram of a charged particle	38
3.2	Anode and cathode in an electrochemical cell	39
3.3	Scheme of a standard hydrogen electrode	40
3.4	Triple-layer model of the electric double layer	41
3.5	Contact adhesion of an ion to a semiconductor	42
3.6	Equivalent circuit of electric double layer with surface states	43
3.7	Distribution of the electron state density of hydrated redox particles	45
3.8	Redox electron transfer reaction	45

3.9	Charge transfer between a semiconductor and a redox system	46
3.10	Band bending of a p-type semiconductor in contact to a redox system . . .	47
3.11	Basic principle of a potentiostat	49
3.12	The Butler Volmer Equation	51
3.13	Single Potential Step experiment	52
3.14	Linear Voltammetry	53
3.15	Cyclic Voltammetry	53
3.16	The complex impedance plane	54
3.17	Impedance Spectroscopy of a single resistor or capacitance	55
3.18	Impedance Spectroscopy of a resistor and capacitance in series or in parallel	56
3.19	Equivalent circuit of a typical electrochemical cell	57
4.1	Photograph of the UHV evaporation chamber	60
4.2	Screenshot of LabView program for molecular beam deposition	61
4.3	Herringbone structure of pentacene	61
4.4	AFM micrographs of pentacene thin films	62
4.5	Structure of tetratetracontane	63
4.6	Evaporation cell	64
4.7	Molecular beam evaporation	64
4.8	Growth of TTC for low deposition rate and room temperature	65
4.9	Growth of TTC for low deposition rate and 370 K	66
4.10	Growth of TTC for high deposition rate and 370 K	67
4.11	Growth of TTC for high deposition rate and room temperature	68
4.12	X-ray Reflectometry Measurements of TTC thin films	70
4.13	Standing and lying phase of TTC	71
4.14	X-ray Reflectometry Measurements of substrates modified by SAMs . . .	71
4.15	Setup for Leakage Current Measurements	72
4.16	Leakage Current Measurements for pentacene capped by TTC	73
4.17	Contact Angle Measurement of a Water Drop on TTC	74
4.18	Penetration of sodium ions into silicon dioxide	75
4.19	Effect of COC on the dielectric layer in an ionic environment	76
5.1	Design of self-made electrochemical cell	78
5.2	Photograph of shielding box for electrochemical measurements	79
5.3	Transient measurements of organic thin films	80
5.4	Cyclic voltammetry measurements of organic thin films	83
5.5	The pentacene-electrolyte interface	85
5.6	Impedance spectroscopy measurements of organic thin films	87
6.1	Basic principle of a DGTFT sensor device	89
6.2	Tools for the fabrication of DGTFTs	91
6.3	Fabrication steps of DGTFTs	93
6.4	Currents occurring at a DGTFT transducer device	94

6.5	Setup for the characterization of DGTFTs	95
6.6	Performance of uncapped pentacene TFT in DI water	96
6.7	Performance of capped pentacene TFT in 1 mM NaCl solution	97
6.8	Performance of DGTFTS in aqueous ionic environment	99
6.9	Correction of the top-gate transfer curve	100
6.10	Sensing of hexanoic acid by bottom-gate voltage sweep method	102
6.11	Sensing of stearic acid by top-gate voltage sweep method	104
6.12	Sensing of stearic acid by potential step method	105
6.13	Energy band diagram of a MIS-Schottky barrier	107
6.14	Continuous bleaching of a lipid membrane on a TTC surface	109
6.15	Influence of lipid membrane formation on DGTFT transfer curve	110

Zusammenfassung

Organische Elektronik hat unlängst Marktreife erlangt und könnte schon bald konventionelle Halbleiter-Elektronik im Bereich kostengünstiger, flexibler und leichtgewichtiger Anwendungen ergänzen. Während organische Leuchtdioden (engl. OLEDs) bereits eine Nische im Markt für mobile elektronische Geräte gefunden haben, werden organische Dünnschicht-Transistoren (engl. OTFTs) und organische photovoltaische Zellen (engl. OPVCs) gerade erst interessant für kommerzielle Anwendungen. Ein neuer, ungewöhnlicher Ansatz ist es, organische Elektronik in der Medizin zu benutzen, speziell in dem Gebiet der Biosensoren. Insbesondere die überlegene Biokompatibilität vieler organischer Materialien prädestiniert organische Sensoren für *in vivo* Anwendungen. In den letzten Jahren hat sich der Fokus auch auf Sensorkonzepte gerichtet, die auf Feldeffekt-Transistoren beruhen. Der wichtigste Vorteil dieses Ansatzes ist nicht nur die geringe Nachweiszeit, sondern auch die intrinsische Verstärkung des Signals, welche weitgehend unabhängig von der Größe der Sensor-Oberfläche ist. Außerdem können organische Transistoren auf flexiblen oder biologisch abbaubaren Substraten prozessiert werden. In den meisten Arbeiten, welche in diesem Fachgebiet publiziert wurden, befindet sich die zu analysierende Lösung in direktem Kontakt zu einem organischen Halbleiter. Jedoch können an dieser Grenzfläche, neben Fallenzuständen oder Dotierungs-Effekten, viele komplexe, elektrochemische Prozesse auftreten, weshalb der Ursprung des Transducer-Signals in der Regel wenig verstanden ist.

Der Ansatz dieser Arbeit ist es, einen Transducer zu entwickeln, der auf einem organischen Double-Gate Dünnschichttransistor (engl. DGTFT) basiert. Hierbei dient das Bottom-Gate als konventioneller Gate-Kontakt, während ein Elektrolyt das Top-Gate darstellt. Eine Änderung des Elektrolytpotentials oder die Adsorption geladener Teilchen an der Grenzfläche zum Elektrolyten bewirkt eine Änderung des Stroms zwischen Source und Drain. Der Vorteil dieses Konzeptes ist, dass eines der Gates benutzt werden kann, die Transfer-Charakteristik zu bestimmen, während das andere Gate die Einstellung des Arbeitspunktes ermöglicht. Transducer, welche auf dem Prinzip der kapazitiven Kopplung basieren, haben das Potenzial sowohl Konzentrationsänderungen eines geladenen Analyten, als auch Aktions- oder Rezeptorpotentiale lebender Zellen zu detektieren.

Das erste Ziel dieser Arbeit war es, ein organisches Top-Gate Dielektrikum zu implementieren und zu charakterisieren. Unsere Wahl fiel hierbei auf die Gruppe der Alkane, da diese bekanntlich gute isolierende Eigenschaften besitzen, sehr hydrophob sind und im elek-

trischen Feld kaum polarisiert werden. Wir entschieden uns, das langkettige Alkan Tetratetracontan zu verwenden, da dessen Schmelzpunkt weit über der Raumtemperatur liegt und kristalline Filme bildet, wenn es mittels Molekularstrahldeposition aufgebracht wird. Durch Änderung der Aufdampfparameter, basierend auf der Charakterisierung der Struktur mittels Rasterkraftmikroskopie, Röntgen-Reflektometrie, Kontaktwinkel-Messungen, sowie Strom-Spannungs-Messungen, wurden die Isolatoreigenschaften von Tetratetracontan optimiert. Zusätzlich wurde die Elektrochemie des Alkans und des organischen Halbleiters Pentacen durch zyklische Voltammetrie sowie Transienten- und Impedanz-Messungen untersucht. Die Resultate dieser Messungen ermöglichten es, einen Pentacen DGTFET mit einem Tetratetracontan Top-Dielektrium mit einer Kapazität von $2.6 \cdot 10^{-8} \text{ F cm}^{-2}$ in einer wässrigen, ionischen Lösung stabil zu betreiben. Die Mobilität des DGTFETs in wässriger Lösung war in der Größenordnung von $10^{-2} \text{ cm}^2/(\text{Vs})$.

Das zweite Ziel war es, das Transducer-Prinzip zu demonstrieren. Dies kann entweder durch Änderung des Elektrolytpotentials geschehen oder durch die Adsorption geladener Teilchen an der Grenzfläche. Es gelang uns, die Transfer-Charakteristik durch das Potential einer Elektrode zu kontrollieren. Im Detail bedeutet dies, dass es möglich ist über das elektrochemische Potential des Elektrolyten sowohl eine Akkumulation von Löchern im Transistorkanal zu erzeugen, als auch eine vollständige Verarmung der Halbleiterschicht herbeizuführen. Zusätzlich kann die Threshold-Spannung mittels der Bottom-Gate Spannung eingestellt werden. Des Weiteren zeigten wir, dass die Anlagerung von Fettsäure Molekülen an der Grenzfläche eine Verschiebung der Threshold-Spannung bewirkt. Hierbei erreichten wir eine Konzentrations-Empfindlichkeit im Bereich von 10 nM .

Schließlich gelang es uns, eine homogene und fluide Lipidmembran auf die Oberfläche des Transducers aufzubringen und das daraus resultierende Signal zu messen. In Zukunft soll die Funktionalisierung der Lipidmembran eine Selektivität des Sensors ermöglichen.

Summary

Organic electronics has recently reached marketability and may soon complement conventional semiconductor electronics in the field of low-cost, lightweight and flexible applications. While organic light-emitting diodes (OLEDs) for efficient and bright displays have already found their niche in the market of mobile electronic appliances, organic thin-film transistors (OTFTs) and organic photovoltaic cells (OPVCs) have just started to become interesting for commercial applications. A new and more unconventional approach is the use of organic electronics in medical science, in particular in the field of biosensing. Here, especially the superior biocompatibility of many organic materials predestine organic sensing devices for *in vivo* applications. In the last few years the focus of interest has also been directed on sensing concepts based on organic field-effect transistors (OFETs). The main advantage of this technology is not only a fast analysis time, but also the intrinsically amplified signal, which is largely independent from the size of the sensing area. Additionally, organic transistors can be processed on flexible and biodegradable substrates. In most works presented so far in this field the analyte solution is in direct contact to an organic semiconductor. However, due to many complex electrochemical processes which can occur at this interface as well as trapping or doping effects, the origin of the transducer signal is generally not well understood.

The approach of this thesis is to realize a transducer device which is based on an organic double-gate thin film transistor (DGTFT). Here, the bottom-gate represents the conventional gate contact, while an electrolyte acts as the top-gate. A change in the potential of the electrolyte or the adsorption of charged particles at the interface with the electrolyte results in a change of the source-drain current. The advantage of this concept is that one of the gates can be used to determine the transfer characteristics, while the other gate allows for the adjustment of the working point. Transducers based on the concept of capacitive coupling have the capability to detect changes in the concentrations of charged analytes as well as action or receptor potentials of living cells.

The first scope of this work was to implement and characterize an organic top-gate dielectric. Here, the choice fell on alkanes, as they are known for good insulating properties, they are very hydrophobic and only marginal polarized in electric fields. We selected the long-chain alkane tetratetracontane, because of its melting point far above room temperature and its feature to form crystalline films when grown by molecular beam deposition.

The sealing properties of tetratetracontane were optimized by changing the deposition parameters based on the characterization of the structure by atomic force microscopy, X-ray reflectometry, contact angle measurements and current-voltage measurements. Additionally, we investigated the electrochemistry of the alkane and the organic semiconductor pentacene by transient, cyclic voltammetry and impedance measurements. The attained findings allowed for a stable performance of a pentacene double gate transistor with a tetratetracontane top gate dielectric with a capacitance of $2.6 \cdot 10^{-8} \text{ F cm}^{-2}$ in an ionic aqueous environment. The mobility of the OTFT in aqueous solution was in the range of $10^{-2} \text{ cm}^2/(\text{Vs})$.

The second aim was to demonstrate the transducer principle. This can either occur by changing the potential of the electrolyte or by the adsorption of charged particles to the interface. We succeeded to control the transfer characteristics by the potential of an electrode. In detail, this means that it is possible to achieve both an accumulation of holes in the transistor channel and the full depletion of the semiconducting layer by the electrochemical potential of the electrolyte. Additionally, the threshold voltage can be adjusted by the bottom-gate voltage. Moreover, we showed that the adhering of small quantities of fatty acid molecules to the interface, results in the a shift of the threshold voltage. Here, we reached a concentration sensitivity in the range of 10 nM .

Finally, we managed to establish a homogeneous and fluid lipid membrane on top of the transducer device and measure the resulting signal. In the future the functionalization of the lipid membrane may allow for selectivity of the sensor device.

Chapter 1

Introduction

1.1 Motivation and Outline

The cognition of the environment by bioanalysis has played a crucial role in the development of life and has reached an astonishing level of complexity and precision. The sensory organs of living organisms are not only capable to detect tiny changes in electromagnetic fields, [1] temperature, pressure, or gradients in the concentration of chemicals, [2, 3] but also trace amounts of biochemicals like enzymes in highly complex systems [4]. Inspired by the recognition systems of nature, in the middle of the 20th century scientists started to develop a new type of sensor device, namely the biosensor, which is based on the combination of biorecognition elements and a transduction method. The most notably starting signal for biosensing research was given by the invention of the oxygen electrode by Leland C. Clark in 1956 [5], leading to the development of the first glucose oxidase sensor in 1962. [6] Since that time, research has made remarkable progress and a multitude of diagnostic devices based on biosensing technologies has entered the market. However, except for the glucose sensor, these biosensing devices are mainly too large, expensive and difficult to handle for laity. Electrochemical sensing concepts have the potential to overcome these difficulties, as they can be produced in micro- or even nanoscale dimensions and allow for a straightforward interfacing to electronic processing and read-out devices. However, the use of biosensing devices in biological relevant environments, e.g. the human body, are still subject to severe limitations. The recent advances in the development of biocompatible materials may play a key role to resolve these issues. [7, 8] Here, the use of organic materials is of special interest, since they can be processed on flexible substrates, [9–11] are non-toxic and offer a soft ambient for living cells [12, 13]. In section 1.2 the basic principles of electrochemical biosensing devices are discussed with special emphasis on the advantage of organic materials.

In this work an electrochemical transducer device is presented, which is based on an organic double-gate thin film transistor (DGTFT) and allows for the detection of biochemical reactions involving charged particles, see Fig. 1.1. Here, the conventional bottom-gate is re-

alized by a highly doped silicon substrate and the top-gate is represented by an electrolyte. While the bottom-dielectric is a silicon dioxide layer, the top-dielectric was accomplished by a thin alkane layer, namely tetratetracontane. The good sealing properties of the alkane layer allow for a high sensitivity of the transducer device and its inert nature is an ideal prerequisite for the development of a biosensing device. Due to its superior electronic properties we chose the organic semiconductor pentacene for the semiconducting layer.

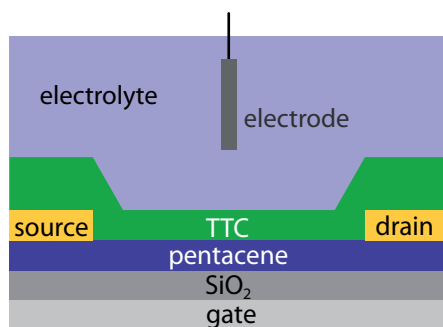


Figure 1.1: Schematic of a DGTFT transducer device.

To realize such a transducer device it is inevitable to overcome two main challenges. First, one has to transfer the theory for inorganic DGTFT devices, which generally operates in the inversion regime, to organic DGTFTs, which operate in the accumulation mode. Beside the basics of organic semiconductors the theoretical background of DGTFTs will be the topic of chapter 2. Secondly, the electrochemistry occurring at the interfaces of organic materials and ionic aqueous solutions is still poorly understood. The basic principles of the electrochemistry of semiconductor electrodes and of the electrochemical techniques are treated in chapter 3. The organic materials used for the transducer device are discussed in chapter 4 and their electrochemical characterization is presented in chapter 5. In chapter 6 we show that the understanding of these two topics allows for a stable operation of an organic DGTFT in an aqueous ionic environment and we demonstrate the sensing principle. The latter was accomplished by detecting fatty acid molecules. Finally, we propose a new approach for the functionalization of the sensor device.

1.2 Basic Principles of Electrochemical Biosensing Devices

The intention of this section is to give the reader a short overview of the vast field of electrochemical biosensing and accent the significance of organic electronics.

The basic principle of a biosensor is to transduce a recognition event, originating from an biological element or response, into a quantifiable signal. [14, 15] Here, for medical applications it is essential to detect small analyte concentrations in the μM or even fM

scope. [16] However, for more sophisticated concepts it also may be volitional to detect e.g. the activity of single living cells at the detector interface. [17] As shown in Fig. 1.2, electrochemical biosensors typically consist of four parts: A bioreceptor which specifically binds to the analyte, a transducer which converts the event into an electronic signal, an amplifier and a facility for the electronic readout, including data acquisition, processing and an interface to the user. [18]

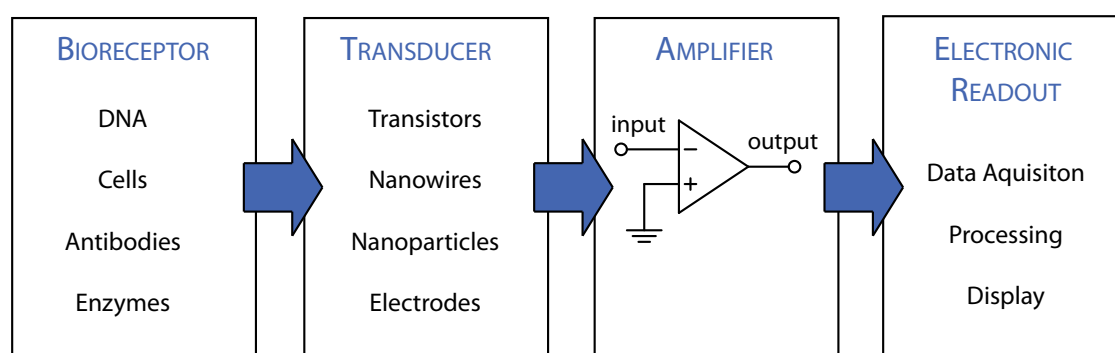


Figure 1.2: Scheme of the basic principle of a biosensing device.

Nevertheless, electrochemical biosensors still suffer from several teething troubles, especially expensive fabrication costs and poor biocompatibility. According to Heiduschka et al. an implant is biocompatible when it does not evoke a toxic, allergic or immunologic reaction, not harm or destroy enzymes, cells or tissues, not cause thrombosis or tumours, and remains for a long term within the organism without encapsulation or rejection. [8] Here, the use of organic materials can provide a decisive contribution, as they can be processed at low costs on highly flexible, soft substrates. Hence they show a superior biocompatibility and even permit the design of biodegradable sensor devices [19, 20], e.g. for in vivo applications. Moreover, the unique properties of organic materials may open up new chances for the design of novel surface architectures. Therefore, in the first part of this chapter the different concepts of electrochemical biosensing, namely amperometric, conductometric and potentiometric techniques, will be discussed and in the second part a variety of surface architectures will be presented.

1.2.1 Devices

The current signal of a biosensing device originates either from a change of the potential at the interface, from a change in the resistance or from a charge transfer. The corresponding devices are termed potentiometric, conductometric and amperometric devices. [21] However, for some sensor devices the division in these categories is not clearly assignable. For example sensors based on impedance spectroscopy can be ranked in all three categories.

Amperometric Devices

Amperometric biosensors term electrochemical devices which measure the current originating from redox reactions of certain species in a biochemical reaction. [22] Here, an electron transfer between a catalytic molecule (e.g. oxidase), dissolved in an electrolyte and a working electrode occurs. While, in the simplest case, the potential of the electrolyte is set to a constant value and the response to an injected analyte is measured, more sophisticated approaches apply an alternating bias. For example in *Chronoamperometry* a square-wave potential is applied at the working electrode, in *Cyclic Voltammetry* the potential is swept linearly between two values at a fixed rate and in *Impedance Spectroscopy* a constant DC-voltage is superposed with a small sinusoidal AC-voltage. A schematic overview of the applied potentials and typical output curves is given in Fig. 1.3.

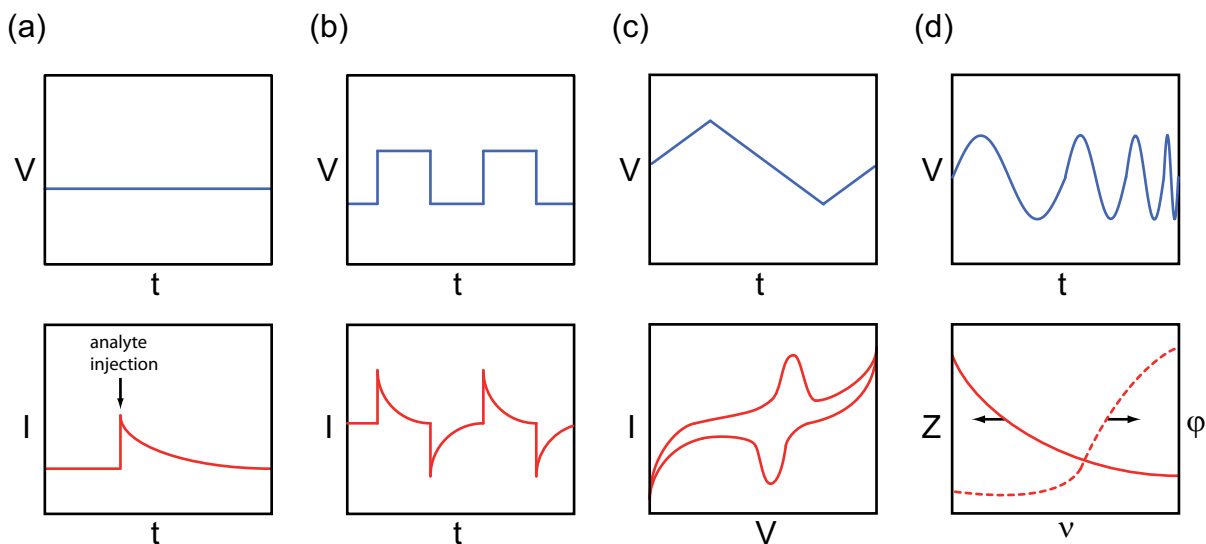


Figure 1.3: Schematic of applied voltages with corresponding output curves for (a) Simple Amperometry, (b) Chronoamperometry, (c) Voltammetry and (d) Impedance Spectroscopy.

The most simple example for such a sensing device is the glucose sensor based on measuring the amount of oxygen consumed by the enzyme glucose oxidase. [6] The current is resulting from the reduction of oxygen at a platinum electrode and thus is proportional to the oxygen concentration in an electrolyte solution. Generally, the performance of this type of sensor is enhanced by the use of conducting polymers for enzyme immobilization, e.g. polypyrrole. [22] An impressive example of how the response can be significantly improved by the use of organic materials is given by the work of Muguruma et al. [23]. Here, a composite electrode made of single-walled carbon nanotubes, a plasma-polymerized thin film and the enzyme glucose oxidase allows for a sensitivity of $42 \mu A m M^{-1} cm^{-2}$ for glucose.

Conductometric Devices

This type of biosensors measures the electrical conductivity of an analyte or a medium. Basically they can be divided in two different designs: The most common class of conductometric devices measures the change of conductivity of a solution between two electrodes due to an enzymatic reaction, which changes the concentration of charged species. A second, usually more complex, class of conductometric techniques is based on the change of conductance of an electrode. This change can be generated e.g. by immobilization of charged molecules like enzymes or antibody-antigen-pairs. The recent trend goes to the use of electronic devices and structures in the micro- and nanoscale, like nanowires [24] or transistor devices. Particularly the latter can profit from the use of organic semiconductors, which allow for tunable material properties and good capabilities for functionalization. In this line the group of G. Malliars developed organic electrochemical transistors (OECTs) for enzymatic sensing. [25] Here the degenerately doped p-type organic semiconductor poly 3,4-ethylenedioxythiophene doped with polystyrenesulfonate (PEDOT:PSS) is de-doped by the penetration of positive ions from the electrolyte, resulting in a change of the conductivity. Thereby, due to an enzyme reaction the positive ion concentration is directly proportional to the glucose concentration.

Potentiometric Devices

Traditionally potentiometric devices were regarded inferior to amperometric devices in performance and sensitivity. However, recent development has shown that this class of sensors has the potential to combine a more direct sensing mechanism with a sub-nanomolar limit of detection. [26] Potentiometric sensor devices monitor the change in potential between a working electrode and a reference electrode in an electrochemical cell, when negligible current flows between them. [18] The change in potential can either result from a change of the bulk potential or from a change of the surface potential, e.g. due to the accumulation of charged species (see Fig. 1.4). In the former case the bulk potential is controlled by an electrode or determined by the ion concentration. Here, the cell potential V is associated to the concentration of charged species via the Nernst equation:

$$V = V^0 + \frac{kT}{ze} \ln \frac{C_a}{C_c} \quad (1.1)$$

where k is the Boltzmann constant, T the absolute temperature in Kelvin, z the charge number of the electrode reaction, e the elementary charge and C_a/C_c is the ratio of the concentration of the charged species at the anode to the concentration at the cathode. V^0 is the formal potential (the cell potential at which $C_a/C_c = 1$). [27] In the most simple case, the direct potentiometry, the Nernst-Equation (Eq. 1.1) is directly used for the determination of an ion concentration. Following a similar concept, in potentiometric titration the potential is changed by titration of ions until an equilibrium has established and zero or constant current is reached.

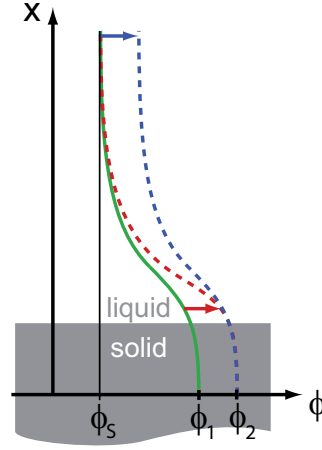


Figure 1.4: Schematic of the change of potential at a solid-liquid interface in a potentiometric device. A shift of the potential from ϕ_1 (green curve) to ϕ_2 can either originate from a change of the bulk potential ϕ_S (blue curve) or from a change of the surface potential (red curve), due to charge build-up.

A device utilizing the change of the surface potential is the ion-selective field-effect transistor (ISFET). [28,29] Here, the analyte solution acts as a gate electrode, which is separated from the semiconductor by an insulating layer which is sensitive to hydrogen ions. A typical material for such an ion sensitive layer is SiO_2 , where the hydrolysis of S-OH groups gives rise to a change of the effective gate voltage and hence a change of the threshold voltage. This technique is commonly used for pH-sensing. In an enzymatically coupled ion-sensitive field effect transistor (ENFET) the principle mentioned above is modified by immobilizing a suitable enzyme layer over the gate dielectric surface. [30]

In the last few years sensor architectures based on capacitive coupling have shown a substantial progress, and even allow for the read out of the action potential of single cells. [31] One of the main advantages of the use of field effect transistors (FETs) for biosensing is that the signal is amplified intrinsically, resulting in a simplification of the sensor design (compare Fig. 1.2). However, concepts based on inorganic FET technology still struggle with biocompatibility issues. New approaches, using organic substrates, semiconductors and dielectrics have the potential to overcome this problems, and thus are currently a matter of intense research. [25,32,33] A transducer principle resting upon an organic thin film transistor (OTFT) will be discussed in more detail in chapter 6.

1.2.2 Surface Architecture

Direct and Indirect Transduction

One of the main issues of an electrochemical biosensor is to transduce a recognition event into a current. The first generation of biosensors relies on so called electrochemical mediators, whose function is to shuttle the electrons between the reaction site and the surface (see Fig. 1.5 a). In the first devices usually oxygen was used as the mediator, whose concentration however is hard to control. Therefore, in the second generation, the oxygen was replaced by artificial redox mediators, i.e. reversible oxidizing reagents like ferro- or ferricyanide. Techniques based on a mediator are also termed indirect transduction. Third generation biosensors in contrast don't require a mediator and rest upon the direct electron transfer, also called direct transduction (see Fig. 1.5 b). Here, a recognition element is immobilized to the surface and works as a selective catalyst. [34] Hence, the goal of the surface modification of a biosensor is to provide functional groups, which are capable to bind a recognition element. Typical recognition elements are redox enzymes (enzymes which catalyze redox reactions), aptamers or antibodies. For an electrochemical detection the latter uses labeling by a redox enzyme, the corresponding technique is called enzyme-linked immunosorbent assay (ELISA, see Fig. 1.5 c). Here, the analyte specifically binds to immobilized antibodies. In order to detect the concentration of the antibody a second antibody, which is mostly coupled to an enzyme, binds to the analyte. The monitoring of the enzymatic reaction finally allows for a quantitative measurement of the analyte concentration. [35,36] As two specific bindings are necessary to detect the analyte, this technique provides a very high selectivity.

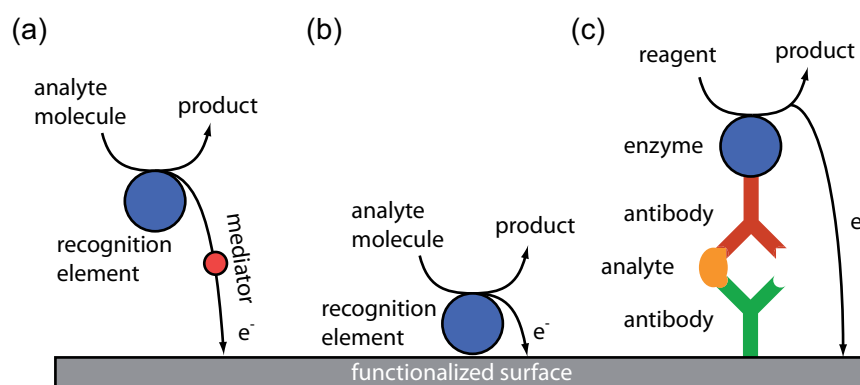


Figure 1.5: Scheme of (a) direct transduction, (b) indirect transduction and (c) of an ELISA-like sandwich.

According to the transduction methods described above the purpose of many biosensors is to detect the electrons which are generated by such a recognition event. This process is often enhanced by conducting materials like gold, graphite or indium tin oxide. More recent approaches also use coatings like self-assembled monolayers, [37] conducting poly-

mers, [38] carbon nanotubes [39] or gold nanoparticles [40].

Supported Lipid Bilayers

As membrane proteins currently present more than half of all drug targets [41], the understanding of their function is of decisive interest for drug screening applications. Consequently artificial lipid membranes are very versatile tools for mimicking biological processes at cell membranes. [42, 43] Regrettably, the progress in using these structures for biosensing is slow. The most common technique involving lipid membranes is impedance spectroscopy, because it allows for modeling the structure of the membrane, including e.g. ion channels. [44, 45] Here, it is important that the lipid membrane shows a good coverage, as defects, gaps or pinholes permit an undesired charge transport.

The advantage of using lipid membranes for the adhesion of living cells, e.g. in order to detect action potentials is, that the fluidity of the lipids allows for the free arrangement of adhesion proteins and receptors, see Fig. 1.6. Here, the inter-membrane distance is about 15 nm [46], which is much smaller than e.g. the width of the extracellular cleft on SiO_2 (about 105 nm [47]). Therefore, a lipid membrane permits a very close approach of the cell to the sensor surface, which results in a higher signal-to-noise ratio. Recently, also the use of field effect transistors coated with lipid membranes was demonstrated as a promising concept for a new class of biosensing devices. [48]

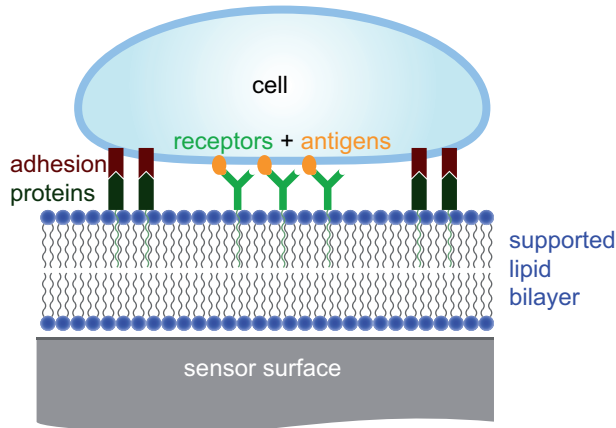


Figure 1.6: Scheme of a cell interfaced with a supported lipid bilayer.

Chapter 2

Organic Field Effect Devices

2.1 Basic Principles of Semiconductor Physics

Although the conducting mechanisms in organic semiconductors are insufficiently described by the theory for classical semiconductors, namely the energy-band model, the latter provides a good starting point for the understanding of organic semiconductor physics. Moreover, in this section especially the surface effects of semiconductors are highlighted, as they play a crucial role for both, the comprehension of semiconductor-electrolyte interfaces and semiconductor devices.

2.1.1 The Energy-Band Model

Electrons in Periodical Potential

The Hamilton operator for electrons in a periodical lattice can be subdivided in the Hamilton operator for free atoms H_a and a Hamilton operator for the perturbation caused by all other atoms H_p :

$$H = H_a + H_p = -\frac{\hbar^2}{2m}\Delta + V_A(\mathbf{r} - \mathbf{R}_m) + H_p(\mathbf{r} - \mathbf{R}_m) \quad (2.1)$$

Where m is the mass of an electron, \hbar is the reduced Planck constant, V_A the Coulomb potential of a free atom, \mathbf{r} the position vector, \mathbf{R}_m the lattice vector of atom m . $H_p(\mathbf{r} - \mathbf{R}_m)$ is given by the relation:

$$H_p(\mathbf{r} - \mathbf{R}_m) = \sum_{n \neq m} V_A(\mathbf{r} - \mathbf{R}_n) \quad (2.2)$$

The energies of the electrons can be calculated by solving the Schrödinger Equation $H\psi_i = E_i\psi_i$. According to the Bloch theorem the wave function of an electron with a wave vector \mathbf{k} is given by:

$$\psi_{\mathbf{k},i} = \sum_m a_m \psi_i(\mathbf{r} - \mathbf{R}_m) = \frac{1}{\sqrt{N}} \sum_m \psi_i(\mathbf{r} - \mathbf{R}_m) \exp(i\mathbf{k}\mathbf{R}_m) \quad (2.3)$$

Where $\psi(\mathbf{r} - \mathbf{R}_m) \exp(i\mathbf{k}\mathbf{R}_m)$ is the eigenfunction of the atoms and N is the number of atoms. This ansatz allows to calculate the energy eigenvalues of the electron:

$$E_{\mathbf{k},i} = \frac{\int \psi_{\mathbf{k},i}^* H \psi_{\mathbf{k},i} dV}{\int \psi_{\mathbf{k},i}^* \psi_{\mathbf{k},i} dV} = E_i - \alpha_i - \sum_{n,m} \beta_{i,n} \exp[i\mathbf{k} \cdot (\mathbf{R}_m - \mathbf{R}_n)] \quad (2.4)$$

Where α_i is the shift of the energy due to the distortion of the other atoms:

$$\alpha_i = - \int \psi_i^*(\mathbf{r} - \mathbf{R}_m) H_p(\mathbf{r} - \mathbf{R}_m) \psi_i(\mathbf{r} - \mathbf{R}_m) dV \quad (2.5)$$

β is the change of energy, due to the overlap of the wave functions:

$$\beta_i = - \int \psi_i^*(\mathbf{r} - \mathbf{R}_n) H_p(\mathbf{r} - \mathbf{R}_m) \psi_i(\mathbf{r} - \mathbf{R}_m) dV \quad (2.6)$$

Hence, in a crystal the discrete energy levels i of free atoms spread into energy bands, which mean energy is shifted by the value $-\alpha_i$ and have a width proportional to β_i . [49] The highest band which is completely filled with electrons at a temperature of $T = 0 \text{ K}$ is called valence band, while the first not fully occupied or unoccupied band is called conduction band. The bands are separated by a region where no electron states are allowed. The origin of this so called energy gap can be understood by recalling that according to the Bloch theorem the wave function Eq. 2.3 is a superposition of plane waves. The resulting standing waves lead either to a maximum or to a minimum charge density at the atomic cores and hence to a reduction or an increase of the electron energy. In this picture the energy gap is given by the difference of these two energies.

Metals and Insulators

According to the energy-band model, metals can be classified as materials with partially occupied conduction band and insulators as materials with a fully occupied valence band and an empty conduction band. The reason for the latter is that the bands can be subdivided in sub-bands with opposite spin directions, resulting in a compensation of the currents of the respective sub-bands. However, this picture describes the nature of an insulator insufficient. Firstly, the lattice constant plays a role for the validity of the energy-band model. As the shielding of the atom cores depends on the electron density, the localization of the core electrons is changing with the lattice constant. According to the uncertainty relation a change in the localization results in a change of energy. Hence, energy bands can only form if the lattice constant is small enough to delocalize the electrons. This so called Mott-transition is the reason why insulators can show metal-like behavior under high pressure. Secondly, the energy band model does not include so called space-charge-limited currents, which can be compared to the current in a vacuum diode and show a crucial dependency on trap states. [50]

Semiconductors

The term semiconductors can be assigned to materials whose energy gap is small enough to be surmounted by thermal excitation, so called intrinsic semiconductors, or to materials with impurity states near the valence or conduction band, so called doped semiconductors. Generally, the charge transport can occur by both, electrons in the conduction band and by unoccupied states, so called holes, in the valence band. Therefore, the conductivity σ is given by the relation:

$$\sigma = e(n\mu_n + p\mu_p) \quad (2.7)$$

Where e is the elementary charge, n the density of electrons, p the density of holes, μ_n the mobility of electrons and μ_p the mobility of holes. According to the Drude model μ_n and μ_p is given by:

$$\mu_n = \frac{v_e^d}{\mathcal{E}} = \frac{e\tau_e}{m_e^*} \quad \text{and} \quad \mu_p = \frac{v_h^d}{\mathcal{E}} = \frac{e\tau_h}{m_h^*} \quad (2.8)$$

Here, v_e^d and v_h^d is the drift velocity of electrons and holes, \mathcal{E} the electric field and τ_e and τ_h are the mean free times between collisions with phonons or defects. m_e^* and m_h^* are the effective masses of electrons and holes and are indirect proportional to the overlap of the wave functions β (see Eq. 2.6). The density of electrons n and the density of holes p , can be calculated by solving the integral of the product of the density of states and the probability of occupation:

$$n = N_C \exp\left(\frac{E_F - E_C}{kT}\right) \quad (2.9)$$

$$p = N_V \exp\left(\frac{E_V - E_F}{kT}\right) \quad (2.10)$$

Where N_C and N_V are the effective densities of states in the conduction and in the valence band, E_C is the lower band edge of the conduction band, E_V is the upper band edge of the valence band, k is the Boltzmann constant and T is the absolute temperature. E_F is the chemical potential (see section 3.1.1), also called the Fermi level. For intrinsic semiconductors E_F lies close to the middle of the band gap and since all electrons on the conduction band origin from the valence band we obtain the relation:

$$n = p = \sqrt{N_C N_V} \exp\left(\frac{-E_g}{2kT}\right) \quad (2.11)$$

Where the energy gap E_g is given by $E_g = E_C - E_V$.

In doped semiconductors impurities give either rise to energy states near the the valence band, so called acceptor levels, which can accept an electron, or energy states near the conduction band, so called donor levels, which can donate an electron. In the first case, the transition of an electron from the valence band to an acceptor level generates a unoccupied state, i.e. a hole in the valence band which can contribute to the hole conductivity (see

Eq. 2.7). In the second case, there is a transition of an electron from a donor level to the conduction band, which can contribute to the electron conductivity. Semiconductors which show hole conductivity are termed p-type semiconductors, while those which show electron conductivity are termed n-type semiconductors. Analogous to Eq. 2.11 charge neutrality results in the relation:

$$n + n_A^- = p + n_D^+ \quad (2.12)$$

Where n_A^- is the density of the charged acceptor levels and n_D^+ is the density of the charged donor levels. The total densities of acceptor and donor levels are given by $n_A = n_A^0 + n_A^-$ and $n_D = n_D^0 + n_D^+$, where n_A^0 and n_D^0 are the densities of neutral dopant states. A detailed discussion of this matter is given in [49].

2.1.2 Semiconductor Interfaces

For the understanding of the thin film transistor (TFT) and double-gate thin film transistor (DGTFT) it is requisite to take a closer look to the relevant interfaces. Firstly, the junction of the contact metal and the semiconductor (MS junction) plays a crucial role for the charge injection. Secondly, the metal-insulator-semiconductor junction (MIS junction) is of significant importance for the comprehension of the charge transport. The treatise of these two junctions is mainly based on the textbook *Physics of Semiconductors* from S. M. Sze [51]. In the end of this section surface states will be discussed, as they are relevant for the deviance from ideal behavior of semiconductor devices as well as for semiconductor-electrolyte interfaces.

The Metal-Semiconductor (MS) Junction

When a metal and a semiconductor are approached to interatomic distances the Fermi energy of the metal E_F^M is aligning with the Fermi level of the semiconductor E_F^{SC} . Note that the Fermi energy of a metal is defined as the highest occupied quantum state of electrons at absolute zero temperature, while the Fermi level of a semiconductor is equal to the chemical potential. Only at absolute zero temperature the Fermi energy equals the Fermi level. The situation for a p-type semiconductor before and after the alignment is illustrated in Fig. 2.1 a and 2.1 b, respectively. For a n-type semiconductor analogous considerations can be made. The thermal equilibrium which is established by charge transfer goes along with the build up of charges at the metal surface and equal but opposite charges at the semiconductor surface. The resulting electric field gives rise to the bending of the valence and conduction band, see Fig. 2.1 b. Due to the high electron density in the metal the charged region of the metal is located very close to the surface, while the charges at the semiconductor are distributed over a region with a certain width w_d , also called depletion width. By inserting the total charge density of a p-type semiconductor $\rho = e(p - n - n_A)$ in the Poisson equation

$$\frac{d^2\psi}{dx^2} = -\frac{\rho(x)}{\epsilon_{SC}} \quad (2.13)$$

where ψ is the potential of the MS junction without an external bias, x the distance to the interface and ϵ_{SC} the permittivity of the semiconductor, one obtains the following relation for the depletion width:

$$w_d = \sqrt{-\frac{2\epsilon_{SC}V_{bi}}{en_A}} \quad (2.14)$$

Where V_{bi} is the so called build-in voltage, the voltage one has to apply to compensate the band bending caused by the contact of the two materials, see Fig. 2.1 b.

Using the condition that the potential must be zero at the interface and regarding the electric field created by the image charges one obtains that there occurs a lowering of the energy barrier $\Delta\phi$ proportional to the square root of the electric field, also called Schottky effect. Therefore, for a p-type semiconductor the total barrier height is given by:

$$e\phi_b = E_g - e(\Phi^M - \chi^{SC}) - e\Delta\phi \quad (2.15)$$

Where, Φ^M is the work function of the metal, χ^{SC} is the electron affinity of the semiconductor, as defined in Fig. 2.1 b. For a high concentration of surface states Fermi level pinning occurs, i.e. the barrier height is independent from the work function of the metal and the Fermi level is pinned by the surface states to a value ϕ_0 . Here the barrier height is given by:

$$e\phi_b = E_g - e\phi_0 - e\Delta\phi \quad (2.16)$$

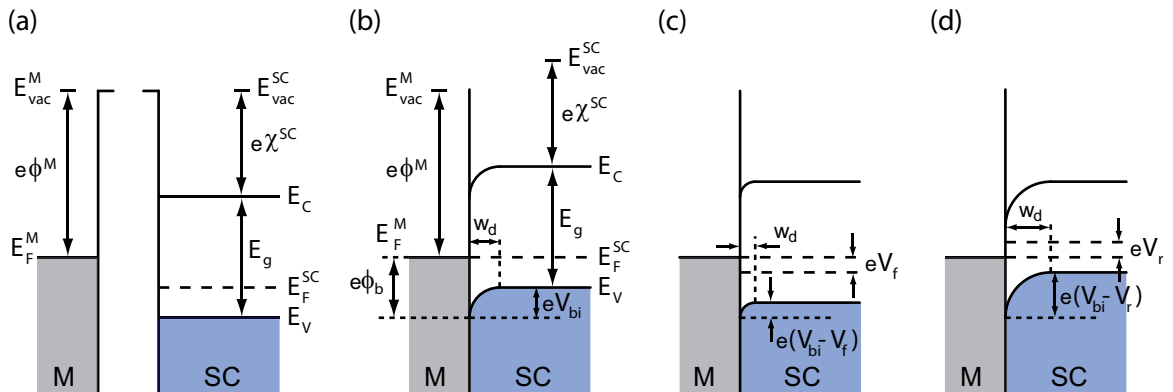


Figure 2.1: Schematic diagram of a MS junction: (a) Metal (M) and semiconductor (SC) are spatially separated, (b) metal and semiconductor are in contact, (c) forward biased MS junction and (d) reverse biased MS junction.

By applying a negative voltage V_f the band bending decreases and charge transfer is enhanced (see Fig. 2.1 c), while by applying a positive voltage V_r the band bending

increases and charge transfer is disabled (see Fig. 2.1 d). The first case is also termed forward bias, the second case reverse bias. The corresponding change in the depletion width can be obtained by substituting V_{bi} in Eq. 2.14 by $V_{bi} - V$.

The Metal-Insulator-Semiconductor (MIS) Junction

In a MIS junction, which can be defined as an insulator sandwiched by a metal and a semiconductor, the field across the insulator results in a band bending which allows for the accumulation of charges. The electron concentration n and the hole concentration p in the semiconductor is given by the change of the potential ψ , which is a measure for the band bending (see Fig. 2.2):

$$n = n_0 \exp \left(\frac{e\psi}{kT} \right) \quad (2.17)$$

$$p = p_0 \exp \left(-\frac{e\psi}{kT} \right) \quad (2.18)$$

Here, ψ is specified with respect to the intrinsic Fermi level E_i , which is defined as the energy in the middle of the band gap.

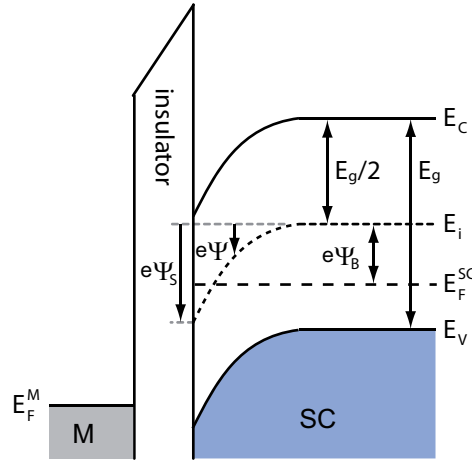


Figure 2.2: Energy band diagram of a MIS junction at the semiconductor surface.

When no voltage is applied between the semiconductor and the metal the difference of the metal work function Φ^M and the work function of a p-type semiconductor (see Fig. 2.3 a) is given by:

$$\Delta\Phi = \Phi^M - \left(\chi^{SC} + \frac{E_g}{2e} - \psi_B \right) \quad (2.19)$$

However in a real device one has to regard the so called flat-band voltage V_{fb} which origins from the phenomena that there is a band curvature at the interface even when no bias is applied, see Fig. 2.3 a.

When a negative voltage is applied at the metal electrode the valence band bend upward and holes are accumulating at the interface, see Fig. 2.3 b. For small positive voltages the valence band bend downwards and holes are depleted at the interface (Fig. 2.3 c). With increasing positive bias however E_i crosses E_F^{SC} and as the concentration of electrons exceeds the concentration of holes an inversion layer is formed (see Fig. 2.3 d).

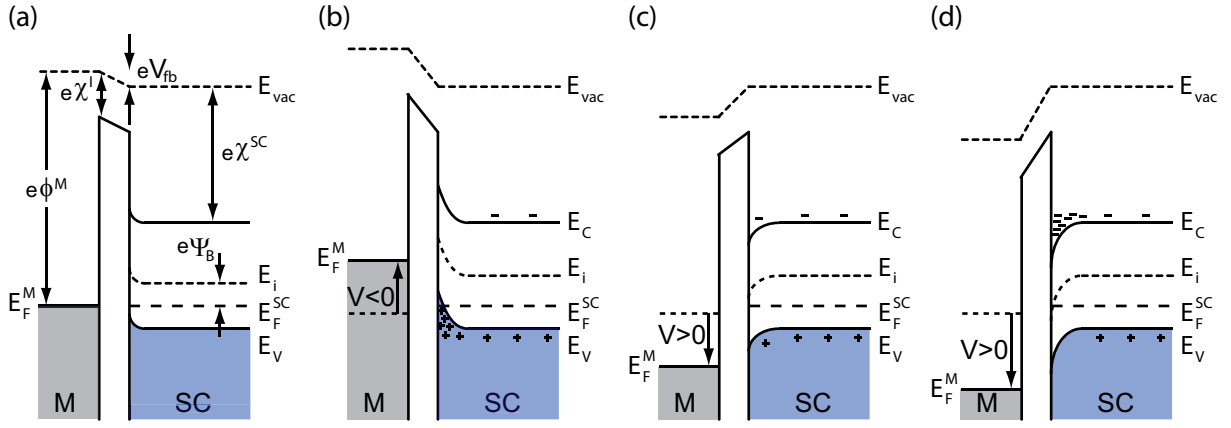


Figure 2.3: Energy band diagrams of a MIS junction for (a) no bias, (b) a negative bias (accumulation), (c) a small positive bias (depletion) and (d) a high positive bias (inversion).

Depending on the surface potential ψ_S for a p-type semiconductor the following regions can be distinguished:

Surface potential	Band bending	region
$\psi_S < 0$	upward	accumulation of holes
$\psi_S = 0$	none	flat band condition
$\psi_B < \psi_S < 0$	downward	depletion of holes
$\psi_S = \psi_B$	downward	midgap: $n_S = p_S = n_i$
$\psi_S > \psi_B$	downward	weak inversion
$\psi_S > 2\psi_B$	downward	strong inversion

The dependency of the surface charge Q_S on the surface potential ψ_S is shown in Fig. 2.4.

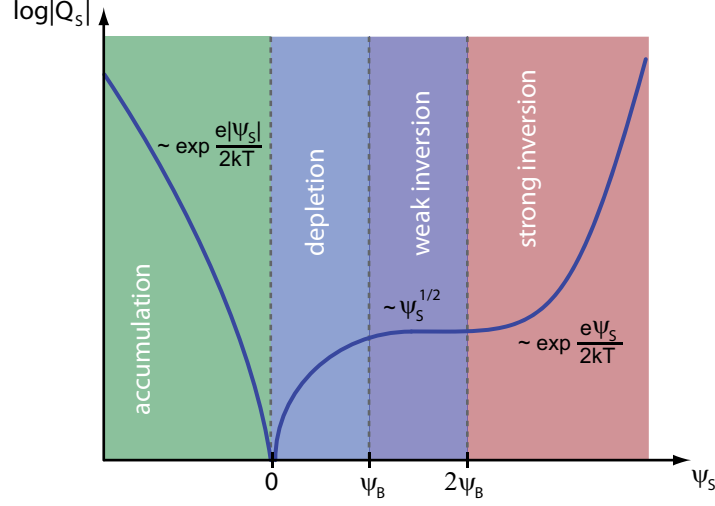


Figure 2.4: Schematic plot of the logarithmic surface charge Q_S of a MIS junction in dependency of the surface potential ψ_S .

Debye Length and Depletion Width

Generally, there are two characteristic length scales which are essential for the understanding of field effect devices.

The so called Debye length is the distance in which the potential of a local excess charge drops by $1/e$ of its value. The decay of the potential with the depth z can be calculated by solving the Poisson equation (Eq. 2.13) for the charge density $\rho = e(n_D - n_A + p - n)$, where n_D and n_A are donor and acceptor concentrations. With the assumption that the concentration of electrons is zero in the bulk of the semiconductor one obtains:

$$\psi(z) = \psi_S \exp\left(-\frac{z}{\lambda_D}\right) \quad (2.20)$$

Where Debye length λ_D is given by:

$$\lambda_D = \sqrt{\frac{\epsilon_{SC} kT}{e^2 p_0}} \quad (2.21)$$

Note that the Debye length not only plays a crucial role in semiconductor physics but also in the description of screening length in electrolytes.

The second important characteristic length is the so called depletion width, which was already mentioned in the characterization of the MS-junction above. The more general form of Eq. 2.14 is

$$w_d = \sqrt{-\frac{2\epsilon_{SC}\psi_S}{en_A}} \quad (2.22)$$

where ψ_S is the surface potential. Taking into account that the maximum depletion width in a MIS-junction is reached when the strong inversion regime sets in, i.e. when $\psi_S = 2 \cdot \psi_B$, one obtains [51]:

$$w_{d,max} = \sqrt{\frac{4 \epsilon_{SC} kT \ln(n_A/n_i)}{e^2 n_A}} \quad (2.23)$$

Surface States

Interfacial effects are important for both, the electronic characterization of thin-film semiconductor devices and the electrochemistry of semiconductor electrodes. Surface States are two-dimensional localized levels in the band gap and can be categorized in two types: surface dangling states and surface ion-induced states. [52]

Surface dangling states, also called Shockley surface states, originates from dangling bonds of surface atoms (see Fig. 2.5 a for a Si-crystal). In order to reduce the surface energy they tend to form bonding or anti-bonding levels with adjacent dangling bonds, corresponding to donor levels near the valence band edge and acceptor levels near the conduction band edge, see Fig. 2.5 b.

Surface ion-induced states, also called Tamm states, results from the difference of the surface lattice potential and the internal lattice potential of an ionic bonding semiconductor. Corresponding to their charge, they can provide cation-induced acceptor levels (SCA) or anion-induced donor levels (SAD), see Fig. 2.5 b.

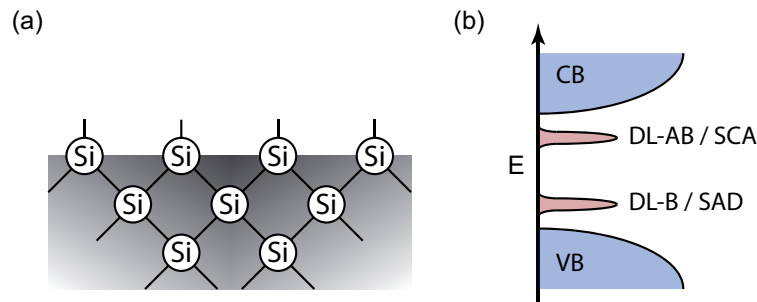


Figure 2.5: (a) Sketch of dangling states of a silicon crystal. (b) Energy diagram with surface dangling donor (DL-B) and surface dangling acceptor (DL-AB) states in a covalently bonded semiconductor or surface anion-induced donor (SAD) and surface cation-induced acceptor (SCA) in an ionic compound semiconductor.

In electrochemistry also adsorption-induced surface states can be relevant. Here the adsorption of covalently bonded particles may induce dangling-like surface states, and the adsorption of ionically bonded particles may induce ion-induced surface states, respectively.

2.2 The Thin Film Transistor

2.2.1 Basic Principle

The thin film transistor (TFT) is a device composed by two metal-contacts (source and drain), which are separated by a thin semiconductor layer, and a third contact (gate) which is separated from the other contacts by an insulating layer. The voltage applied at the gate contact allows to control the conductivity of the semiconductor and hence the current between source and drain. Generally one distinguishes two types of TFTs: the bottom-contact TFT, where the source and drain contacts are located underneath the semiconductor layer (Fig. 2.6 a), and the top-contact TFT where the source and drain contacts are situated on top of the semiconductor layer (Fig. 2.6 b).

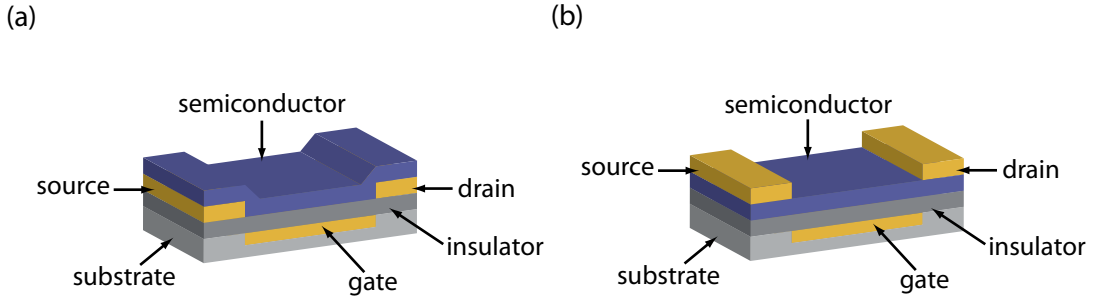


Figure 2.6: Scheme of (a) a bottom-contact TFT and (b) a top-contact TFT.

Obviously in both cases the MS junction and the MIS junction discussed in section 2.1.2 are the key for the understanding of the electrical characteristics. In the following considerations a p-type semiconductor is assumed, as it is the relevant case for this work. Furthermore, the assumptions are made that there are no contact resistances and the flat-band voltage V_{fb} is zero. According to Fig. 2.3 c, a positive voltage V_G applied at the gate contact with respect to the source contact, which is usually grounded, results in an depletion of positive charge carriers at the insulator semiconductor interface. Here, the transistor is in the off-mode and no current between the source and drain contact occurs. In contrast, when a negative voltage V_G is applied at the gate, corresponding to Fig. 2.3 b there is an accumulation of holes. When a negative voltage V_{SD} is applied at the drain contact in respect to the source contact, the accumulated charges are moved by the electric field, a current I_{SD} occurs and the transistor is in the on state. It is important to realize that the surface potential ψ_S is no longer constant in the transistor channel, i.e. in the conductive region between source and drain. As expected, initially I_{SD} increase linearly with V_{SD} (Fig. 2.7 a), however from a certain voltage there is a point in the transistor channel where ψ_S is zero (Fig. 2.7 b). Beyond this so called pinch-off point, the sign of the potential is inverted. With further increasing V_{SD} the pinch-off point moves toward the source contact and as no additional charges are accumulated, the drain current I_{SD} saturates. The plot of the drain current I_{SD} versus the drain potential, the so called conductance or output curve, is shown in Fig. 2.7 c. When, in contrast, the gate voltage V_G is swept at

a constant drain voltage V_{SD} , the pinch-off point moves towards the drain contact with increasing V_G and therefore there is a transition from the saturation to the linear regime. The plot of the drain current I_{SD} versus the gate voltage V_G , also called transconductance or transfer curve, is shown in Fig. 2.7 d. Note that analogous considerations can be made for n-type semiconductors.

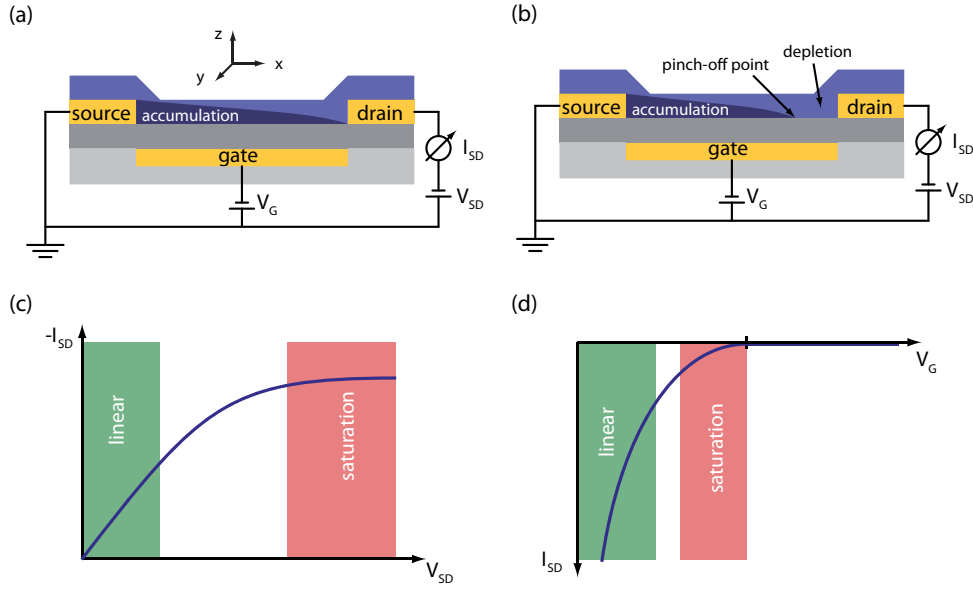


Figure 2.7: (a) Scheme of the potential distribution of a TFT in (a) the linear regime and (b) in the saturation regime. Sketches of the corresponding output and transfer curves are shown in (c) and (d).

By applying a high positive voltage according to Fig. 2.3 d inversion, e.g. the accumulation of electrons, occurs. However, TFTs are usually operated in accumulation mode and not in inversion, because it is difficult to find contact materials with a suitable work function for the injection of negative charges. Moreover, most organic semiconductors show a bad conductivity for minority charge carriers due to high concentrations of traps.

2.2.2 Current-Voltage Characteristics

In this section the qualitatively predictions of the electric characteristics of a TFT made above will be verified quantitatively. Here, most of the theoretical background is adopted from the works of G. Horowitz [53], C. D. Dimitrakopoulos [54] and Brown et al. [55].

The Linear Regime

In the linear region the gate voltage drop can be subdivided in three contributions:

$$V_G = V_I + V_{fb} + \psi_S(x) \quad (2.24)$$

where V_I is the potential drop across the insulator, V_{fb} is the flat band voltage and $\psi_S(x)$ is the surface potential at the distance x from the source contact. The continuity of the electric field, implies $\epsilon_{SC}\mathcal{E}_{SC} = \epsilon_I\mathcal{E}_I$, where ϵ_{SC} and ϵ_I is the permittivity of the semiconductor and the insulator and \mathcal{E}_{SC} and \mathcal{E}_I the electric field in the semiconductor and insulator. Regarding that the voltage drop at the insulator is given by $\mathcal{E}_I d_I$ one obtains:

$$V_G = \frac{\epsilon_{SC}\mathcal{E}_{SC}}{C_I} + V_{fb} + \psi_S(x) \quad (2.25)$$

Here, $C_I = \epsilon_I/d_I$ is the capacitance per unit area of the insulator, where d_I is the thickness of the insulator. Under the assumption that $\psi_S > kT$ the electric field can be estimated as [56]:

$$\mathcal{E}_{SC} \approx \sqrt{\frac{2kTn_0}{\epsilon_{SC}}} \exp\left(\frac{e\psi_S}{2kT}\right) \quad (2.26)$$

Hence, $\psi_S(x)$ in Eq. 2.25 can be neglected and with the gradual channel approximation $|\partial\mathcal{E}_x/\partial x| \ll |\partial\mathcal{E}_y/\partial y|$, the space charge per unit area is given by:

$$Q(x) = -C_I [V_G - V_{fb} - V(x)] \quad (2.27)$$

Assuming that the charge carrier density in the bulk is given by $Q_0 = e p_0 d_{SC}$, where d_{SC} is the thickness of the semiconductor layer, and using Eq. 2.7 for the conductance, the differential form of Ohm's law gives:

$$dV = I_{SD} dR = \frac{I_{SD} dx}{W\mu (|Q(x) + Q_0|)} \quad (2.28)$$

Where R is the resistance and W the width of the conducting channel. By integrating Eq. 2.28 over the channel length L , i.e. from $(x = 0, V = 0)$ to $(x = L, V = V_{SD})$ one obtains finally the expression for the drain current:

$$I_{SD} = \frac{W}{L} \mu C_I \left[(V_G - V_T) V_{SD} - \frac{V_{SD}^2}{2} \right] \quad (2.29)$$

with the so called threshold voltage V_T :

$$V_T = \frac{e p_0 d_{SC}}{C_I} + V_{fb} \quad (2.30)$$

For small drain voltages, e.g. $|V_{SD}| \ll |V_G - V_T|$ Eq. 2.29 simplifies to:

$$I_{SD}^{lin} = \frac{W}{L} \mu C_I (V_G - V_T) V_{SD} \quad (2.31)$$

The result that the drain current is direct proportional to the drain voltage is consistent with the qualitatively prediction made in the previous section.

The Saturation Regime

Regarding the influence of the bulk conductivity and the flat band voltage by introducing the threshold voltage V_T (see Eq. 2.30) the pinch-off point is given by the location in the channel where $V(x) = V_G - V_T$. As already mentioned no holes are accumulated beyond this point, what can be interpreted as reduction of the effective channel length. The drain current in the saturation regime is given by the sum of two integrals [55]:

$$I_{SD}^{sat} = \frac{W}{L} \mu C_I \int_0^{V_G} (V_G - V_T - V) dV + \frac{W}{L} \mu e p_0 \int_{V_G}^{V_{SD}^{sat}} (d_{SC} - w_d) dV \quad (2.32)$$

Here, the first term corresponds to the accumulation region and the second term to the depletion region. The depletion width $w_d(x)$ is given by:

$$w_d(x) = \frac{\epsilon_{SC}}{C_I} \left(\sqrt{1 + \frac{2C_I^2 (V_G - V_{fb} - V(x))}{e n_A \epsilon_{SC}}} - 1 \right) \quad (2.33)$$

Assuming that $C_{SC} \gg C_I$ and identifying the dopant concentration with the carrier concentration, one obtains a simple expression of the drain current in the saturation regime:

$$I_D^{sat} = \frac{W}{2L} \mu C_I (V_G - V_T)^2 \quad (2.34)$$

As expected in this regime the drain current does not depend on the drain voltage.

2.2.3 Characteristic Parameters

The Mobility

As already discussed in section 2.1.1 the mobility is defined as the proportionality factor of the drift velocity v_{SD} and the electric field \mathcal{E} : $v_D = \mu \cdot \mathcal{E}$. The high relevance of the mobility for the TFT characterization is arising from its independence from geometrical factors.

By differentiating the drain current in Eq. 2.31 with respect to the gate voltage, one obtains the following expression for the mobility in the linear regime:

$$\mu_{lin} = \frac{L}{W C_I} \frac{1}{V_{SD}} m_{lin} \quad (2.35)$$

where $m_{lin} = \Delta I_D / \Delta V_G$ is the slope of the transconduction curve in the linear regime, see Fig. 2.8 a.

The mobility can also be calculated by differentiating the square root of the drain current in the saturation regime I_{SD}^{sat} (Eq. 2.34) with respect to V_G :

$$\mu_{sat} = \frac{2L}{W C_I} m_{sat}^2 \quad (2.36)$$

where $m_{sat} = \Delta \sqrt{I_{SD}^{sat}} / \Delta V_G$ is the slope of $\sqrt{I_{SD}^{sat}}$ plotted versus V_G , see Fig. 2.8 b.

The Threshold Voltage

The threshold voltage V_T has its origin in the flat-band voltage V_{fb} and the bulk conductance (see Eq. 2.30). Descriptively explained, V_T is a measure for the point when the transistor switches between the off-state and the on-state. From Eq. 2.34 it is apparent that V_T can be obtained by the V_G -intercept of $\sqrt{I_{SD}^{sat}}$ plotted versus V_G , see Fig. 2.8 b.

The Subthreshold Swing

The speed of the switching process is given by the so called subthreshold swing S , which is defined as the gate voltage which must be applied to increase the drain current by one order of magnitude, see Fig. 2.8 c. In this context often the ratio of the current in the on-state I_{on} and the current in the off-state I_{off} , as defined in Fig. 2.8 c, is quoted. Please note that there is a regime situated intermediately between the off-state and the saturation regime in the transfer curve. This regime is sometimes called subthreshold region and is specified by an exponential increase of the drain current [57]. It has been shown that the subthreshold region is very sensitive to the presence of traps [58]. Especially for low drain voltages, as used for sensor devices based on TFTs, this regime plays a crucial role.

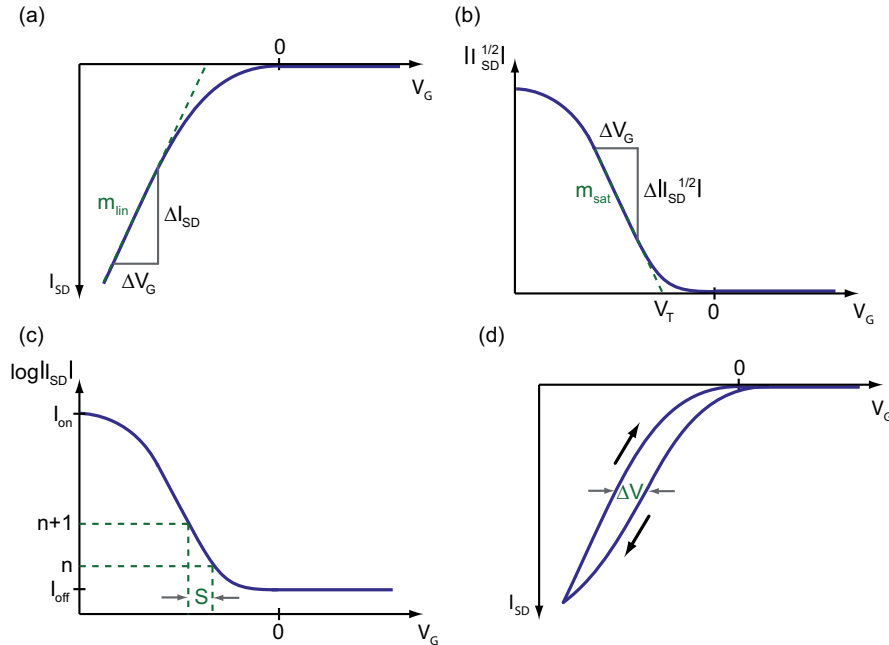


Figure 2.8: Characteristic parameters of a TFT: Visualization of (a) the mobility in the linear regime, (b) the mobility in the saturation regime and the threshold voltage, (c) the subthreshold swing and (d) the hysteresis.

The Hysteresis

In the transfer curves of real devices the curve obtained by sweeping from the off-state to the on-state is not congruent with the curve of the reverse sweep direction. This phenomena is called hysteresis and is defined as the shift of the threshold voltage of the forward and the backward sweep. The origin of the hysteresis are the filling and emptying of trap states situated in the band gap of the semiconductor. The additional charge of the immobile charge carriers changes the effective gate voltage and shifts the transfer curve by a voltage ΔV , see Fig. 2.8 d.

2.3 The Double-Gate Thin Film Transistor

For many applications it is desirable to operate a TFT in a small voltage window. One possibility to adjust a working point is to control the threshold voltage by the field of a second gate contact, which is separated to the semiconductor by a second insulator (see Fig. 2.9). Such a device is called double-gate TFT (DGTFT) or dual-gate TFT and is a well established concept for inorganic devices operating in the inversion regime [59]. Though several works on DGTFTs working in accumulation mode have been published in the last few years [60,61], to our knowledge no analytical model is available on this matter. In this section the concept of Lim et al. [59] for double-gate metal-oxide-semiconductor field-effect transistors (MOSFETs) working in the inversion regime is modified for DGTFTs working in the accumulation regime.

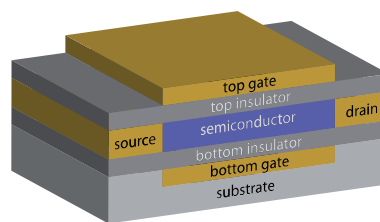


Figure 2.9: Schematic of a DGTFT

2.3.1 Basic Principle

Before the problem is treated quantitatively, first the operation of a DGTFT is explained qualitatively. The basic idea is that it is possible to establish an accumulation channel at the bottom-insulator/semiconductor interface and at the top-insulator/semiconductor interface, respectively. When the bottom-interface is accumulated, screening occurs and the surface potential at the top-interface is not affected. In contrast, if the bottom-channel is depleted it is possible that the field resulting from the potential at the bottom-gate contact exceeds to the top-interface and thus changes the corresponding surface potential, see Fig. 2.10. This, in turn results in a shift of the threshold voltage.

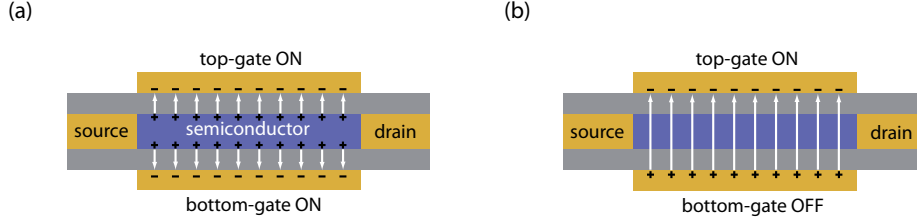


Figure 2.10: Illustration of the basic principle of a DGTFET. (a) Both interfaces are accumulated and hence screened by each other. (b) The bottom-gate is in the off-state and therefore the electric field can extend to the top-interface and may switch it to the off-state.

Note that the top-interface and the bottom-interface may have different threshold voltages. Therefore it is not only possible to shift the threshold voltage of the top interface toward negative values, i.e. switch to the off-state, but also to shift the threshold voltage towards positive voltages, i.e. the transistor opens up more early. This situation occurs when the voltage at the bottom gate is biased negatively, but the bottom interface is not yet accumulated. To simplify the analysis let's assume that the threshold voltage of the bottom-gate V_T^b equals zero when the top-gate is floating and the threshold voltage of the top-gate V_T^t equals zero when the bottom-gate is floating. The DGTFET can be operated in four different modes: double accumulation (bottom-gate voltage V_G^b and top-gate voltage V_G^t negative), double depletion (V_G^b and V_G^t positive), shift of V_T^t by V_G^b (V_G^b positive and V_G^t negative) and shift of V_T^b by V_G^t (V_G^b negative and V_G^t positive), see Fig. 2.11 a. The corresponding charge distributions are schematically plotted in Fig. 2.11 b.

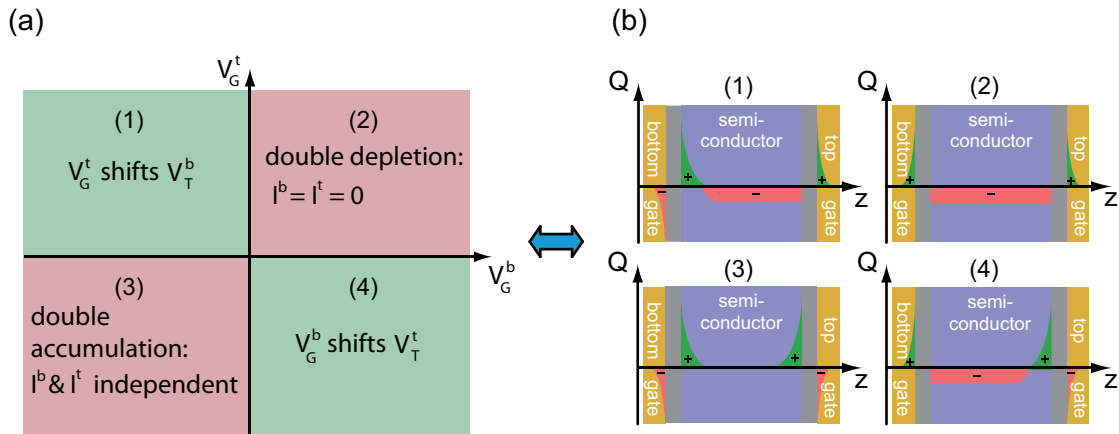


Figure 2.11: Schematic of (a) the operation modes of an idealized DGTFET. The regions where one gate influences the threshold voltage of the opposed interface are highlighted green, while the independent regions are highlighted red. (b) illustrates the charge distribution across the DGTFET layers. The accumulation of charges is marked green and the depletion is marked red.

To figure out the qualitatively current characteristic for a bottom-gate sweep, it is reasonable to distinguish the following two situations [60]:

1. The top-gate is biased negatively at voltage V_G^t and the top-interface is in the accumulation regime. When the bottom-interface is in the depletion regime and the bottom-gate voltage V_G^b is swept towards positive voltages, there is a voltage at which the top channel is depleted by the electric field created by the bottom gate, see Fig. 2.12 a. Therefore the threshold voltage of the top-gate V_T^t has been adjusted to V_G^b .
2. The top-gate is biased positively at voltage V_G^t and the top-interface is in the depletion regime. The threshold of the bottom-interface V_T^b is shifted towards more negative values, see Fig. 2.12 b.

Hence, the threshold-voltage of a DGTFT depends on whether V_G^b or V_G^t is more positive. In the following section the resulting threshold voltages will be discussed quantitatively.

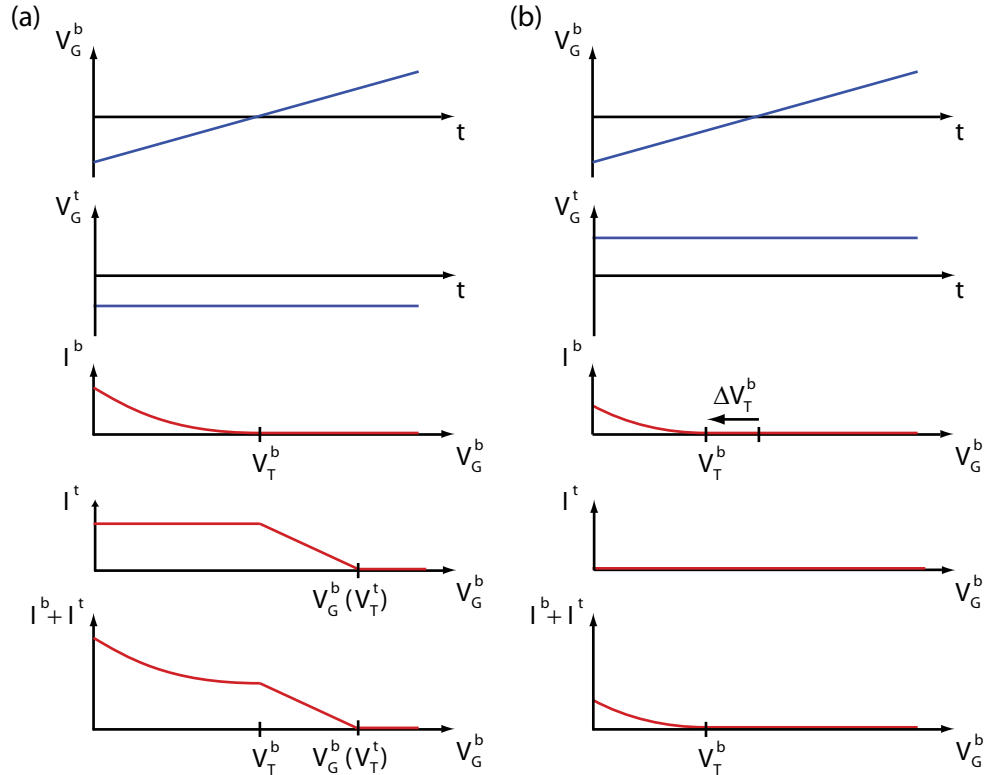


Figure 2.12: Sketch of the current-voltage characteristic of a DGTFT. Sweep of the bottom-gate voltage with (a) a negative biased top-gate and (b) a positive biased top-gate. Additional to the schematic curves of the voltages, the bottom-interface current, the top-interface current and the total current is plotted qualitatively.

2.3.2 Current-Voltage Characteristics

The quantitative analysis of the current-voltage characteristics of DGTFTs is based on the same principle than for the TFT (section 2.2.2). The starting point is solving the Poisson equation (Eq. 2.13) for the potential for the bottom-gate surface potential ψ_s^b , the top-gate surface potential ψ_s^t and the charge density $-en_A$. Analogous to Eq. 2.24 the surface potentials are given by the following relations:

$$V_G^b = V_I^b + V_{fb}^b + \psi_s^b \quad (2.37)$$

$$V_G^t = V_I^t + V_{fb}^t + \psi_s^t \quad (2.38)$$

where V_G^b and V_G^t is the voltage applied at the bottom-gate and the top-gate, V_I^b and V_I^t are the potential drops of the top- and bottom gate insulators and V_{fb}^b and V_{fb}^t are the corresponding flat band voltages. Assuming that the semiconductor is completely depleted, except from a narrow accumulation layer with a negligible thickness, one obtains by integration that the surface potential difference is approximately given by [59]:

$$\psi_{SC} = \psi_s^t - \psi_s^b \approx \left(\mathcal{E}_{SC}^t - \frac{en_A d_{SC}}{2\epsilon_{SC}} \right) d_{SC} \quad (2.39)$$

Here, \mathcal{E}_{SC}^t is the electric field at the top-gate/semiconductor interface, d_{SC} the thickness of the semiconductor layer, n_A the doping density and ϵ_{SC} the permittivity of the semiconductor. Using Gauss's theorem the potential drop of the bottom-gate insulator V_I^b and the potential drop of the top-gate insulator V_I^t are given by

$$V_I^b = -\frac{1}{C_I^b}(\epsilon_{SC}\mathcal{E}_{SC}^t - en_A d_{SC} + Q_a^b) \quad (2.40)$$

and

$$V_I^t = \frac{1}{C_I^t}(\epsilon_{SC}\mathcal{E}_{SC}^t - Q_a^t) \quad (2.41)$$

Here, C_I^b and C_I^t are the capacitances per unit area of the bottom- and top-gate insulator and Q_a^b and Q_a^t are the accumulation charges at the bottom- and top-interface. By solving Eq. 2.39 for \mathcal{E}_{SC}^t and inserting in Eq. 2.40 and Eq. 2.41, Eq. 2.37 and Eq. 2.38 become:

$$V_G^b = V_{fb}^b - \frac{C_{SC}}{C_I^b}\psi_s^t + \left(1 + \frac{C_{SC}}{C_I^b}\right)\psi_s^b - \frac{Q_{SC}/2 + Q_a^b}{C_I^b} \quad (2.42)$$

$$V_G^t = V_{fb}^t + \left(1 + \frac{C_{SC}}{C_I^t}\right)\psi_s^t - \frac{C_{SC}}{C_I^t}\psi_s^b - \frac{Q_{SC}/2 + Q_a^t}{C_I^t} \quad (2.43)$$

where $C_{SC} = \epsilon_{SC}/d_{SC}$ is the capacitance per unit area of the semiconductor and $Q_{SC} = -en_A d_{SC}$ the depletion region areal charge density. Eq. 2.42 and Eq. 2.43 allows for the determination of the top-gate threshold voltage V_T^b in terms of V_G^b and the determination

of the bottom-gate threshold voltage V_T^b in terms of V_G^t . As the description of the latter is analogous to that of the former, in the following only the influence of the bottom-gate on V_T^t will be discussed.

Accumulated Bottom Surface

When the bottom-interface starts to accumulate ψ_S^b is zero. Beyond this point the bottom-gate voltage has no influence on the top-interface and one say that ψ_S^b is virtually pinned at zero. Hence Eq. 2.43 yields:

$$V_{T,ac}^t = V_{fb}^t + \left(1 + \frac{C_{SC}}{C_I^t}\right) \psi_S^t - \frac{Q_{SC}/2 + Q_a^t}{C_I^t} \quad (2.44)$$

As in the usual TFT theory the threshold is not defined by a certain surface potential but by Eq. 2.30 it is reasonable to define the threshold voltage of the top-interface as the onset of accumulation, i.e. $\psi_S^t = 0$ and $Q_a^t = 0$. With Eq. 2.44 one obtains:

$$V_{T,ac}^t = V_{fb}^t - \frac{Q_{SC}}{2C_I^t} \quad (2.45)$$

Note that that this result differs from the threshold of a single gate TFT by the term $Q_{SC}/(2C_I^t)$.

Depleted Bottom Surface

The onset voltage, i.e. the onset of accumulation of the bottom-interface corresponds to $\psi_S^b = 0$ and $Q_a^b = 0$ and is hence given by:

$$V_{on}^b = V_{fb}^b - \frac{C_{SC}}{C_I^b} \psi_S^t - \frac{Q_{SC}}{2C_I^b} \quad (2.46)$$

To simplify the problem lets assume again that at the threshold voltage there are no accumulated charges, i.e. $Q_a^t = 0$. By solving Eq. 2.42 for ψ_S^b , inserting in Eq. 2.43 and using Eq. 2.44 and Eq. 2.46 one obtains for the threshold voltage of the top-gate:

$$V_{T,dep}^t = V_{T,ac}^t - \frac{C_{SC}C_I^b}{C_I^t(C_{SC} + C_I^b)} (V_G^b - V_{on}^b) \quad (2.47)$$

Hence, the threshold voltage of the top-gate for a depleted bottom-interface differs from the threshold voltage for an accumulated bottom-interface by a factor which is proportional to the difference of V_G^b and the onset-voltage V_{on}^b . The threshold shifts until the accumulation or the strong inversion regime is reached, i.e. the field of the bottom gate is screened.

Inverted Bottom Surface

Strong inversion is defined by $\psi_S^b = 2\psi_B$. By inserting this condition in Eq. 2.43 and make the analogous assumptions than for Eq. 2.45 one obtains for the threshold voltage of the inversion regime:

$$V_{T,inv}^t = V_{fb}^t + 2\psi_B - \frac{Q_{SC}}{C_I^t} \quad (2.48)$$

By assuming $Q_a^b \ll Q_{SC}$ and inserting $\psi_S^b = 2\psi_B$ in Eq. 2.42 one obtains the onset voltage of the inversion regime V_{inv}^b :

$$V_{inv}^b = V_{fb}^b - \frac{C_{SC}}{C_I^b} \psi_S^t + \left(1 + \frac{C_{SC}}{C_I^b}\right) 2\psi_B - \frac{Q_{SC}}{2C_I^b} \quad (2.49)$$

The resulting shift of the threshold voltage is shown in Fig. 2.13.

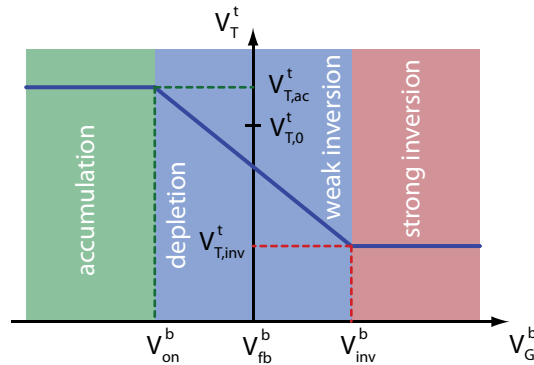


Figure 2.13: Illustration of the threshold voltage shift of the top-gate V_T^t dependent on the bottom-gate voltage V_G^b . The green area symbolize the accumulation regime, the blue area the depletion and weak inversion regime and the red area the strong inversion regime. The threshold voltage of the top-interface when there is no influence from the bottom-gate is indicated as $V_{T,0}^t$.

Influence of the depletion width

In the last section the assumption was made that the semiconductor film is completely depleted. The thin accumulation layer can be neglected as the Debye length λ_D (see Eq. 2.21) is much smaller than the depletion width w_d . Therefore, the expressions for the threshold voltage for an accumulated and for a depleted bottom interface given in Eq. 2.45 and Eq. 2.47 are only valid if the semiconductor film thickness d_{SC} is less or equal than the depletion width w_d . Here, the theory for TFTs operating in the accumulation regime fundamentally differs from the theory for MOSFETs operating in the inversion regime, which was discussed by Lim et al. [59]. The reason is that in the first case the onset voltage corresponds to a depletion width of zero, while in the second case the onset of

inversion corresponds the maximum depletion width. According to Eq. 2.33 the depletion width of the bottom-interface is given by:

$$w_d^b = \frac{\epsilon_{SC}}{C_I^b} \left(\sqrt{1 + \frac{2C_I^{b^2}(V_G^b - V_{fb}^b - \psi_S^b)}{en_A\epsilon_{SC}}} - 1 \right) \quad (2.50)$$

The maximum depletion width $w_{d,max}^b$ is reached when strong inversion sets in, e.g. $\psi_S^b = 2\psi_B$. The depletion width of the bottom-interface w_d^t is given by the corresponding formula. The dependency of the maximum depletion width $w_{d,max}$ on the dopant concentration in the bulk n_A is shown in Fig. 2.14. For comparison additionally the Debye length λ_D (see Eq. 2.21) is plotted. Here the approximation is used that the charge carrier concentration p_0 equals the doping concentration n_A .

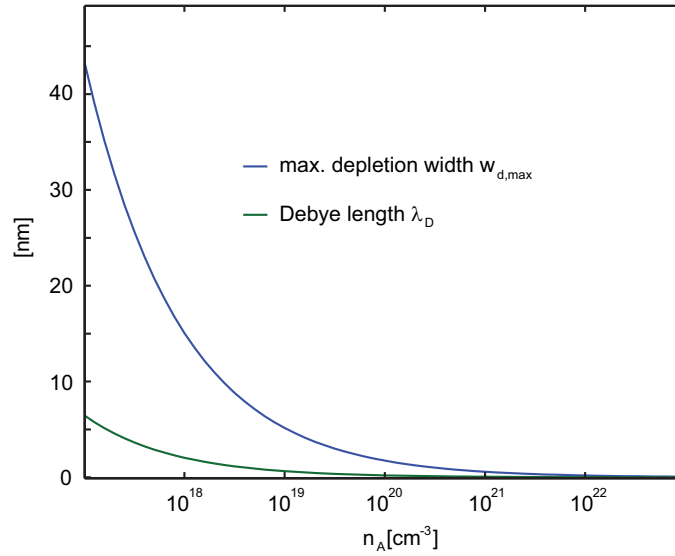


Figure 2.14: Simulation of the dependency of the depletion width and Debye length on the charge carrier concentration. For the calculation the permittivity of pentacene ($\epsilon_{SC} = 3.0 \epsilon_0$) was chosen.

In contrast to the MOSFET theory, the depletion caused by the top-gate is not relevant, because the depletion width is zero at the threshold voltage. This means that even when the sum of the depletion width of the bottom-interface and that of the top-interface exceeds the film thickness, there is no effect on the top-gate threshold voltage. Therefore, it is possible to distinguish two regimes:

- $d_{SC} \geq w_{d,max}^b$: The film is never completely depleted by the bottom gate and the threshold voltage is given by the formula for the single gate TFT Eq. 2.30:

$$V_{T,0}^t = V_{fb}^t - \frac{Q_{SC}}{C_I^t} \quad (2.51)$$

- $d_{SC} \leq w_d^b$: The film is depleted by the bottom gate and the threshold voltage is given by Eq. 2.47.

Note that for $V_{T,ac}^t$ the depletion width at the bottom interface is zero, and hence the situation shown in Fig. 2.13 never occurs in real devices. As w_d^t does not contribute to the threshold shift, the maximum shift is reached when $V_G^b = V_{inv}^b$. The influence of the depletion width on the threshold voltage shift is qualitatively shown in Fig. 2.15.

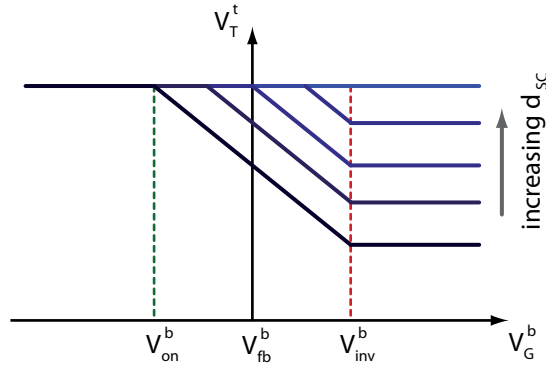


Figure 2.15: Illustration of the influence of the depletion width on the threshold voltage shift of a DGTFT.

In real devices the shift is not only limited by the depletion width caused by the gate voltage but also by the influence of the field originating from the source and drain contact. Additionally, when the bottom-interface is in the saturation regime (see Fig. 2.7), the depletion zone beyond the pinch-off point may exceed to the top-interface and consequently affect the threshold voltage.

The threshold voltage of a DGTFT

With the findings above it is now possible to predict the the total threshold voltage of a DGTFT. As discussed in section 2.3.1 the onset of the current for a bottom gate sweep can origin from two different mechanisms. For positive top-gate voltages, the onset is given by the bottom-interface threshold V_T^b , which is controlled by the top-gate voltage. Analogous to Eq. 2.47 the threshold voltage in this regime is given by:

$$V_T = V_T^b = V_{T,ac}^b - \frac{C_{SC}C_I^t}{C_I^b(C_{SC} + C_I^t)}(V_G^t - V_{on}^t) \quad (2.52)$$

where $V_{T,ac}^b = V_{fb}^b - Q_{SC}/(2C_I^b)$ and $V_{on}^t = V_{fb}^t - (C_{SC}/C_I^t)\psi_S^b - Q_{SC}/(2C_I^t)$.

For negative top-gate voltages, the onset is given by the bottom-gate voltage, which is needed to deplete the top-interface $V_G^b(V_T^t)$. This voltage can be derived from Eq. 2.47:

$$V_T = V_G^b(V_T^t) = V_{on}^b - \frac{C_I^t(C_{SC} + C_I^b)}{C_{SC}C_I^b}(V_G^t - V_{T,ac}^t) \quad (2.53)$$

To get a more descriptive idea of the situation let's assume the on-voltages V_{on}^b and V_{on}^t are zero and the threshold voltages of the top-interface and the bottom-interface do not reach $V_{T,ac}$ or $V_{T,inv}$. Now, when the threshold voltage for a bottom-gate sweep V_T is plotted versus the applied top-gate voltage V_G^t a regime with the slope $C_{SC}C_I^t/[C_I^b(C_{SC} + C_I^t)]$ for positive V_G^t and a regime with the slope $C_I^t(C_{SC} + C_I^b)/(C_{SC}C_I^b)$ for negative V_G^t can be observed (see Fig. 2.16).

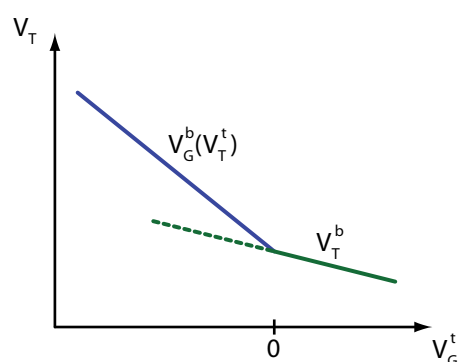


Figure 2.16: The two threshold voltage regimes of a DGTFT. The figure shows an idealized plot of the threshold voltage of bottom-gate sweeps versus the top-gate voltage.

Note, that when the top gate is floating the threshold lies somewhere on the curve for positive V_G^t or its interpolation (see dashed line in Fig. 2.16). Consequently, it may occur that when the transition point of the two regimes is positive, the threshold voltage may be more negative for a floating top-gate than for a positively biased top-gate.

2.4 Organic Semiconductors

In this section the structural and electronic properties of organic semiconductors will be discussed. The content of this chapter is mainly based on the textbook of Schwörer and Wolf [62].

2.4.1 Structural Properties

Organic materials are termed as small molecule crystals or polymers consisting mainly of a carbon atom structure with a conjugated π -electron system. The electron configuration of a single excited carbon atom is $1s^2 2s^1 2p_x^1 2p_y^1 2p_z^1$. A double bond between two carbon atoms is based on a so called sp^2 -hybridization, i.e. one $2s$ -orbital and the p_x - and p_y -orbitals form three σ -bonds, which are coplanar and arranged in a 120° angle, respectively, while the third p_z orbital is unchanged. The overlap of these remaining p_z -orbitals results in the so called π -bond. The corresponding π -electrons are much weaker bonded than the σ -electrons and therefore delocalized over the whole molecule. As π -electrons fill the highest occupied

molecular orbital (HOMO), they mainly determine the electronic and optical properties of organic molecules. One of the main advantages of organic molecules is that the energy band gap, i.e. the energetic separation of the lowest unoccupied molecular orbital (LUMO) and the HOMO, can be tuned over a wide range by modifying the molecular structure. Due to their easy handling, stability and solubility amorphous polymer layers are preferred for applications like organic light-emitting diodes (OLEDs) or organic photovoltaic cells (OPVCs). For high performance devices like OTFTs however highly ordered crystals of small molecules are preferred, as these show the highest mobilities. The most common classes of small molecules used for semiconductor devices are polyacenes, consisting of linearly fused benzene rings, polycyclic aromatic hydrocarbons or fullerenes (see Fig. 2.17).

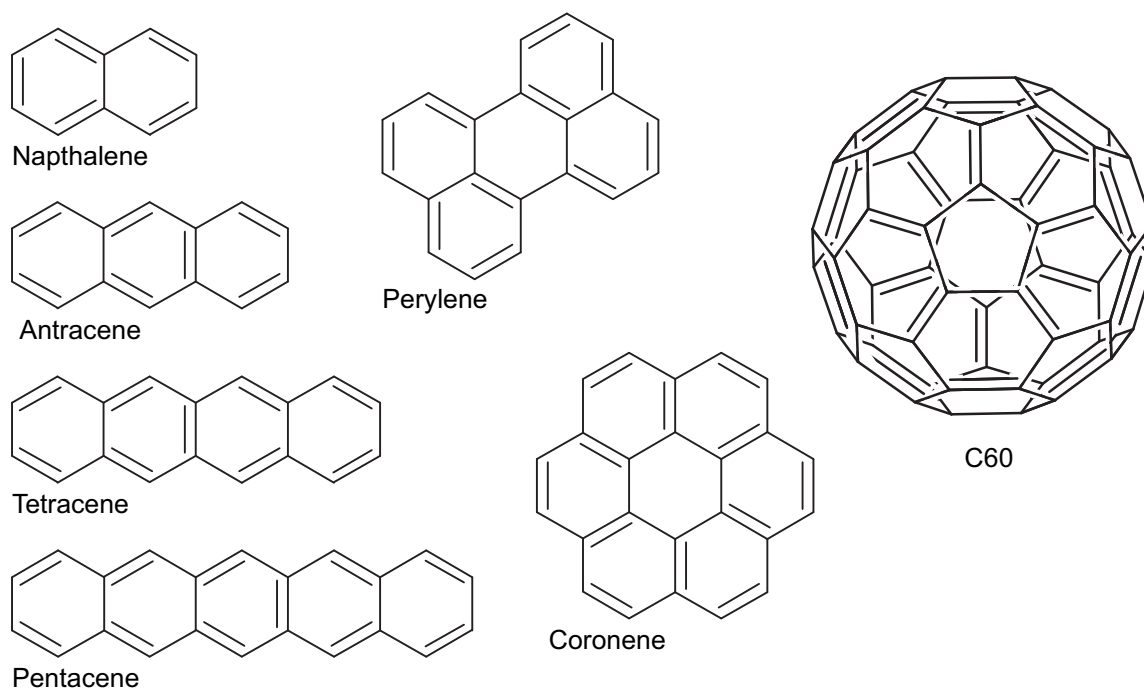


Figure 2.17: Structural formulas of common organic semiconductors: Polyacenes (naphthalene, anthracene, tetracene, pentacene), polycyclic aromatic hydrocarbons (perylene, coronene) and the fullerene C60. The images of the structures were created by the software ACD/ChemSketch 12.01.

The crystal structures of these molecules are based on van der Waals binding and therefore dominated by the principle of close packing. By determining the ratio of the total stack area and total glide area, it is possible to classify four different crystal structures: herringbone, sandwich, γ and β . [63]

2.4.2 Electronic Properties

When a charge carrier is located at a certain molecule in an organic molecular crystal it creates a polarization of its own environment, which follows the movement of the carrier

instantaneously. The corresponding quasiparticles are called polarons. The energy of a hole polaron P_h , which moves in the valence band, is given by the difference of the ionization energy of the molecule in the gas phase and the ionization energy of the molecule in the crystal. The energy of an electron polaron P_e , which moves in the conduction band, is given by the difference of the electron affinity of the molecule in the gas phase and the electron affinity of the molecule in the crystal. Therefore, the energy gap between the valence band and the conduction band of the crystal, also called optical band gap, differs from the energy gap between the HOMO and LUMO level of a molecule by the value $P_h + P_e$. Additionally to the electronic polarization, there is also a vibronic polarization, i.e. the polaron causes a lattice relaxation which lowers the energy gap. This lowered energy gap is called adiabatic band gap.

In a real crystal local compressions and dilatations result in a Gaussian distribution of the polaron states. While the polarons in the center of the distribution form the valence and conduction bands, the polarons in the band gap form trap states, i.e. they can be filled with charge carriers, but do not further contribute to the charge transport. Trap states near the conduction or valence band are also called shallow traps and can be thermally emptied. Electrons or holes which are trapped in states which are more distant to the conduction or valence band, so called deep traps, can not be released thermally. Analogous, imperfections in the crystal structure like defects, impurities or grain boundaries result in trap states.

The Theory of Sommerfeld

Neglecting the trap states mentioned above the band transport of charge carriers can be described by quasi-free electrons, whose behavior is determined by the Schrödinger equation and the Pauli exclusion principle. In the semi-classical approach of Sommerfeld the change of the quasi-momentum $\hbar\mathbf{k}$ of an electron in an electric field \mathcal{E} is given by:

$$\hbar\dot{\mathbf{k}} = -e\mathcal{E} \quad (2.54)$$

This corresponds to a small shift $\delta\mathbf{k} = -e\mathcal{E}\delta t/\hbar$, where δt is the time the system needs to obtain a dynamical equilibrium after the electric field was applied. In the simplest case this can be interpreted as a shift of the Fermi sphere. Note that only the fast electrons at the Fermi surface contribute to charge transfer. According to the linearized Boltzmann equation the Fermi-Dirac distribution f after applying an external electric field is given by:

$$f(\mathbf{k}) \approx f_0(\mathbf{k}) + \frac{e\tau(\mathbf{k})}{\hbar}\mathcal{E} \cdot \quad (2.55)$$

where $f_0(\mathbf{k})$ is the Fermi-Dirac distribution in equilibrium without an external electric field and $\tau(\mathbf{k})$ is the relaxation time of the electrons. The current density j can be calculated by integrating the product of $f(\mathbf{k})$ and the velocity $\mathbf{v}(\mathbf{k})$. Regarding that only the electrons at the Fermi surface contribute to the charge transport and that the conductivity is given by $\sigma = j/\mathcal{E}$ one obtains [49]:

$$\sigma = \frac{ne^2}{m^*} \tau(E_F) = e \cdot n \cdot \mu \quad (2.56)$$

where n is the concentration of electrons, m^* the effective mass of the electron, $\tau(E_F)$ the relaxation time of electrons at the Fermi surface and μ is the mobility as defined in Eq. 2.7. Note that this equation is equal to the classical Drude equation (see Eq. 2.8), except the important difference that $\tau(E_F)$ is not the mean free time between collisions of electrons with defects or phonons. In the theory of Sommerfeld not all electrons with a slow drift velocity contributes to the current, but only the fastest near the Fermi surface.

Charge Transport in Organic Molecule Crystals

In highly purified organic semiconductors the movement electrons can be described as plane waves. Here, the charge transport is limited by scattering with phonons and the mobility μ of the charge carriers increases with decreasing temperature T [64]:

$$\mu(T) \propto T^{-n} \quad (2.57)$$

where n is positive number (≈ 1.5 for acoustic phonons). However, below a certain temperature, which increases with an increasing concentration of impurities, the mobility is dominated by hopping of electrons from one molecule to another. As this process is thermally activated, the mobility decreases with decreasing temperature [65]:

$$\mu(T) = \mu_0 \exp\left(-\frac{E_A}{kT}\right) \quad (2.58)$$

where μ_0 is the intrinsic mobility at $T = 0\text{ K}$ and E_A is the mean activation energy which is needed to move a charge carrier from one localized state to another.

The influence of traps can be described by the trap-and-release model. Here, the effective mobility is described by:

$$\mu_{eff} = \mu(T) \frac{\tau_c}{\tau_c + \tau_t} \quad (2.59)$$

where τ_c is the carrier lifetime in the condensed state and τ_t is the time the charge carrier stays in the trap. According to Shockley and Read [66] the ratio of these two times is given by:

$$\frac{\tau_c}{\tau_t} = \frac{N_c}{N_t} \exp\left(-\frac{E_t}{kT}\right) \quad (2.60)$$

where N_c is the effective density of states in the carrier band, N_t is the density of trapping sites and E_t the energy separation between the trap and the carrier band. Inserting Eq. 2.60 in Eq. 2.59 one obtains the Hoesterey-Letson formula for multiple shallow trapping [67]:

$$\mu_{eff} = \mu(T) \left[1 + \frac{N_t}{N_c} \exp\left(\frac{E_t}{kT}\right)\right]^{-1} \quad (2.61)$$

Charge Transport in Disordered Organic Semiconductors

The mobilities in disordered organic semiconductors is several magnitudes lower than in crystals and the charge transport is mainly based on hopping. In the Bässler model [68] for hopping transport one assume that the density of states of the electrons are given by a Gaussian distribution with a width σ and that the jump rate from one state i with the energy E_i to another state j with the energy E_j is given by:

$$\nu_{ij} = \nu_0 \exp(-2\gamma\Delta R_{ij}) \exp\left(-\frac{E_j - E_i - e\mathcal{E}(x_i - x_j)}{kT}\right) \text{ for } E_j - e\mathcal{E}(x_i - x_j) > E_i \quad (2.62)$$

$$\nu_{ij} = \nu_0 \exp(-2\gamma\Delta R_{ij}) \text{ for } E_j - e\mathcal{E}(x_i - x_j) < E_i \quad (2.63)$$

where the prefactor ν_0 is the so called try frequency, γ is the inverse Bohr radius, ΔR_{ij} is the absolute value of the distance between i to j and $\mathcal{E}(x_i - x_j)$ the difference in the electric field. The problem can not be solved analytical, but a Monte Carlo simulation yields the following expression for the mobility [68]:

$$\mu(T) = \mu_0 \exp\left(-\frac{T_0^2}{T^2}\right) \quad (2.64)$$

where μ_0 is the mobility of the undistorted semiconductor at $T \rightarrow \infty$ and $T_0 = 2\sigma/(3k)$.

Chapter 3

Electrochemistry of Semiconductor-Electrolyte Interfaces

Utilizing the concept of a double-gate transistor for a transducer, the question arise how an aqueous ionic electrolyte can act as a top-gate. Of particular interest is the understanding how the potential applied to an electrode immersed in the electrolyte translate into the top-gate potential at the interface to the top-gate dielectric. Furthermore the comprehension of the interactions between the electrolyte and the organic materials is an indispensable prerequisite for a stable operation of the transducer device. The topic of this chapter is to discuss the basics of electrochemistry and the fundamental electrochemical methods allowing to investigate the phenomena occurring at the interface to an electrolyte.

3.1 Basic Principles of Electrochemistry

This section is mainly based on the excellent textbook on metal and semiconductor electrodes from Norio Sato [52] and the definite book on electrochemistry by Allan Bard and Larry Faulkner [27].

3.1.1 The Electrochemical Potential

Generally the thermodynamic state of a system is described by thermodynamic potentials. Although the characterization of the system by each potential is equivalent, it is reasonable to correspond to the conditions the experiment is taking place. In chemistry it is convenient to use either the Gibbs free energy G , for constant temperature T and pressure p , or the Helmholtz free energy F , for constant temperature and volume V . The chemical potential μ_i is defined as the differential energy of an electrically neutral particle i :

$$\mu_i = \left(\frac{\partial G}{\partial x_i} \right)_{p,T,x} = \left(\frac{\partial F}{\partial x_i} \right)_{V,T,x} \quad (3.1)$$

Where x_i is the molar fraction of particle i , and x is the fraction of all other particles. Now, the electrochemical potential $\bar{\mu}_i$ combines the concepts of the chemical potential and electrostatics and is given by the simple relation:

$$\bar{\mu}_i = \mu_i + z_i e \phi \quad (3.2)$$

Here, z_i is the charge number of the component i , e is the elemental charge and ϕ is the inner potential, which is defined as the differential work to transfer a unit positive charge from infinity into the condensed phase. This potential can be subdivided into the outer potential ψ , which is the potential at the closest approach to the charged phase but beyond the influence of image forces, and the surface potential χ . The latter is defined as the differential work to transfer a unit positive charge from the outer potential into the condensed phase and has its origin in surface electric dipoles. Hence, we obtain for the inner potential:

$$\phi = \psi + \chi \quad (3.3)$$

The energy required to transfer a charged particle i from the outer potential to the interior of the condensed phase is called real potential α_i and is given by:

$$\alpha_i = \mu_i + z_i e \chi \quad (3.4)$$

For electrons the real potential equals the negative work function $-\Phi$. An energy scheme of the involved potentials is given in Fig. 3.1.

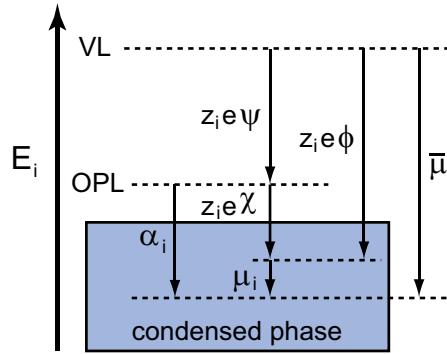


Figure 3.1: Energy level diagram of a charged particle. VL terms the vacuum infinity level and OPL the outer potential level.

3.1.2 The Potential of Electrodes

An electrode is defined as an electronic conductor which allows for the introduction of an electric current or an electric field. Independently of the polarity, an electrode which provides positive charges to an electrolyte is termed *anode* and an electrode which provides negative charges to an electrolyte is termed *cathode* (see Fig. 3.2).

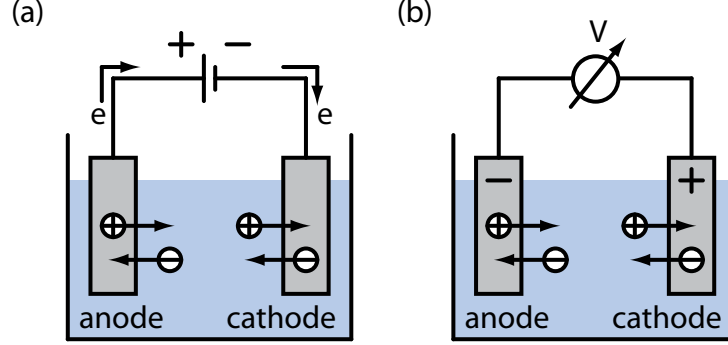


Figure 3.2: Illustrations of (a) electrodes in a material producing electrolytic cell and (b) of electrodes in an electricity-producing voltaic cell.

Electrodes are also classified into electronic and ionic electrodes, depending on whether a transfer of electrons or ions occurs. Furthermore one differentiates between nonpolarizable electrodes (e.g. a Ag/AgCl electrode) and polarizable electrodes (e.g. a Pt-electrode). At the interface of nonpolarizable electrodes a transfer of electrons or ions occurs. The current which is required to establish a charge transfer equilibrium is called *farradaic current*. In contrast, polarizable electrodes allow no transfer of electrons or ions across the electrode interface. The current which is necessary to establish an electrostatic equilibrium is called *nonfaradaic current* or *transient current*.

The electrode potential V is defined by the relation:

$$V = -\frac{\alpha_{e(M/S/V)}}{e} = \frac{\Phi_{(M/S/V)}}{e} \quad (3.5)$$

Where, $\alpha_{e(M/S/V)}$ is the real potential of electrons in the electrode and $\Phi_{(M/S/V)}$ is the work function. The real potential $\alpha_{e(M/S/V)}$ is the sum of the energy of the electron transfer from the standard gaseous state to the electrolyte $\alpha_{e(S/V)} = \mu_{e(S)} - e\chi_{S/V}$ and the energy of the electron transfer from the electrolyte to the electrode $\alpha_{e(M/S)} = \mu_{e(M)} - e\Delta\phi_{(M/S)} - \mu_{e(S)}$. Thus the electrode potential is given by:

$$V = -\frac{\mu_{e(M)}}{e} + \Delta\phi_{(M/S)} + \chi_{S/V} \quad (3.6)$$

The analogous considerations can be applied to the ion energy levels of electrodes.

For an electrode at which the transfer of redox electrons is in equilibrium, $\alpha_{e(M/S)} = 0$ and $\mu_{e(M)} = \mu_{RED(S)} - \mu_{OX(S)}$, where $\mu_{RED(S)}$ and $\mu_{OX(S)}$ are the chemical potential of the reductant and the oxidant, respectively. From Eq. 3.6 we get:

$$V_{eq} = -\frac{\mu_{OX(S)} - \mu_{RED(S)}}{e} + \chi_{S/V} = -\frac{\mu_{OX(S)}^0 - \mu_{RED(S)}^0}{e} + \chi_{S/V} + \frac{kT}{e} \ln \frac{[OX]}{[RED]} \quad (3.7)$$

Where $\mu_{OX(S)}^0$ and $\mu_{RED(S)}^0$ are the standard chemical potentials of the oxidant and reductant and $[OX]/[RED]$ the ratio of the concentrations of oxidant and reductant. Merging

the constants to one constant V_0 , called the standard redox electrode potential, one obtains the famous *Nernst-Equation*:

$$V_{eq} = V_0 + \frac{kT}{e} \ln \frac{[OX]}{[RED]} \quad (3.8)$$

Analogous for ion transfer equilibrium one obtains:

$$V_{eq} = V_0 + \frac{kT}{ze} \ln [M_{(S)}^{z+}] \quad (3.9)$$

Where $[M_{(S)}^{z+}]$ is the concentration of metal ions in the solution [52].

Generally the electrode potential is stated relative to the electrode potential of the standard hydrogen electrode (SHE). As shown in Fig. 3.3 a SHE consists of a Pt-electrode in a solution with a H^+ concentration of 1 M and a tube which bubbles hydrogen gas through the solution at a pressure of 1013 mbar and a temperature of 298,15 K. The absolute potential of the electrode is adjusted by the reaction $2H^+ + 2e^- \rightleftharpoons H_2$ which is catalyzed by the Pt and is given by [69]:

$$V_{SHE} = +4.44 (\pm 0.02) V \quad (3.10)$$

As the standard conditions of a SHE are hard to achieve in a real experiment, usually the SHE is substituted by a so called normal hydrogen electrode (NHE). The NHE is identically designed as a SHE, but is filled with a 1 M hydrochloric acid and works under atmospheric conditions. The discrepancy of the absolute potential of the NHE and the SHE is very small.

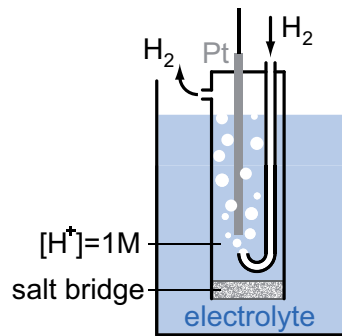


Figure 3.3: Scheme of a standard hydrogen electrode (SHE).

Note that in electrochemistry the electrical potential is abbreviated with the symbol E , while the energy has the symbol ϵ . In order to prevent confusion in this work the notation of physics is used, i.e. V name a potential difference and E an energy.

3.1.3 The Surface of Semiconductor Electrodes

The Electric Double Layer

The potential difference at an electrode/electrolyte interface results in an excess of ions at the electrode surface and a corresponding layer of counter charges. The complete charge distribution at the interface is called electrical double layer. [27] In an aqueous solution the double layer basically consists of three different layers [27, 52]:

- The diffuse layer of excess electrons or holes in the solid phase, also called space charge layer. In semiconductors with a low electron / hole concentration, the thickness of this layer is in the range of 100 to 1000 *nm*.
- The compact or inner layer, consisting of adsorbed water molecules, also called Helmholtz or Stern layer, with a thickness of about 0.3 to 0.5 *nm*. The plane corresponding to the thickness of the water molecule layer is termed inner Helmholtz plane (IHP), the plane corresponding to the closest approach of hydrated ions is called the outer Helmholtz plane (OHP). It is important to realize that the OHP also depends on the surface roughness.
- The diffuse layer of excess hydrated ions is simply called diffuse layer or Gouy layer. For low ion concentrations in aqueous solutions the thickness of this layer is in the range of 10 to 100 *nm*.

A schematic of these three layers are shown in Fig. 3.4 a, the resulting charge and potential distribution in Fig. 3.4 b and Fig. 3.4 c, respectively.

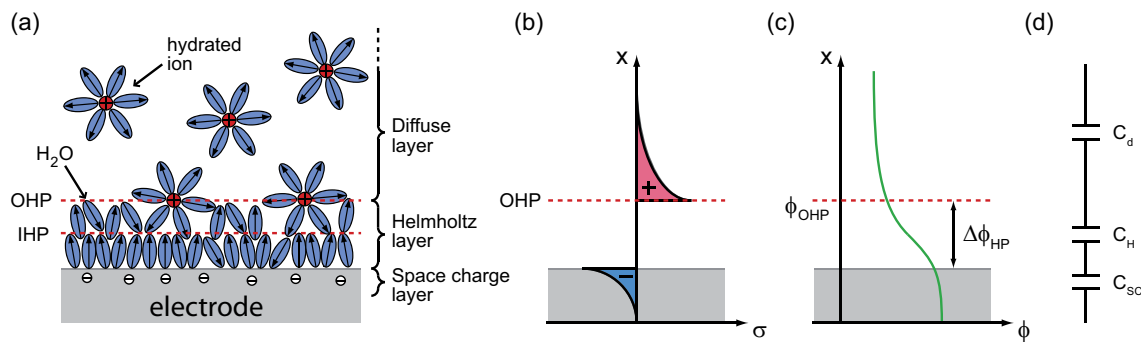


Figure 3.4: (a) Schematic assembly of the electric double layer. (b) Charge distribution, (c) Potential distribution and (d) Equivalent circuit of the triple-layer model of the electric double layer

In this so called triple-layer model, the capacitance of the electric double layer can be represented by three capacitances in series: the capacitance of the space charge layer C_{SC} , the Helmholtz layer capacitance C_H and the diffuse layer capacitance C_d (see Fig. 3.4 d). The total capacitance of the electrical double layer C_{dl} is given by:

$$\frac{1}{C_{dl}} = \frac{1}{C_{SC}} + \frac{1}{C_H} + \frac{1}{C_d} \quad (3.11)$$

Adsorption

Basically, one can differentiate between three classes of adsorption of particles on a solid surface. [52] At *physisorption* particles are attached to the surface due to Van der Waals' forces and tend to form a closed packed two-dimensional structure. In contrast, *chemisorption* describes the adsorption of atoms, ions or molecules due to covalent, metallic or ionic binding. *Contact adsorption of ions* occurs when hydrated ions are first dehydrated and then adsorbed at the inner Helmholtz plane of the compact layer. The resulting charge and potential distributions are shown in Fig. 3.5.

When a particle approaches a conductive surface the HOMO and LUMO levels of the particles are broaden into bands, whose width depends on their position relative to the band structure of the electrode material. Moreover, the position of these bands are shifted by a magnitude equivalent to the adsorption energy. Charge transfer can occur between the adsorbed particle and a semiconductor electrode, when the position of the bands of the adsorbed particle matches with the conduction or valence band of the semiconductor.

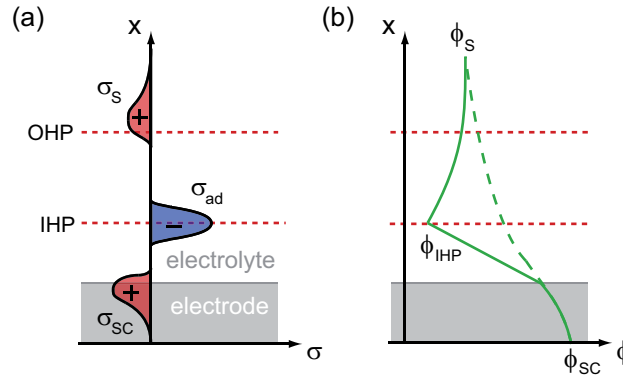
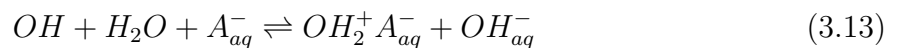


Figure 3.5: Illustration of (a) the charge distribution and (b) the potential distribution without (dashed line) and with contact adhesion of ions to a semiconductor (solid line).

Hydroxylation

It is typically for many semiconductor surfaces to form acid-type or base-type hydroxyl groups. The former can donate a proton as an acid, the latter can accept a proton as a base:



Where K_{aq}^+ and A_{aq}^- is a hydrated cation and hydrated anion, respectively. Disregarding a constant term the resulting shift of the potential of the compact layer is proportional to the pH value of the solution [52]:

$$\Delta\phi_H = 2.3 \frac{kT}{e} (pH) \quad (3.14)$$

This relation allows for the use of SiO_2 as the active material of an ISFET, as discussed in section 1.2.1. On the other hand this phenomena can cause problems, when SiO_2 is used as bottom-gate dielectric of double-gate TFT transducers.

Surface States

It is possible to distinguish two groups of surface states: surface states of short relaxation times ($10^{-3} - 10^{-6}s$), originating from intrinsic surface states like dangling bonds (see section 2.1.2), and surface states of long relaxation times ($\approx 1s$), originating from extrinsic states due to adsorbed particles. [52]

Surface states can play a crucial role at semiconductor interfaces as they can be charged and discharged like a capacitor and thus changes the impedance of the whole interface. The situation may be illustrated by an equivalent circuit with an additional capacitance C_{SS} and resistor R_{SS} in parallel to the space charge capacitance C_{SC} , see Fig. 3.6.

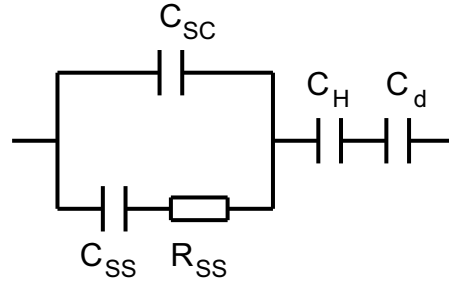


Figure 3.6: Equivalent circuit of electric double layer with surface states: C_{SC} is the capacity of the space charge layer, C_{SS} the capacity of the surface states, R_{SS} the resistance of charging and discharging the surface states, C_H the capacity of the compact layer and C_d capacity of the diffuse layer.

Additional to the phenomena described above surface states can give rise to band edge level pinning or Fermi level pinning. In the first case the change in electrode potential occurs across the space charge layer, while in the second case the change occurs across the compact layer.

3.1.4 Electrode Reactions

In this section the transfer of electrons and ions at semiconductor electrodes is discussed. The prerequisite for the understanding of these reactions is the treatise of the energy levels of electrons in aqueous solutions, what will be the matter of the first subsection.

The Energy Levels of Electrons

For electrons the charge number in the equations for the electrochemical potential (Eq. 3.2) and the real potential (Eq. 3.4) is given by $z_i = -1$. The chemical potential μ_e of electrons in metals can be split in two contributions the exchange and correlation potential V_{ex} , which characterize the effects of the Pauli principle and Coulomb potential beyond pure electrostatic interaction, [70] and the kinetic energy U_e :

$$\mu_e = V_{ex} + U_e \quad (3.15)$$

Here, the energy levels of redox electrons in aqueous solutions are of main interest. A redox reaction is defined as a chemical reaction in which an electron transfer occurs from one reactant, termed reductant (RED), to another reactant, termed oxidant (OX):



The electron donating process is called oxidation, while the electron accepting process is called reduction.

In water the donor level E_{RED} differs from the acceptor level E_{OX} by the energy, which is necessary for the reorganization of the hydrate structure, which occurs immediately after the electron transfer:

$$E_{OX} - E_{RED} = \lambda_{OX} + \lambda_{RED} \quad (3.17)$$

Where λ_{OX} is the reorganization energy of the oxidant and λ_{RED} is the reorganization energy of the reductant. It is notable that the energy levels of hydrated species in aqueous solutions fluctuates in the range of the reorganization energy, due to thermal motions. The fluctuation can be approximated by a Gaussian normal distribution, with E_{RED} and E_{OX} as most probable levels, respectively. Analogous to an intrinsic semiconductor the level E_F^{REDOX} at which the donor state density equals the acceptor state density is termed Fermi level of the redox electron:

$$E_F^{REDOX} = \frac{1}{2}(E_{OX} + E_{RED}) + kT \ln \frac{[RED]}{[OX]} \quad (3.18)$$

Where k is the Boltzmann constant, T the temperature, $[RED]$ the concentration of the reductant and $[OX]$ the concentration of the oxidant.

In Fig. 3.7 the situation for equal reductant and oxidant concentrations is illustrated. For unequal concentrations the Fermi level of the redox electron is shifted towards E_{RED} or E_{OX} , respectively.

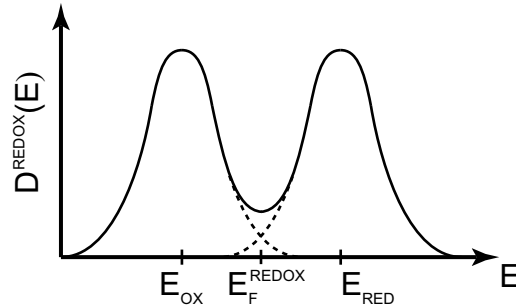


Figure 3.7: Schematic diagram of the distribution of the electron state density of hydrated redox particles

Electron Transfer

In general charge transfer reactions in which a negative charge is transferred to an electrolyte is called cathodic reaction, while the transfer of a positive charge is called anodic reaction. Furthermore, it is possible to differentiate between the electron transfer of hydrated particles at the OHP and adsorbed particles at the IHP. In contrast to metal electrodes the electron state density at the Fermi level of semiconductor electrodes is zero and hence allows no electron transfer. A charge transfer is only possible at the conduction or valence band or at surface states. A typical charge transfer reaction at semiconductor electrodes is the redox electron transfer reaction. The corresponding electron state densities of the semiconductor and redox particles, as well as the resulting exchange reaction current in equilibrium, is shown in Fig. 3.8.

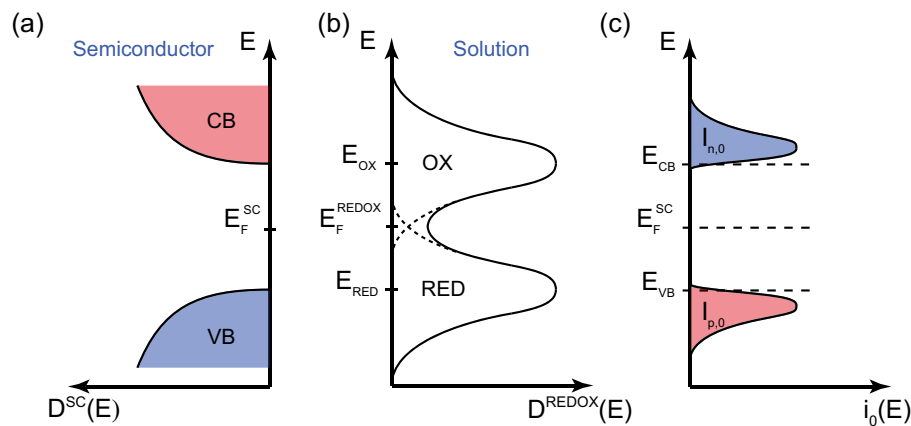
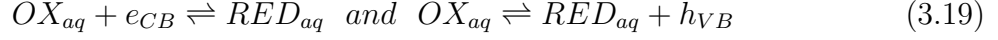


Figure 3.8: Illustration of a redox electron transfer reaction to a semiconductor: (a) Electron state density of a semiconductor, (b) electron state density of redox particles and (c) exchange reaction current in equilibrium ($I_{n,0}$ and $I_{p,0}$ are the electron and hole transfer current in equilibrium).

The general transfer reactions are:



Where the first reaction give rise to an electron transfer current $I_n(E)$ and the second to a hole transfer current $I_p(E)$. The total electron and hole currents are hence given by:

$$I^+(E) = I_n^+(E) + I_p^+(E) \text{ and } I^-(E) = I_n^-(E) + I_p^-(E) \quad (3.20)$$

Where $I_n^+(E)$ and $I_p^+(E)$ are the anodic currents and $I_n^-(E)$ and $I_p^-(E)$ are the cathodic currents. Their magnitude depends on the electron state densities of the semiconductor $D_n^{SC}(E)$ or $D_p^{SC}(E)$ and the redox particles $D^{RED}(E)$ or $D^{OX}(E)$ and the rate constants k_n and k_p (see section 3.2):

$$I_n^+(E) = e k_n(E) D_n^{SC}(E) [1 - f(E - E_F^{SC})] D^{RED}(E) \quad (3.21)$$

$$I_p^+(E) = e k_p(E) D_p^{SC}(E) [1 - f(E - E_F^{SC})] D^{RED}(E) \quad (3.22)$$

$$I_n^-(E) = e k_n(E) D_n^{SC}(E) f(E - E_F^{SC}) D^{OX}(E) \quad (3.23)$$

$$I_p^-(E) = e k_p(E) D_p^{SC}(E) f(E - E_F^{SC}) D^{OX}(E) \quad (3.24)$$

Where $f(E - E_F^{SC})$ is the Fermi-Dirac distribution of the energy difference to the Fermi-level. [52]

The situation is illustrated in Fig. 3.9.

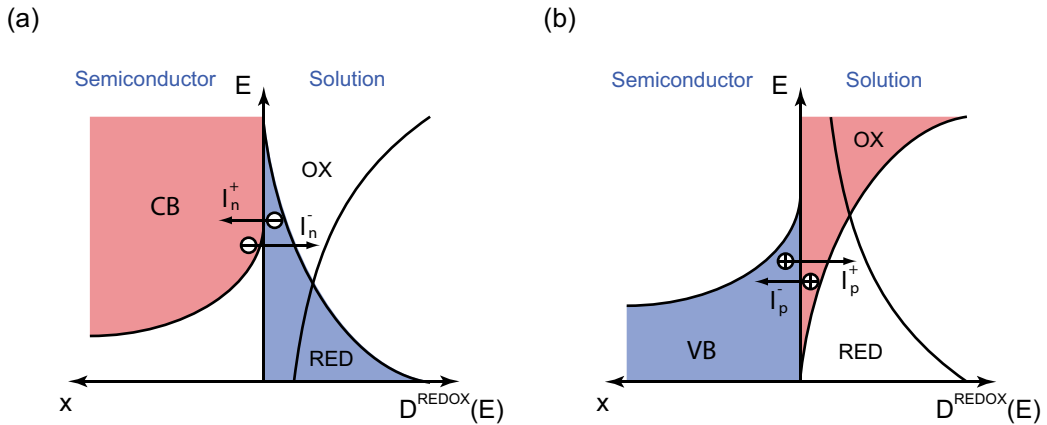


Figure 3.9: Charge transfer between a semiconductor and a redox system: Illustration of an electron transfer (a) at the conduction band and (b) at the valence band.

Analogous to an MS junction (see section 2.1.2) the charge transfer results in an alignment of the Fermi level of the semiconductor E_F^{SC} and the Fermi level of the redox electron (see Eq. 3.18) and the bending of the bands, see Fig. 3.10 a. Typically, the energy band edges are pinned at the interface. The charges cross the interface until it is inhibited by the

potential difference ϕ_{SC} caused by the band bending. The total potential difference across the interface V_E , i.e. the potential applied by an electrode is given by:

$$V_E = \phi_{SC} + \phi_{DL} + C \quad (3.25)$$

where ϕ_{SC} is the potential given by the band bending, ϕ_{DL} is the potential drop across the electric double layer (see Fig. 3.10 b) and C is a constant depending on the nature of the electrode.

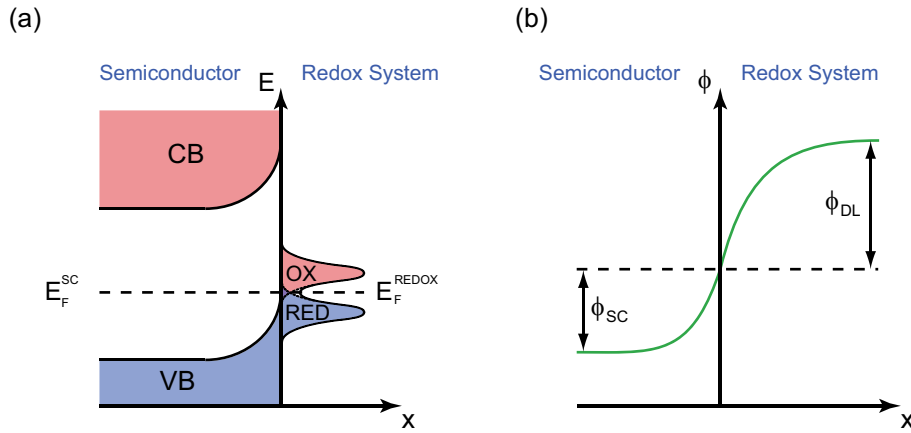
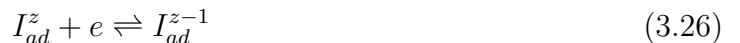


Figure 3.10: Visualization of (a) the band bending of a p-type semiconductor in contact to a redox system and (b) the potential distribution at the interface.

Ion Transfer

Also ion transfer can occur in both directions. Even covalently bonded inorganic semiconductors like Si or Ge are known to dissolve in aqueous solutions. [71] Here the removing of an electron pair from the bonding orbital is followed by the formation of an intermediate surface radical, which is ionized, transferred across the compact layer and finally hydrated. However, the organic semiconductor pentacene which was used in this work, is known for its insolubility and hence this matter will not be discussed in further detail. More relevant is the charge transfer due to the adsorption of ions on semiconductor electrodes, which was already discussed in section 3.1.3. The adhered ion I_{ad}^z with a charge number z establish an interfacial redox reaction system:



Here, the reaction from left to right means that there is an electron transfer from the conduction band of the semiconductor to the adhered ion or a hole transfer from the adhered ion to the valence band of the semiconductor. In equilibrium the Fermi level of the semiconductor and the Fermi level of the interfacial redox electrons equal. Assuming that the concentration of ions $[I_{ad}^z]$ is proportional to the coverage, the Fermi level of the interfacial redox electrons is given by:

$$E_F(I_{ad}^z/I_{ad}^{z-1}) = E_F^0(I_{ad}^z/I_{ad}^{z-1}) + kT \ln \left(\frac{[I_{ad}^{z-1}]}{[I_{ad}^z]} \right) \quad (3.27)$$

Where $E_F^0(I_{ad}^z/I_{ad}^{z-1})$ is the Fermi level at $[I_{ad}^{z-1}]/[I_{ad}^z] = 1$. The Fermi level at the surface of a semiconductor $E_F^{S,SC}$ depends on the potential difference of the space charge layer:

$$E_F^{S,SC} = E_{F,fb}^{SC} - e\Delta\phi_{SC} \quad (3.28)$$

Where $E_{F,fb}^{SC}$ is the Fermi level at flat band potential. From Eq. 3.27 and Eq. 3.28 follows that in equilibrium the ratio of concentrations $[I_{ad}^{z-1}]/[I_{ad}^z]$ depends exponentially from the electrode potential.

For organic semiconductors it is also known that ions can intercalate or diffuse into the bulk region and hence change the electric properties, e.g. by the formation of trap states, doping or dedoping [25].

3.2 Electrochemical Methods

This section gives a short overview on the electrochemical methods which are relevant for the electrochemical characterization of the surfaces in chapter 5.

3.2.1 The Potentiostat

The function of a potentiostat is to adjust a desired potential difference between an electrolyte and an electrode, in spite of changes in the current e.g. due to the electrode reactions discussed above. For this purpose usually a three electrode configuration is used:

- A *working electrode* which is the electrode at which the electrochemical reaction of interest occurs. In general the potential of the working electrode is set to ground.
- A *counter electrode* which sets the potential of the electrolyte versus the potential of the working electrode. Usually an inert, polarizable electrode like a platinum wire or plate is used.
- A *reference electrode* which measures the potential of the electrolyte near the working electrode. Mostly a nonpolarizable electrode like a Ag/AgCl-electrode is used.

The basic principle of a potentiostat is to use the potential measured at the reference electrode to readjust the potential applied at the counter electrode by a feedback circuit, see Fig. 3.11.

Here, an operation amplifier (OPA) constitute a feedback loop by amplifying the potential difference between the positive and negative input:

$$V_{CE} = A(V_i - V_{RE}) \quad (3.29)$$

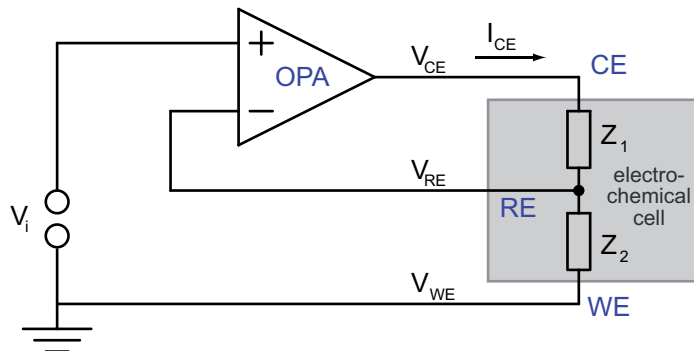


Figure 3.11: Simplified circuit diagram of a potentiostat (WE: working electrode, RE: reference electrode, CE: counter electrode, OPA: operation amplifier)

Where V_{CE} the potential at the counter electrode, A is the amplification factor, V_i the potential applied by a function generator to the amplifier input versus ground and V_{RE} the potential at the reference electrode. The electrochemical cell is simplified by two impedances, Z_1 between the counter and the reference electrode and Z_2 between the working and the reference electrode. As the working electrode is grounded the current through the counter electrode is given by:

$$I_{CE} = \frac{V_{CE}}{Z_1 + Z_2} \quad \text{and} \quad I_{CE} = \frac{V_{RE}}{Z_2} \quad (3.30)$$

From Eq. 3.29 and Eq. 3.30 we obtain:

$$\frac{V_{RE}}{V_i} = \frac{\beta A}{1 + \beta A} \quad (3.31)$$

Where $\beta = Z_2/(Z_1 + Z_2)$. If $\beta A \gg 1$, we get $V_{RE} = V_i$, what is the feedback equation we are looking for.

For interpreting the data provided by a potentiostat it is important to know that the convention of the signs of the voltage and current have historical and not physical origin and is thus inconsistent in literature. The cathodic reaction, i.e. the reduction $OX + ne \rightarrow RED$, occurs when the voltage at the WE is swept from positive to negative values and give rise to a negative current measured at the WE. What actually happens is that the WE is at ground and the voltage of the CE is swept from negative to positive values. It is mostly the convention to plot the decreasing voltage of the WE versus the voltage of the RE and give the cathodic current a positive sign (opposite to the convention in physics). For anodic reactions, i.e. the oxidation $RED \rightarrow OX + ne$, the opposite signs are convention.

3.2.2 The Current in an Electrochemical Experiment

The total current in an electrochemical experiment is composed of three contributions:

- The faradaic current, which originates from electron transfer (see section 3.1.2 and 3.1.4).

- The charging current, which is given by the simple relation $I_{ch} = C \cdot dV/dt$, where C is the capacitance, V the voltage and t the time.
- The ohmic drop.

For the reaction $OX + ne \rightleftharpoons RED$ the faradaic current is related to the rate of the reduction v_{RED} and the rate of the oxidation v_{OX} by:

$$v_{RED} = k_{RED} \cdot [OX_S] = \frac{I_C}{nFA} \quad (3.32)$$

$$v_{OX} = k_{OX} \cdot [RED_S] = \frac{I_A}{nFA} \quad (3.33)$$

Where k_{RED} and k_{OX} are the rate constants of the reduction and oxidation, $[OX_S]$ and $[RED_S]$ are the concentrations of the oxidant and reductant at the electrode surface, I_C and I_A the cathodic and anodic current and A is the active surface area. Assuming an exponential dependency of the rate constants on the electrode potential V , the dependency of the total faradaic current I on the electrode potential is given by the *Butler-Volmer equation*:

$$I = A I_0 \left\{ \frac{[RED_S]}{[RED_B]} \exp \left[\frac{(1 - \alpha)F(V - V_{eq})}{kT} \right] - \frac{[OX_S]}{[OX_B]} \exp \left[-\frac{\alpha F(V - V_{eq})}{kT} \right] \right\} \quad (3.34)$$

Where I_0 is the standard exchange current, $[RED_B]$ and $[OX_B]$ the concentration of the reductant and oxidant in the bulk, α is the transfer coefficient, which is a measure of the symmetry of the energy barrier, F the Faraday constant, and V_{eq} the equilibrium potential from Eq. 3.8. [27] The first term in Eq. 3.34 is the anodic current I_A and the second term the cathodic current I_C , see Fig. 3.12.

The ratio of concentrations of the reductant or oxidant depends on three different mass transport mechanisms:

- Diffusion, which is the movement of particles along a concentration gradient.
- Migration, which is the movement of a charged particle in an electric field.
- Convection, the movement of particles by hydrodynamic transport (thermal motion, stirring etc.).

As the potential is almost constant in an electrolyte, it is reasonable to assume a diffusion limited electrode reaction for an electrolyte which it is not stirred. Considering the reaction $OX + ne \rightarrow RED$, the diffusion flux of the oxidant J_{OX} is given by *Fick's first law*:

$$J_{OX} = \frac{I}{nFA} = -D_{OX} \frac{\partial [OX]}{\partial x} \quad (3.35)$$

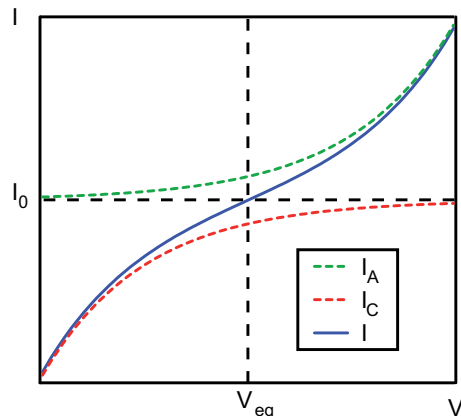


Figure 3.12: Simulated plot of the Butler Volmer Equation. The slashed green line is the anodic current I_A , the red dashed line the cathodic current I_C and the solid blue line the total current $I = I_A + I_C$

Where D_{OX} is the diffusion constant and x is the distance to the electrode. The dependency of the concentration on time is given by *Fick's second law*:

$$\frac{\partial[OX]}{\partial t} = D_{OX} \frac{\partial^2[OX]}{\partial^2 x} \quad (3.36)$$

Solving Eq. 3.36 for a planar electrode and using Eq. 3.35 one obtains the *Cottrell equation* [27]:

$$|I| = \frac{nFA[OX_B]\sqrt{D_{OX}}}{\sqrt{\pi t}} \quad (3.37)$$

This is the basic equation for all amperometric experiments.

3.2.3 Potential Step Methods

Lets first consider a single potential step experiment as shown in Fig. 3.13 a. According to the Butler Volmer equation Eq. 3.34 the current has a peak when the voltage changes from V_1 to V_2 and then decreases indirect proportional to the square root of the time, as predicted by the Cottrell equation Eq. 3.37 (see Fig. 3.13 b). The reason for this behavior is that the initial electrode reaction, e.g. $OX + ne \rightarrow RED$ creates an concentration gradient, which in turn creates a continuing flux of the oxidant to the electrode. This flux causes a depletion zone of the oxidant, which thickness increases with time, see Fig. 3.13 c. The thickness of the depletion layer l can be estimated by the relation $l = \sqrt{\pi D_{OX} t}$. Note that, by fitting the curve of decreasing current in Fig. 3.13 b, it is possible to determine the diffusion constant D_{OX} by Eq. 3.37.

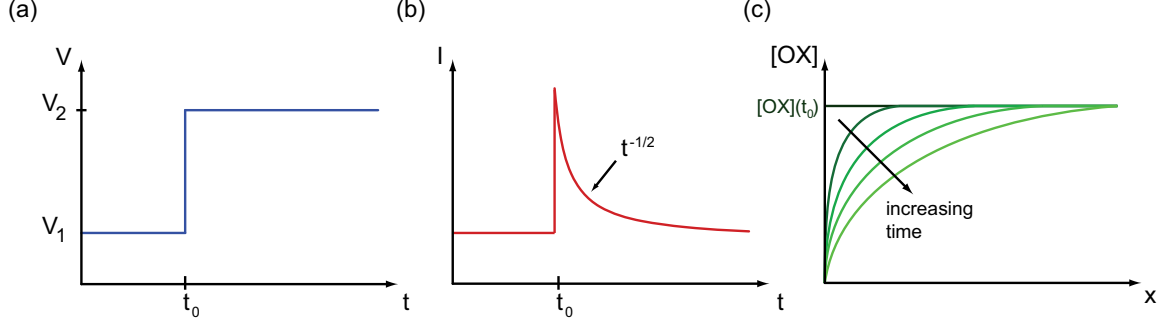


Figure 3.13: Illustration of a Single Potential Step Experiment: (a) Voltage applied at the working electrode, (b) measured current according to the Cottrell Equation and (c) time-development of the concentration $[OX]$ versus distance to the electrode x .

Multistep experiments can be explained by repeating the arguments discussed above. If, for example, after a certain period of time, the voltage is set back from V_2 to V_1 , there will be a peak with opposite sign, as the concentration of *RED* is very high at the interface. Then the current will decline back to the steady state current due to the depletion effect.

A similar behavior can be observed when a certain amount of a reactant is injected into the electrolyte. However, due to the induced convection the system is not under pure diffusion control anymore and Eq. 3.37 is no longer valid.

3.2.4 Voltammetry

In a linear voltammetry experiment the current is measured while applying a linear voltage sweep: $V(t) = V_i - vt$, where V_i is the initial voltage at which the system is in equilibrium and no electrode reaction occurs, v is the sweep velocity and t the time, see Fig. 3.14 a. The behavior of the current for the electrode reaction $OX + ne \rightleftharpoons RED$ can be understood by inserting $V(t)$ in the Nernst equation 3.8. A detailed analysis of the problem is given in [27] and results in an expression for the current which is proportional to the initial concentration of the oxidant and the square root of the sweep velocity v . The resulting current is shown in Fig. 3.14 b.

The distribution of the current can be explained qualitatively by regarding that initially there is a sufficient amount of the oxidant at the electrode surface and hence the current is limited by the kinetics of the electrode reaction according to Eq. 3.34. This gives rise to the exponential increase of the current in the beginning, see Fig. 3.14 b. However, at a certain time t_p and voltage V_p the current peaks as there is no more oxidant left at the surface and the current is limited by diffusion, similar to the potential step method described above, see Fig. 3.14 c. This region is also called Cottrell area.

The peak current I_p is given by [27]:

$$I_p = 0.4463 F \sqrt{\frac{e}{kT}} n^{3/2} A D_{OX} [OX](t_0) \sqrt{v} \quad (3.38)$$

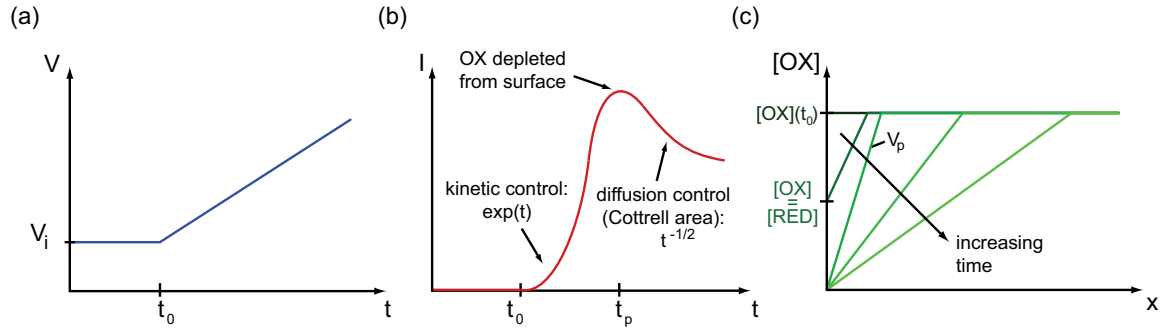


Figure 3.14: Illustration of a Linear Potential Sweep Experiment: (a) Voltage applied at the working electrode, (b) measured current and (c) time-development of the concentration $[OX]$ versus distance to the electrode x .

Note that this equation is not valid, when the oxidant sticks at the surface. In this case, the peak current is proportional to the sweep velocity.

The peak voltage V_p is given by [27]:

$$V_p = V_{1/2} - 1.109 \frac{kT}{ne} = V_{1/2} - \frac{28.5mV}{n} \text{ at } 25^\circ C \quad (3.39)$$

Where the half wave potential at $I = I_p/2$ is given by $V_{1/2} \equiv V^0 + kT/(ne) \ln(D_{RED}/D_{OX})^{1/2}$.

Now lets go a step further and consider a cyclic voltammetry experiment, where a triangular voltage is applied (see Fig. 3.15 a).

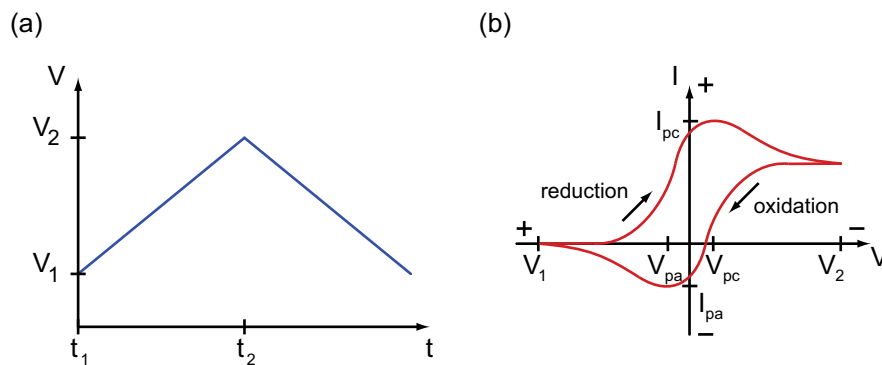


Figure 3.15: Illustration of a Cyclic Voltammetry Experiment: (a) Voltage applied at the working electrode and (b) measured current.

The current for a full reversible (also called 'nernstian') electrode reaction is plotted in Fig. 3.15 b. The current distribution can be explained by applying the same arguments to the oxidation than to the reduction, explained above. The voltage separation between the peak of the cathodic reaction V_{pc} and anodic reaction V_{pa} at ideal conditions is resulting from Eq. 3.39 and is:

$$\Delta V_p = V_{pa} - V_{pc} = \frac{57mV}{n} \text{ at } 25^\circ C \quad (3.40)$$

Furthermore, in a fully reversible electrode reaction the position of V_{pc} and V_{pa} do not depend on the sweep velocity v , whereas the peak currents are proportional to the square root of the sweep velocity. The ratio of the peak currents equals minus one.

In a quasi-reversible electrode reaction the reduction and oxidation rates have different values. With decreasing rate constants the voltage separation increases as a function of the scan rate, as the equilibrium at the surface is established slower. For similar reasons also the peak heights decreases with decreasing rate constants. In a non-ideal experiment also charging currents occur, which are the reason why there is still a separation of the forward- and backward-sweep curves when the faradaic currents are subtracted from the total current.

For semiconductor electrodes the situation is more complex as the kinetic limited region is not sufficiently described by the Butler-Volmer Eq. 3.34 but by Eq. 3.21 - 3.24. Moreover, one has to account for transitions to surface states, see section 3.1.3. Finally, the bending of the bands by the applied electrode potential determines the conductivity of the semiconductor and hence the current measured at the working electrode.

3.2.5 Impedance Spectroscopy

Analogous to the resistance in DC circuits, the complex impedance of an AC circuit is defined as:

$$Z = |Z| \exp(i\theta) = Z_{Re} + iZ_{Im} = \frac{V(t)}{I(t)} \quad (3.41)$$

Where $|Z|$ is the magnitude of the impedance, $\theta = \phi_V - \phi_I$ the phase difference between voltage and current, Z_{Re} the real part of Z , Z_{Im} the imaginary part of Z , $V(t)$ is given by $V(t) = |V| \exp[i(\omega t + \phi_V)]$ and $I(t)$ is given by $I(t) = |I| \exp[i(\omega t + \phi_I)]$. Here $|V|$ and $|I|$ are the magnitudes of the voltage and the current, ω is the angular frequency, t the time, ϕ_V the phase of the voltage and ϕ_I the phase of the current. The complex impedance plane is illustrated in Fig. 3.16.

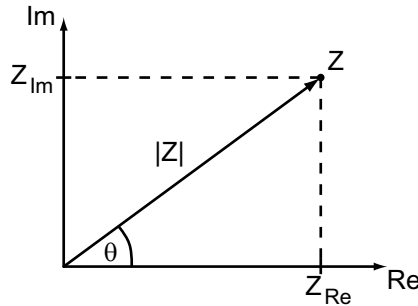


Figure 3.16: Sketch of the complex impedance plane

In an impedance spectroscopy experiment usually the frequency of the applied AC voltage is swept in a certain range while the current is measured. By modeling the electrochemical cell by an appropriate equivalent circuit it is possible to get detailed information about the build-up of the electrode. The real part of the impedance can be assigned to a resistance R , while the imaginary part of the impedance can be assigned to a capacitance C or an inductance L . However, the latter is usually irrelevant for electrochemical methods. As an ideal resistor shows no frequency dependency the real part of Z is given by $Z_{Re} = R$ and $\theta = 0^\circ$. In contrast the impedance of a capacitor C depends on the frequency and the imaginary part of the impedance is given by $Z_{Im} = 1/\omega C$ and $\theta = -90^\circ$. The complex impedance plane of an impedance spectroscopy measurement of a single resistor or a single capacitor is shown in Fig. 3.17 a and 3.17 c, respectively. The corresponding plots of the impedance and phase angle versus the logarithm of the angular frequency, so called Bode plots, are shown in Fig. 3.17 b and 3.17 d, respectively.

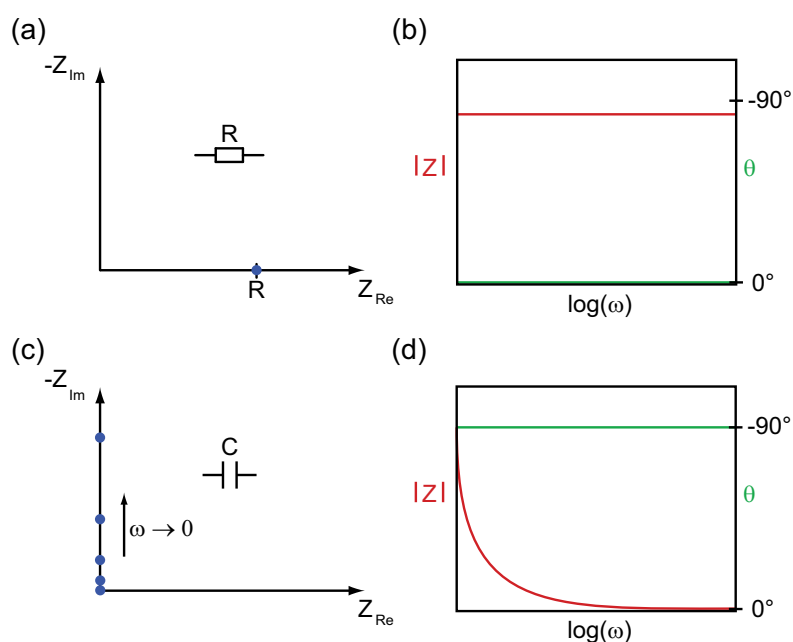


Figure 3.17: Illustration of Impedance Spectroscopy of a single resistor or capacitance: (a) Complex impedance plane of a single resistor, (b) Bode plot of a single resistor ($|Z|$: red curve, θ : green curve), (c) Complex impedance plane of a single capacitor, (d) Bode plot of a single capacitor ($|Z|$: red curve, θ : green curve).

All relevant equivalent circuits in electrochemistry can be composed either by elements of a resistor and a capacitance in series or by elements of a resistor and a capacitance in parallel. In series the data points in the complex impedance plane are just shifted by a value R along the real part axis of the impedance and the Bode plot is dominated by the capacitance. In parallel the data points in the complex impedance plane describe a semi circle with a diameter of R and the Bode plot is dominated by the capacitance at high frequencies and by the resistance at low frequencies. The complex impedance plane and

the Bode plots of these two elements are illustrated in Fig. 3.18.

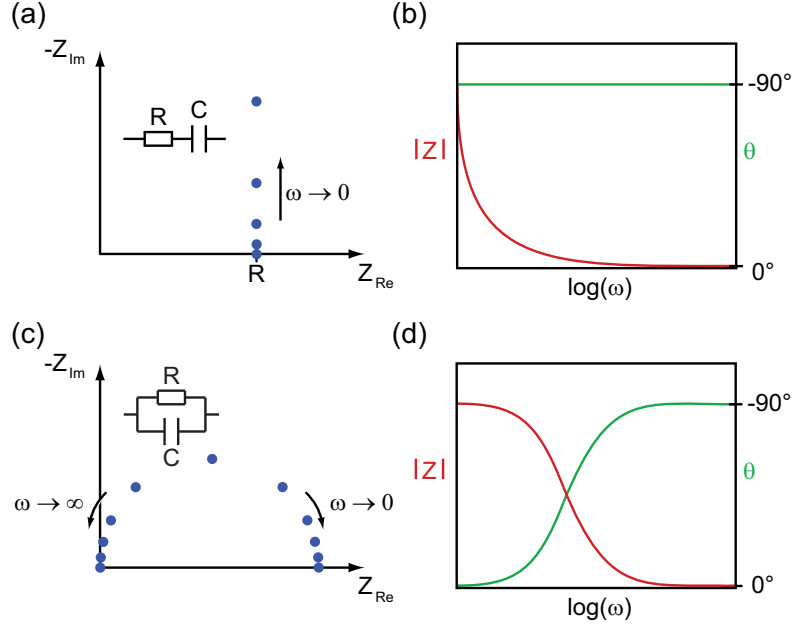


Figure 3.18: Illustration of Impedance Spectroscopy of a resistor and capacitance in series or in parallel: (a) Complex impedance plane of a resistor and capacitance in series, (b) Bode plot of a resistor and capacitance in series ($|Z|$: red curve, θ : green curve), (c) Complex impedance plane of a resistor and capacitance in parallel, (d) Bode plot of a resistor and capacitance in parallel ($|Z|$: red curve, θ : green curve).

In the simplest case an electrochemical cell may be illustrated by the solution resistance R_Ω in series with the capacitance of the double layer C_{dl} (compare Fig. 3.4) and the faradaic impedance Z_f in parallel, see Fig. 3.19 a. The faradaic impedance Z_f , originating from the faradaic current, can be subdivided either in a series resistance R_s and a pseudocapacity C_s in series, or in a charge transfer resistance R_{ct} and the Warburg impedance Z_W , which originates from mass transfer mechanisms in the electrolyte, see Fig. 3.19 b. A detailed description of the equivalent circuit components can be found in [27]. The impedance plot of the equivalent circuit is shown in Fig. 3.19 c. As expected from the considerations above, the impedance describes a half circle with a diameter R_{ct} , which is shifted by R_Ω . As at low frequencies the current is limited by mass transport the curve increases linear below a certain frequency.

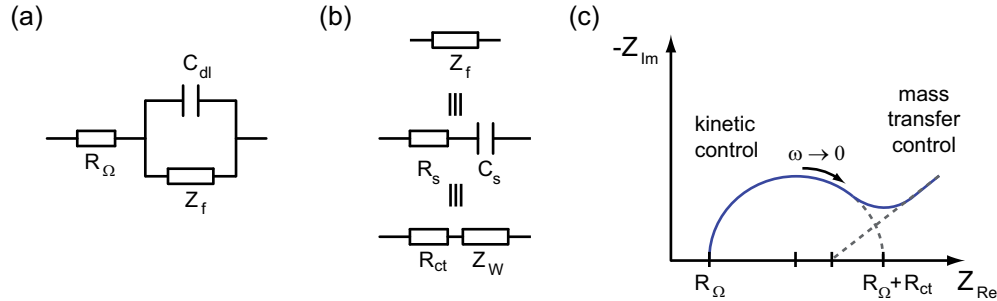


Figure 3.19: (a) Equivalent circuit of a typical electrochemical cell, consisting of the solution resistance R_Ω , the capacitance of the double layer C_{dl} and the faradaic impedance Z_f . (b) The faradaic impedance can be subdivided either in series resistance R_s and a pseudocapacity C_s or in a charge transfer resistance R_{ct} and the Warburg impedance Z_W . (c) Impedance plane plot for the equivalent circuit of (a). According to [27].

At semiconductor electrodes, aside from the more complex kinetics occurring at the interface (see section 3.1.4), the capacitance and resistance of the electrode is changing with the electrode potential. Therefore, in order to investigate the latter, it is reasonable to apply a DC offset voltage to accomplish a region of operation where no faradaic currents occur.

Chapter 4

Materials

4.1 The Organic Semiconductor Pentacene

4.1.1 Structural and Electronic Properties

Pentacene ($C_{22}H_{14}$) is a polyacene consisting of five linearly-fused benzene rings (see Fig. 2.17). Its p-type semiconducting properties origin from the conjugated π -orbital system with alternating double and single bonds, as discussed in section 2.4.1. Due to its highly-ordered crystalline growth, pentacene shows a superior mobility compared to most other organic semiconductors. [72] However, the charge transport mechanism is not yet fully clarified. As the mean free path of holes are smaller than the lattice constant, [73] hopping seems to dominate the charge transfer at room temperature. Contrary, bandlike behavior was observed for pentacene thin films on certain substrates like pyrolytic graphite. [74] The bandgap was optical determined to be about 1.82 eV [75] and the valence band edge was determined at -5.1 eV by ultraviolet photoemission spectroscopy (UPS) [76]. Troisi et al. explain this opposed observations by dynamically localization of charge carriers due to fluctuations in the intermolecular transfer integral originating from molecular motions. [77] One of the main disadvantages of the use of pentacene for electronic devices is its instability under exposure of light, air or moisture. The resulting defects can be distinguished in three different types [78], [79]:

- ($C - H_2$)-defect: A ($C - H$) unit of the pentacene molecule is converted to a ($C - H_2$) unit. In the resulting $C_{22}H_{15}$ molecule one of the C -atoms become fourfold and is no longer part of the π -system. Also two ($C - H_2$)-defects can occur creating a dihydropentacene molecule ($C_{22}H_{16}$).
- (O_H)-defect: A dangling bond (see section 2.1.2) of a pentacene molecule is catching an oxygen atom and a pentacenequinone molecule ($C_{22}H_{13}O$) is created.
- ($C - HOH$)-defect: One of the hydrogen atoms is replaced by a hydroxyl radical and pentacenehydroquinone ($C_{22}H_{14}O$) is formed.

The formation of defects can be used to fabricate e.g. humidity sensors based on pentacene TFTs [80], but as they form trap-states in the band gap it is usually desirable to suppress these defects.

4.1.2 Thin Film Growth

Pentacene can be deposited by thermal evaporation under high vacuum conditions. For this purpose we used a home-made UHV (ultra high vacuum) chamber (see Fig. 4.1 a) which allows for the installation of different types of evaporation cells, the interception of the molecular beam by a shutter, the read-out of the deposition rate at the shutter and at the samples by quartz microbalance sensors and the control of the substrate temperature by halogen bulbs. The substrate temperature was measured by a Pt-100 temperature sensor. Self-made tantalum bags, which could be heated by electric current, were used for the evaporation of pentacene (see 4.1 b).

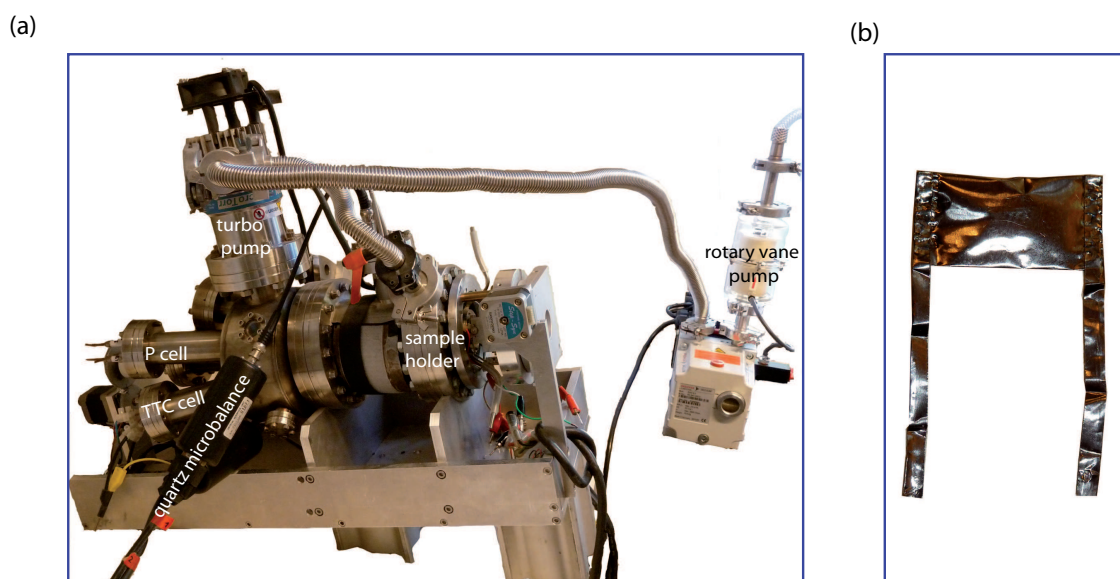


Figure 4.1: (a) Photograph of the UHV evaporation chamber. (b) Tantalum effusion cell for Pentacene.

The control of the substrate temperature and the evaporation cell current as well as the read-out of the substrate temperature, deposition rate and the total film thickness was arranged by a self-made Lab-View program (see Fig. 4.2).

The growth of pentacene strongly depends on the deposition rate, the nature of the substrate, the substrate temperature and the vacuum conditions. [81] In this work the optimum parameters to obtain highly crystalline pentacene thin films turned out to be a deposition rate of about 0.1 \AA s^{-1} , a substrate temperature of $30 - 40^\circ\text{C}$ and a pressure smaller than 10^{-7} mbar . The substrates used in this work were thermally grown SiO_2 , Si_3N_4 and polycrystalline Au . As the hydrophobicity of the substrate is a further decisive influence on

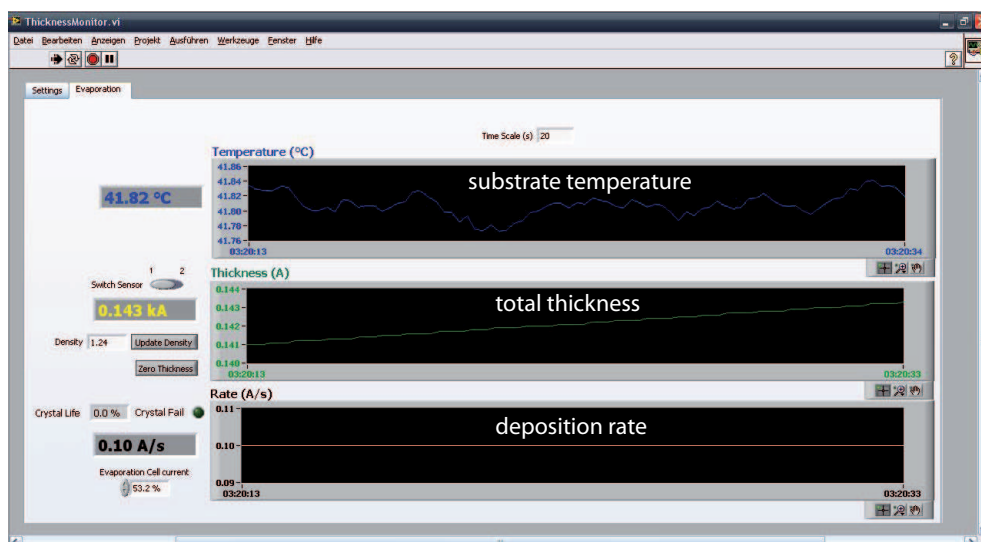


Figure 4.2: Screenshot of self-made LabView program for molecular beam deposition.

the growth of pentacene we spin-coated a very thin film of the hydrophobic cyclic olefin copolymer (COC) Topas® of different chain-lengths on top of the substrates. Under such conditions pentacene grow in grains with a size of about $1\ \mu\text{m}$ with a terraced structure which associates to single molecular layers with a height of $15.4\ \text{\AA}$ [82]. This so called thin-film phase can be assigned to a herringbone structure, i.e. the pentacene molecules are alternately tilted by an angle of 54° and the long molecular axis is tilted relatively to the surface normal by an angle of 6° , see Fig. 4.3.

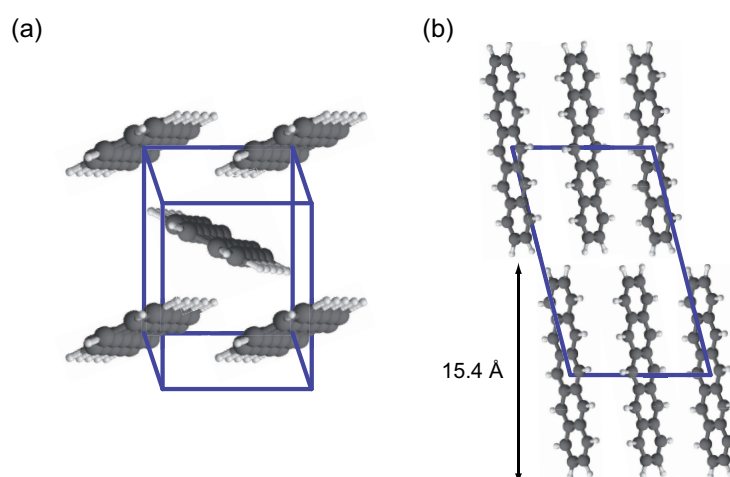


Figure 4.3: Illustration of the herringbone structure of pentacene: (a) top view and (b) side view.

It turned out that although the Si_3N_4 substrates show a rougher surface than thermally grown SiO_2 , the modification by the COC layer results in a comparable morphology than

COC modified SiO_2 (see atom force microscopy (AFM) micrographs Fig. 4.4 a and Fig. 4.4 b). In contrast, the morphology of pentacene on a polycrystalline Au substrate is more rugged. Here, the first monolayer is oriented with the long axis parallel to the surface [83] and the pentacene molecules above form small grains as shown in Fig. 4.4 c. This in turn results in a degradation of the electronic properties of pentacene. We managed to overcome this problem by spin coating a COC layer on top. Fig. 4.4 d shows that this modification allows for a thin film growth comparable to this on Si_3N_4 or SiO_2 . Despite a thickness of a few nanometers, the COC layer still allows a charge injection from the gold substrate to the pentacene layer.

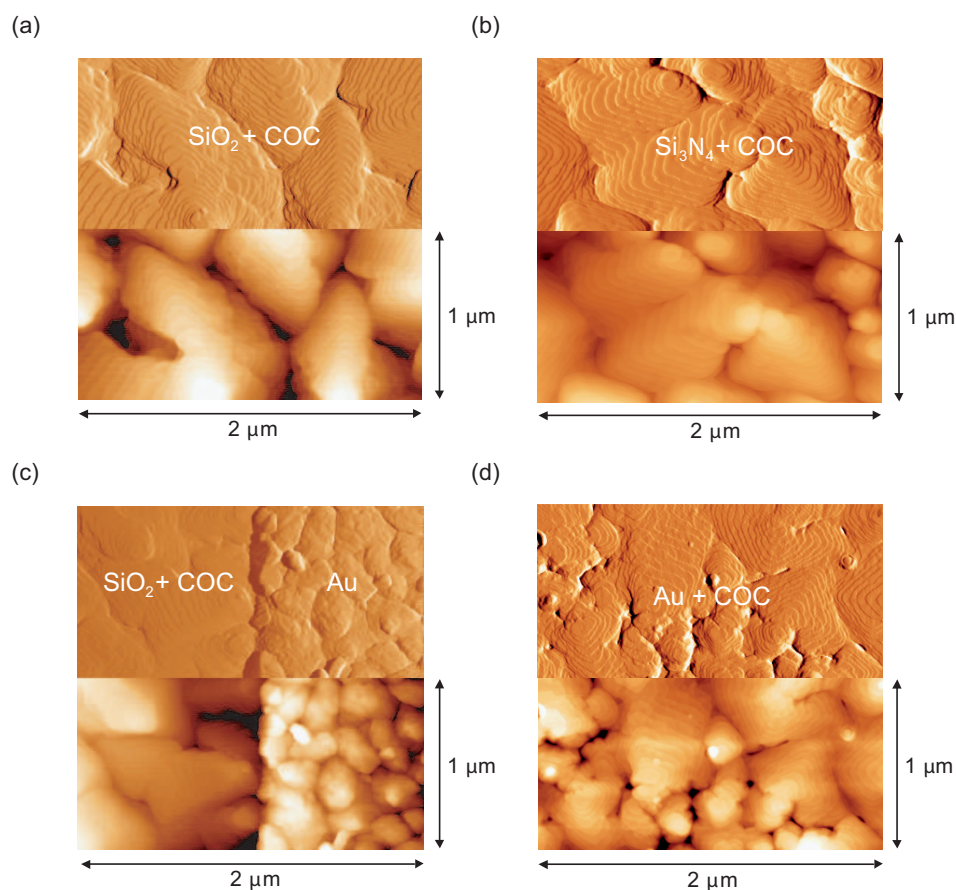


Figure 4.4: AFM amplitude and height micrographs of pentacene thin films on (a) a SiO_2 substrate modified with COC, (b) on a Si_3N_4 substrate modified with COC, (c) on a SiO_2 substrate modified with COC next to a bare Au surface and (d) on a Au substrate modified with COC.

The SiO_2 surface was also modified by silanization with octadecyltrichlorosilane (OTS) or hexamethyldisilazane (HMDS). The treatment resulted in significant improvement of the mobility. However, the transistors fabricated on this substrates showed very negative threshold voltages and a very low subthreshold swing. Therefore, these transistors are not suited for the operation at low voltages, what is highly desirable for applications in liquid

environments. The growth was also enhanced by dipping the substrate in hydrofluoric acid (1%) for about one second in order to remove the hydroxyl groups and therefore creating a more hydrophobic surface. As this method often results in a decrease of the breakthrough voltage of the oxide, it is not well suited for the fabrication of transistors. The Au surfaces were also modified by 1-octanethiol solution (NanoThinks™ 8, Sigma Aldrich), which forms a self-assembled monolayer on the Au surface. However, this method did not improve the growth of pentacene in a significant manner.

4.2 The Alkane Tetratetracontane

Tetratetracontane (TTC) is a long-chain alkane ($CH_3(CH_2)_{42}CH_3$, see Fig. 4.5) with a melting point of $358 - 360\text{ K}$, i.e. above room temperature, and forms closely packed and highly crystalline films by thermal vacuum deposition. [84] Like all alkanes TTC is a good insulator with a resistivity greater than $10^{15}\ \Omega \cdot cm$, show a breakdown voltage of about 20 MV/m [85] and is highly hydrophobic. Therefore, it is well suited to protect sensitive organic semiconductors like pentacene from damaging influences like oxygen or humidity. [86] Important for the use in biosensor devices is that the lack of π -electrons results in a chemical inert nature and good biocompatibility.



Figure 4.5: Structure of tetratetracontane (TTC)

4.2.1 The TTC-Effusion-Cell

The technical challenge of the evaporation of TTC is that the evaporation temperature (about 570 K) is much higher than the melting point (about 360 K). This results in leaking of liquid TTC from the evaporation cell and therefore in a strongly fluctuating deposition rate. This problem was solved by tilting the whole UHV chamber by about 10° and the design of a more sophisticated effusion-cell made of steel (see Fig. 4.6 a). The cell has a crucible with a volume of about 0.5 cm^3 , which can be closed by a screw, an outlet port with a diameter of 1 mm and is heated by two halogen bulbs. The cell temperature can be measured by a Pt-100 temperature sensor. The whole fusion cell was thermally and electrically decoupled from the UHV chamber by a ceramic mounting (see Fig. 4.6 b). The basic idea of this design is to reduce the angle of beam spread by the ratio of the length and the diameter of the outlet port. Here, it is important that the so called Knudsen condition is fulfilled, i.e. the mean free path in the evaporation cell must be larger than the diameter of the outlet port. Note that the spatial arrangement of the crucible and the outlet port inhibits a leakage of liquid TTC, see Fig. 4.6 a. The volume of steel was reduced as much as possible in order to decrease the thermal inertia of the cell. A schematic of the molecular beam evaporation of TTC is shown in Fig. 4.7.

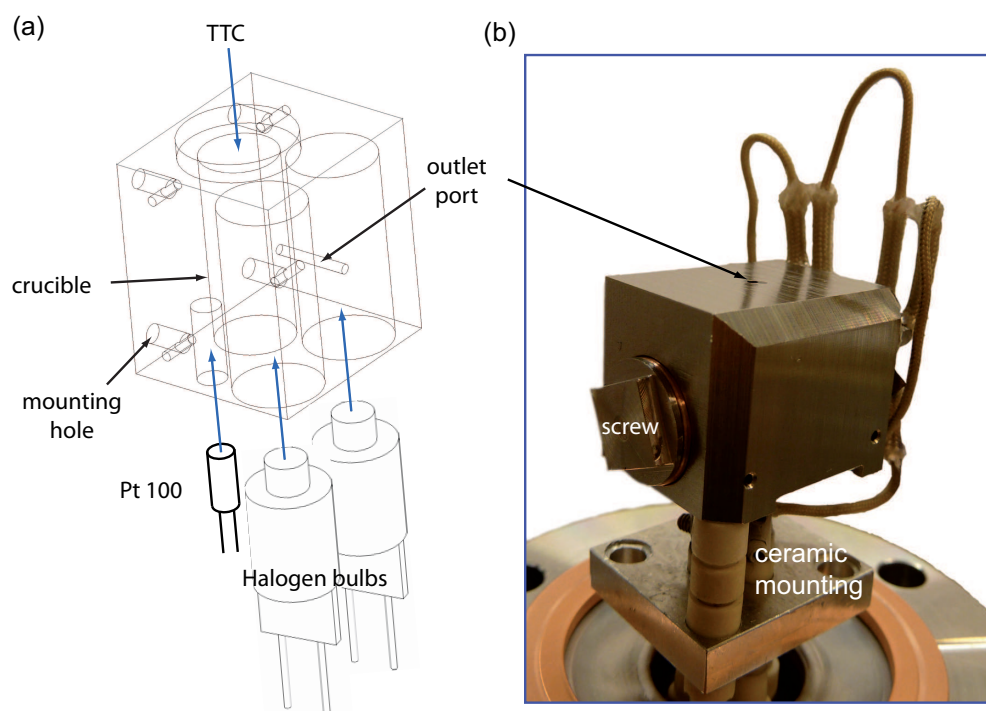


Figure 4.6: (a) Design drawing of the self made effusion cell for the evaporation of TTC. (b) Photograph of the effusion cell mounted on a CF vacuum flange.

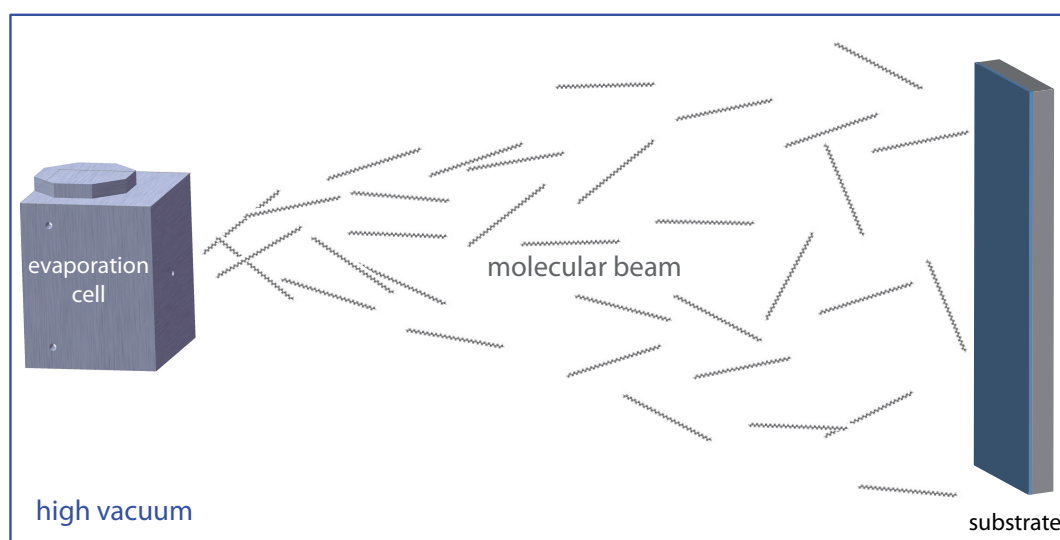


Figure 4.7: Illustration of the basic principle of molecular beam evaporation (not true to scale).

4.2.2 Characterization of Tetratetracontane Thin Films

The use of TTC as a capping layer for sensing devices in aqueous environment necessitates an optimization of the growth parameters in order to obtain a good coverage and an electrically dense layer. For this purpose 50 nm thin films of TTC were grown at different substrate temperatures and different deposition rates on all relevant substrates. In detail, this means on SiO_2 covered by COC, representing the channel region of a TFT, Au , representing the contact region of a top-contact TFT, and Au covered by 50 nm pentacene (P), representing the contact region of a bottom-contact TFT. The Au substrates were also modified by 1-octanethiol SAMs (NanoThinksTM 8, Sigma Aldrich) in order to enhance the growth of pentacene or TTC. The films were characterized by AFM, contact-angle measurements, x-ray reflectometry measurements and current-voltage measurements.

Atomic Force Microscopy Imaging

First we investigated the growth at a low deposition rate (0.1 \AA/s) and a substrate temperature of about 300 K on the substrates mentioned above, see first row of Fig. 4.8. Additionally, the SiO_2 substrates were modified with COC and the Au surfaces with 1-octanethiol SAMs, see second row of Fig. 4.8.

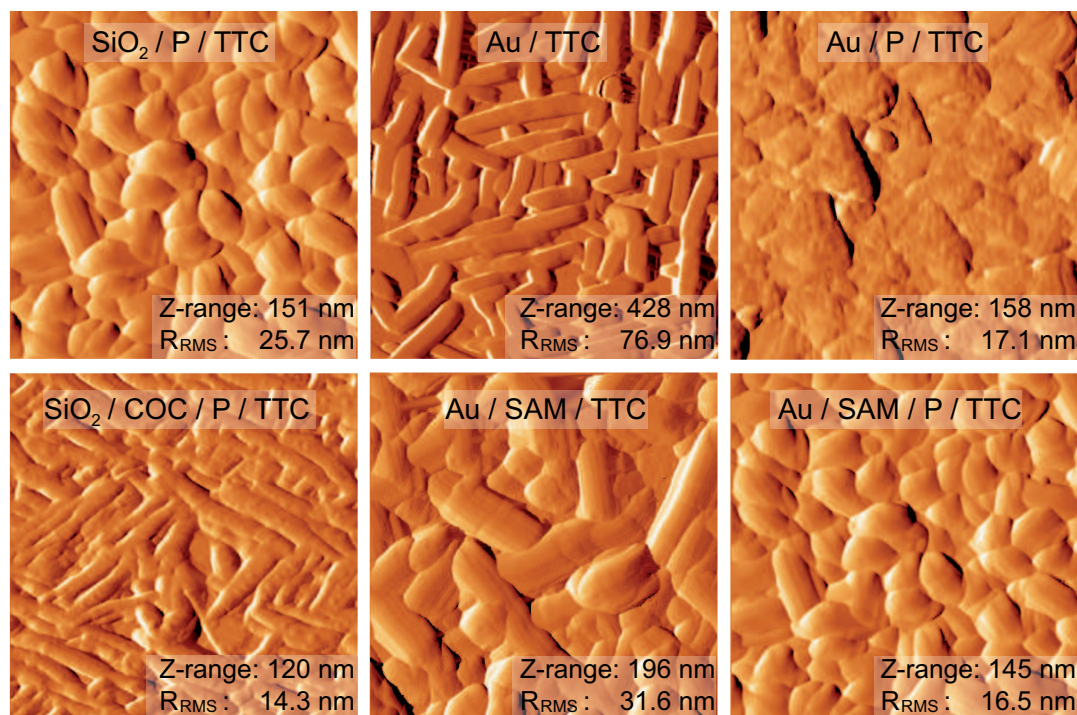


Figure 4.8: Growth of TTC for a low deposition rate and a substrate temperature of about 300 K. The AFM amplitude micrographs have a size of $2 \mu\text{m} \times 2 \mu\text{m}$.

The findings are summarized in the following table:

Substrate	Coverage	Morphology	Grain Size
SiO_2/P	good	round grains	$200\text{ nm} - 400\text{ nm}$
Au	incomplete	rod-like grains	$100\text{ nm} \times \text{max. } 800\text{ nm}$
Au/P	good	flake-like grains	$200\text{ nm} - 500\text{ nm}$
$SiO_2/COC/P$	few pinholes	angled, worm-like grains	$100\text{ nm} \times \text{max. } 800\text{ nm}$
Au/SAM	good	rod-like grains	$300\text{ nm} \times \text{max. } 800\text{ nm}$
$Au/SAM/P$	good	round grains	$200\text{ nm} - 400\text{ nm}$

Note that the growth of TTC on $SiO_2/COC/P$ aligns along the steps of the pentacene thin film phase, resulting in a quite good coverage. However, some pinholes advance to the pentacene layer (see corresponding AFM micrograph in Fig. 4.8) and may cause leakage currents in an electrochemical experiment.

Secondly, we investigated the growth at a low deposition rate (0.1 \AA/s) and a substrate temperature of about 370 K , see Fig. 4.9.

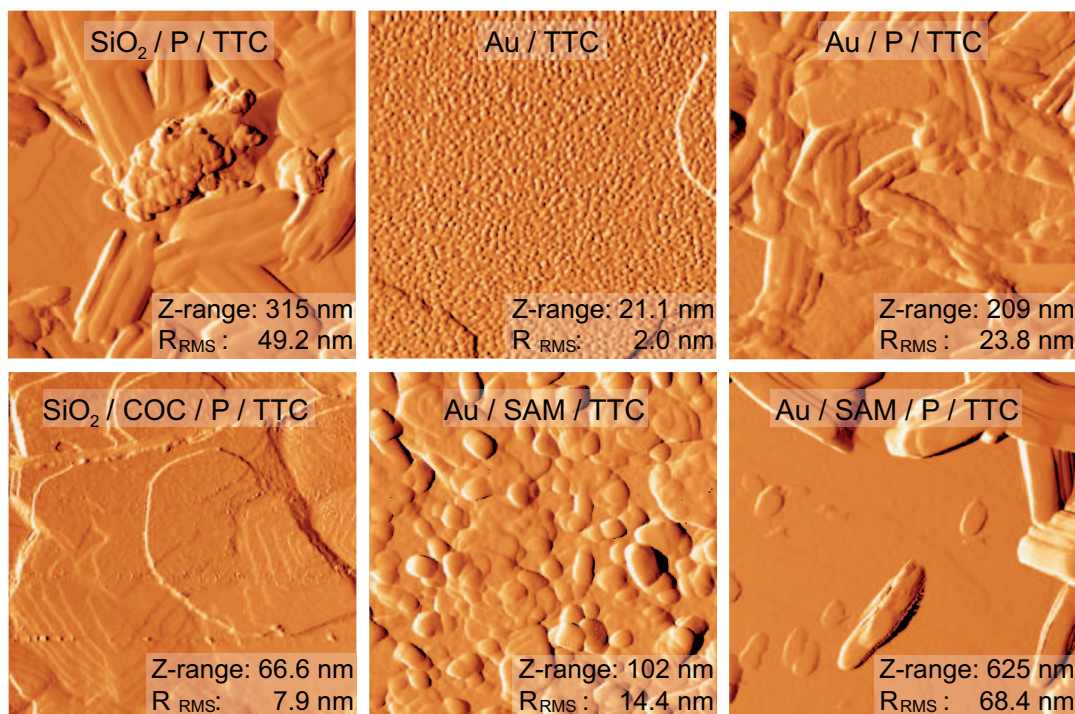


Figure 4.9: Growth of TTC for a low deposition rate and a substrate temperature of about 370 K . The AFM amplitude micrographs have a size of $2\text{ }\mu\text{m} \times 2\text{ }\mu\text{m}$.

As the higher temperature results in a higher mobility of the TTC molecules, one expects that the interaction between the TTC molecules plays a more important role for the growth

than the interaction between the TTC molecules and the substrate. A more detailed discussion on how the interactions between the molecules and substrate influences the growth of TTC can be found in the dissertation of M. Huth [87]. The observations for the different substrates are shown in the following table:

Substrate	Coverage	Morphology	Grain Size
SiO_2/P	poor	mixed	max. 400 nm
Au	very poor	dewetting	-
Au/P	poor	finger-like grains	$100 \text{ nm} \times \text{max. } 400 \text{ nm}$
$\text{SiO}_2/\text{COC}/\text{P}$	very poor	dewetting	-
Au/SAM	good	round grains	max. 100 nm
$\text{Au}/\text{SAM}/\text{P}$	poor	rod-like grains	$200 \text{ nm} \times \text{max. } 600 \text{ nm}$

Obviously the high substrate temperature result in most cases either in dewetting or a highly irregular growth of TTC. Only when TTC is deposited directly on a 1-octanethiol SAM, the molecules form a dense layer consisting of small grains.

Thirdly, we investigated the growth at a high deposition rate ($4 \text{ \AA}/\text{s}$) and a high substrate temperature of about 370 K, see Fig. 4.10.

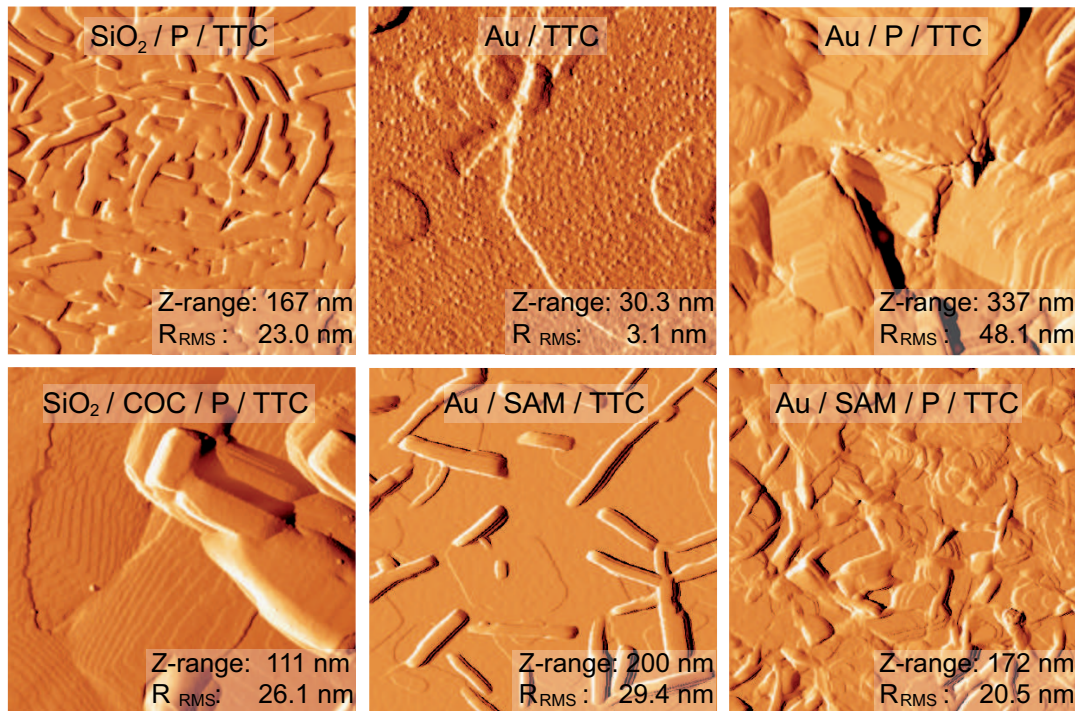


Figure 4.10: Growth of TTC for a high deposition rate and a substrate temperature of about 370 K. The AFM amplitude micrographs have a size of $2 \mu\text{m} \times 2 \mu\text{m}$.

Here, one expect that the higher mobility of the TTC molecules, due to the high substrate temperature, is compensated by the shorter time available for the arrangement of the molecules. The results are presented in the following table:

Substrate	Coverage	Morphology	Grain Size
SiO_2/P	incomplete	rod-like grains	$100\text{ nm} \times \text{max. } 400\text{ nm}$
Au	very poor	dewetting	-
Au/P	incomplete	clod-like, terraced grains	max. 500 nm
$SiO_2/COC/P$	very poor	dewetting	-
Au/SAM	poor	rod-like grains	$100\text{ nm} \times \text{max. } 1\text{ }\mu\text{m}$
$Au/SAM/P$	poor	mixed	$< 200\text{ nm}$

As expected for SiO_2/P , Au/P and $Au/SAM/P$ surfaces the coverage is better than for low deposition rates. However, for Au , $SiO_2/COC/P$ and Au/SAM substrates strong dewetting occurs.

Finally, we investigated the growth at a high deposition rate ($4\text{ }\text{\AA}/\text{s}$) and a substrate temperature of about 300 K , see Fig. 4.11.

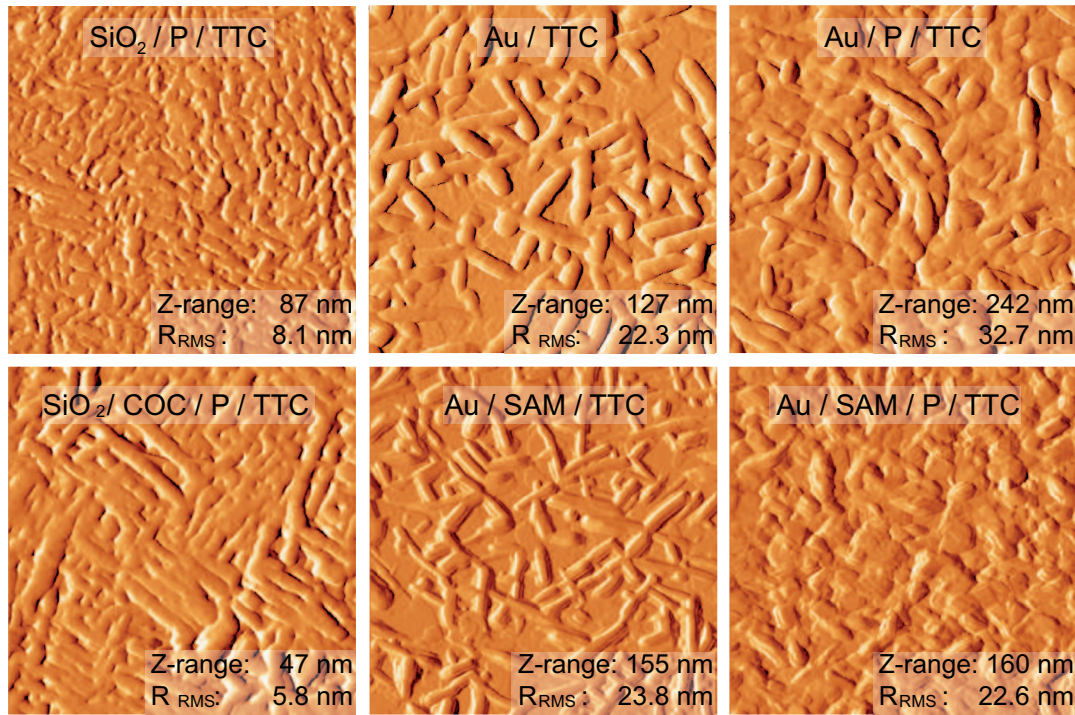


Figure 4.11: Growth of TTC for a high deposition rate and a substrate temperature of about 300 K . The AFM amplitude micrographs have a size of $2\text{ }\mu\text{m} \times 2\text{ }\mu\text{m}$.

For this parameters one expect that the TTC molecules have a low mobility and little time

to arrange on the surface. Therefore, the interaction between the TTC molecules and the substrate should dominate. Here, we made the following observations:

Substrate	Coverage	Morphology	Grain Size
SiO_2/P	very good	worm-like grains	$50\text{ nm} \times \text{max. } 300\text{ nm}$
Au	good	worm-like grains	$100\text{ nm} \times \text{max. } 400\text{ nm}$
Au/P	good	primary worm-like grains	$100\text{ nm} \times \text{max. } 400\text{ nm}$
$SiO_2/COC/P$	very few pinholes	angled, worm-like grains	$100\text{ nm} \times 800\text{ nm}$
Au/SAM	moderate	rod-like grains	$50\text{ nm} \times \text{max. } 400\text{ nm}$
$Au/SAM/P$	good	clod-like grains	$< 200\text{ nm}$

Comparing Fig. 4.11 with the AFM height micrographs for the other sets of parameters, one can say that a low substrate temperature and high deposition rates result in the best coverages and smoothest surfaces on almost all substrates.

X-ray Reflectometry Measurements

In order to discover the orientation of the TTC molecules and if the TTC deposition damages the pentacene layer we also performed x-ray reflectometry measurements at the Hamburger Synchrotronstrahlungslabor (HASYLAB, beamline W1) in Hamburg. As the TTC layer on $SiO_2/COC/P$ show a better coverage than on SiO_2/P for the most relevant substrates (see Fig. 4.8 and 4.11) and the electrical properties of pentacene significantly improves by the use of COC, the SiO_2/P substrates are not further investigated. The sets of parameters was $300\text{ K} / 0.1\text{ Ås}^{-1}$ (cs), $370\text{ K} / 0.1\text{ Ås}^{-1}$ (hs), $300\text{ K} / 4.0\text{ Å/s}^{-1}$ (cf) and $370\text{ K} / 4.0\text{ Ås}^{-1}$ (hf), respectively. Fig. 4.12 a and b shows that the thin film phase of pentacene [82] (00l-series, green lines) on $SiO_2/COC/P$ substrates is conserved and therefore the TTC deposition does not damage the pentacene thin film phase. Using the orthorhombic structure assumed by Craig et al. [88] and Nyburg et al. [89], the peak at 1.525 Å^{-1} can be identified with (110) plane, 3.05 Å^{-1} with the (220) planes and the peak at 1.69 Å^{-1} with the (020) plane of TTC. This allows to calculate the unit cell dimensions of $a = 4.96 \pm 0.02\text{ Å}$, $b = 7.43 \pm 0.02\text{ Å}$ and $c = 57.91 \pm 0.02\text{ Å}$. Apparently, the c-axis, i.e. the long axis of the TTC molecule is oriented parallel to the surface. Consequently TTC on $SiO_2 / COC / P$ grows not in a standing phase like on SiO_2 / COC [87] (see Fig. 4.13 a), but in lying phase (see Fig. 4.13 b).

While the (110) and (020) peaks can be observed for all sets of parameters, the (200) peak vanishes for high substrate temperatures. Also the higher orders of the pentacene thin film peaks are suppressed, what may originate from a small influence of the high TTC deposition rate on the pentacene thin film phase. The higher regularity for a low substrate temperature is in agreement with the AFM study presented above. For the Au substrates only the (110) peak of the lying TTC phase is still observed for low substrate temperatures, while no peaks occur for high substrate temperature, indicating an amorphous growth of TTC, see Fig. 4.12 c and d. The huge peak at 2.67 Å^{-1} originates from the Au substrate

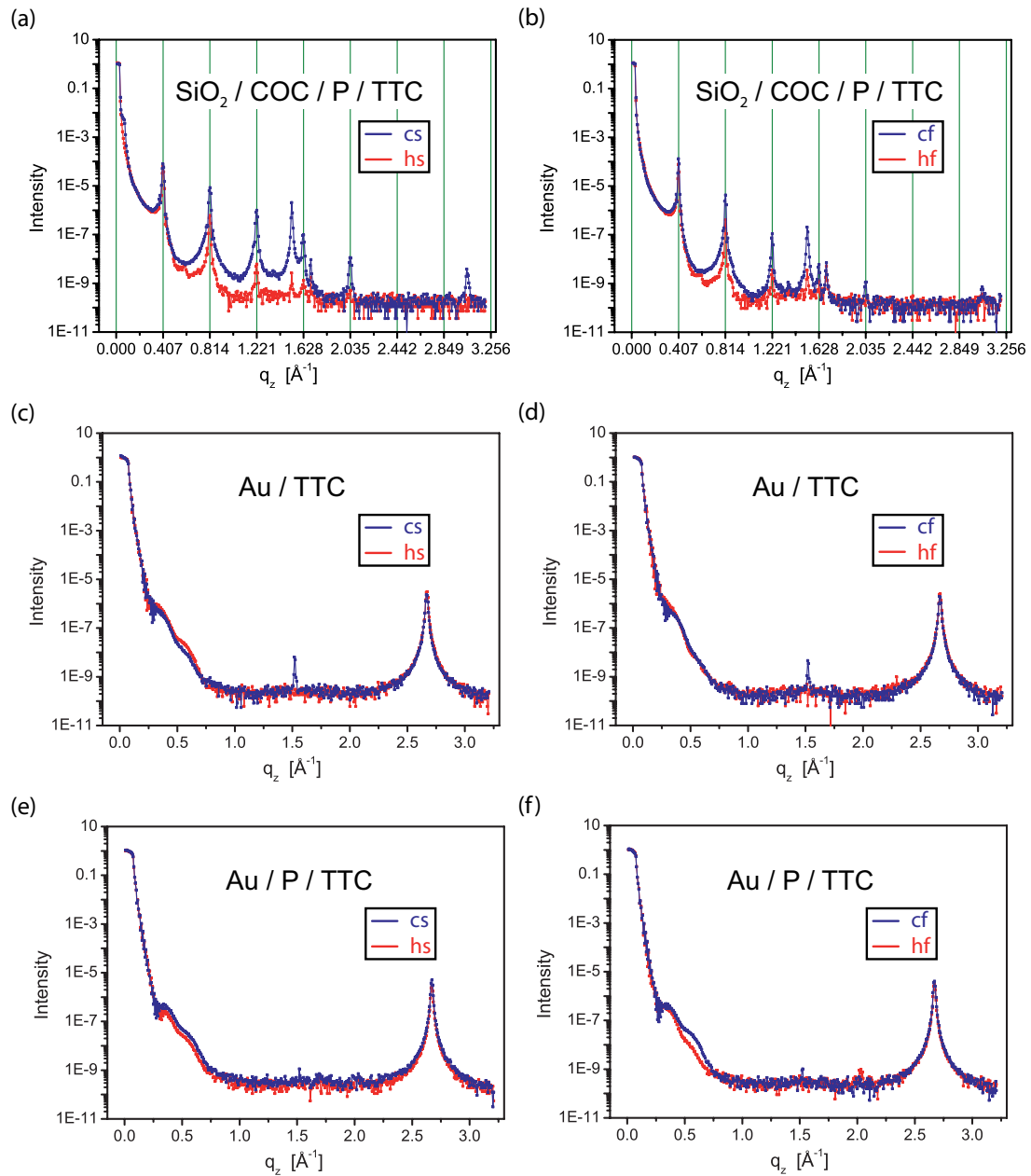


Figure 4.12: X-ray reflectometry measurements of TTC thin films on $\text{SiO}_2/\text{COC}/\text{P}/\text{TTC}$ (a and b), on Au/TTC (c and d) and on $\text{Au}/\text{P}/\text{TTC}$ (e and f) deposited for different substrate temperatures. Additionally, the TTC films were deposited either at a low deposition rate (a, c, e) or at a high deposition rate (b, d, f).

and may cover the (220) peak. Again the measurements are in good agreement with the observations made in the AFM micrographs above. The identical situation appears for the *Au/P* substrate, except from a lower intensity of the (110) peak (Fig. 4.12 e and f). Therefore, in accordance to the AFM study only a small part of the TTC molecules are oriented in the lying phase.

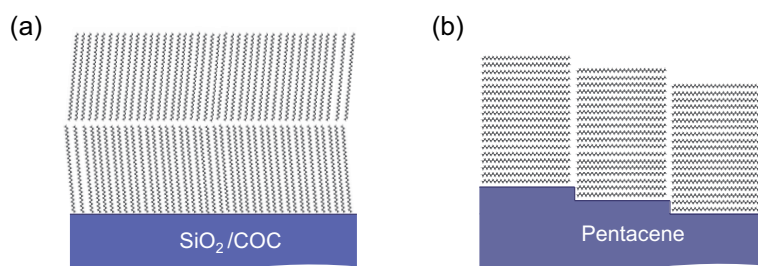


Figure 4.13: Idealized sketch of (a) the standing phase of TTC on $\text{SiO}_2 / \text{COC}$ and (b) the lying phase of TTC on $\text{SiO}_2 / \text{COC} / \text{P}$.

Finally, also the Au substrates modified by 1-octanethiol SAMs were investigated by x-ray reflectometry measurements. As the high substrate temperature turned out as unsuitable for the growth of a dense TTC layer, only the TTC layers with different deposition rates were analyzed. For the *Au/SAM* substrates, the (110) peak of the lying TTC phase (see Fig. 4.14 a) and an additional peak at 2.31 \AA^{-1} (blue circle), originating from another TTC phase, appears. Also for the *Au/SAM/P* substrate this peak can be observed (see Fig. 4.14 b), besides two peaks at 1.99 \AA^{-1} and 2.03 \AA^{-1} (green circle). These peaks may be associated with a pentacene bulk phase or a further TTC phase.

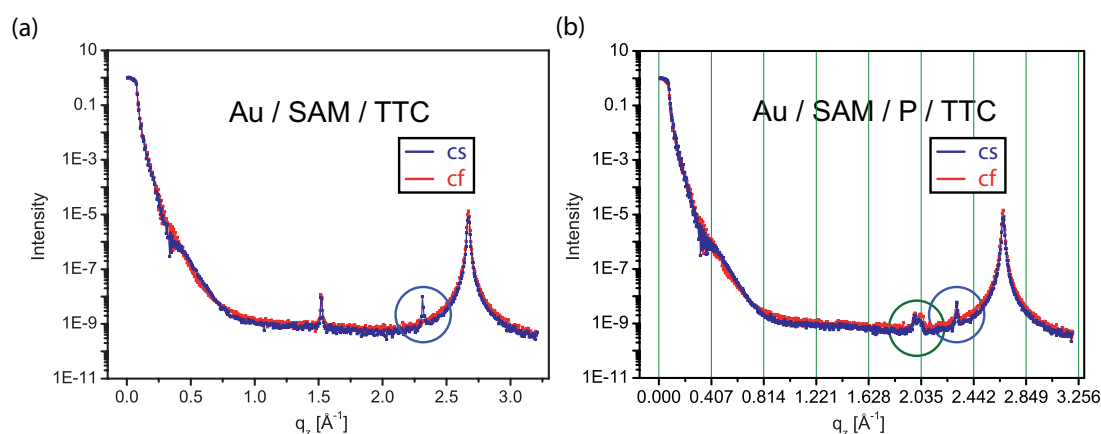


Figure 4.14: X-ray Reflectometry Measurements of a TTC thin film on (a) a Au substrate modified by a SAM and (b) on a stack consisting of a Au substrate modified by a SAM and a 50 nm thick pentacene film.

Current-Voltage Measurements

The most crucial aspect of a capping layer for sensing devices is to prevent charge transfer. In order to investigate the correlation between the morphology of the TTC film and the insulating quality, we designed a microfluidic chamber made of PDMS which allows for the introduction of electrodes, see Fig. 4.15. The chamber can be pressed on top of a chip manually via a micrometer-differential-adjuster, while the pressure is measured by a piezo-electric pressure-sensor. For the measurement of the leakage currents Au-pads ($4 \times 4 \text{ mm}$) were deposited via e-beam evaporation on top of thermally oxidized silicon wafers and were capped subsequently by molecular beam epitaxy with pentacene and TTC, as described above.

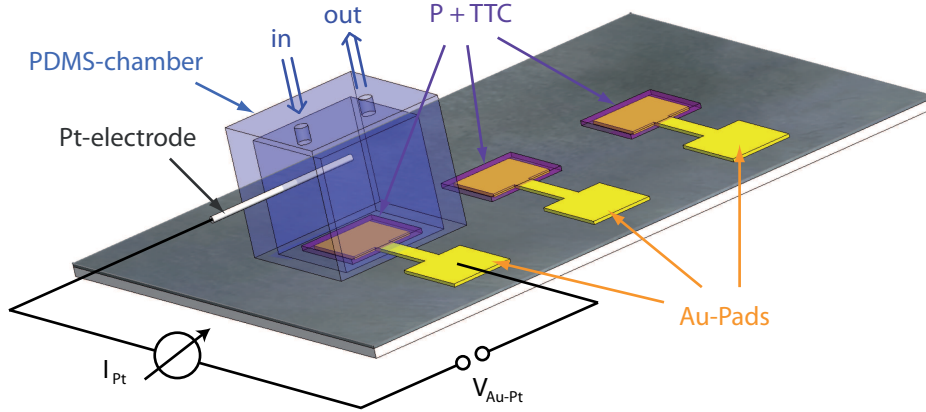


Figure 4.15: Schematic of the setup for leakage current measurements.

After carefully filling the microfluidic chamber with a 1 mM sodiumchloride (NaCl) solution, the leakage currents across the pentacene-TTC stack were measured by applying a voltage V_{Au-Pt} between the Au-pad and a platinum electrode (see Fig. 4.15) and measuring the current I_{Pt} with a Keithley 2612 Sourcemeter. The contact area to the electrolyte was 0.06 cm^2 . The resulting current-voltage curves are presented in Fig. 4.16.

As expected the TTC layer deposited at a low substrate temperature (Fig. 4.16 a and c), show much better sealing properties than the TTC layer deposited at a high substrate temperature (Fig. 4.16 b and d). The different magnitude of the noise in Fig. 4.16 a and c originates from a different current range chosen for the sourcemeter. Note that this measurement basically corresponds to a voltammetry experiment and therefore the peaks in Fig. 4.16 b and d results from the reduction and oxidation of pentacene. The electrochemical processes at electrolyte / pentacene interfaces are discussed in detail in section 5.3.

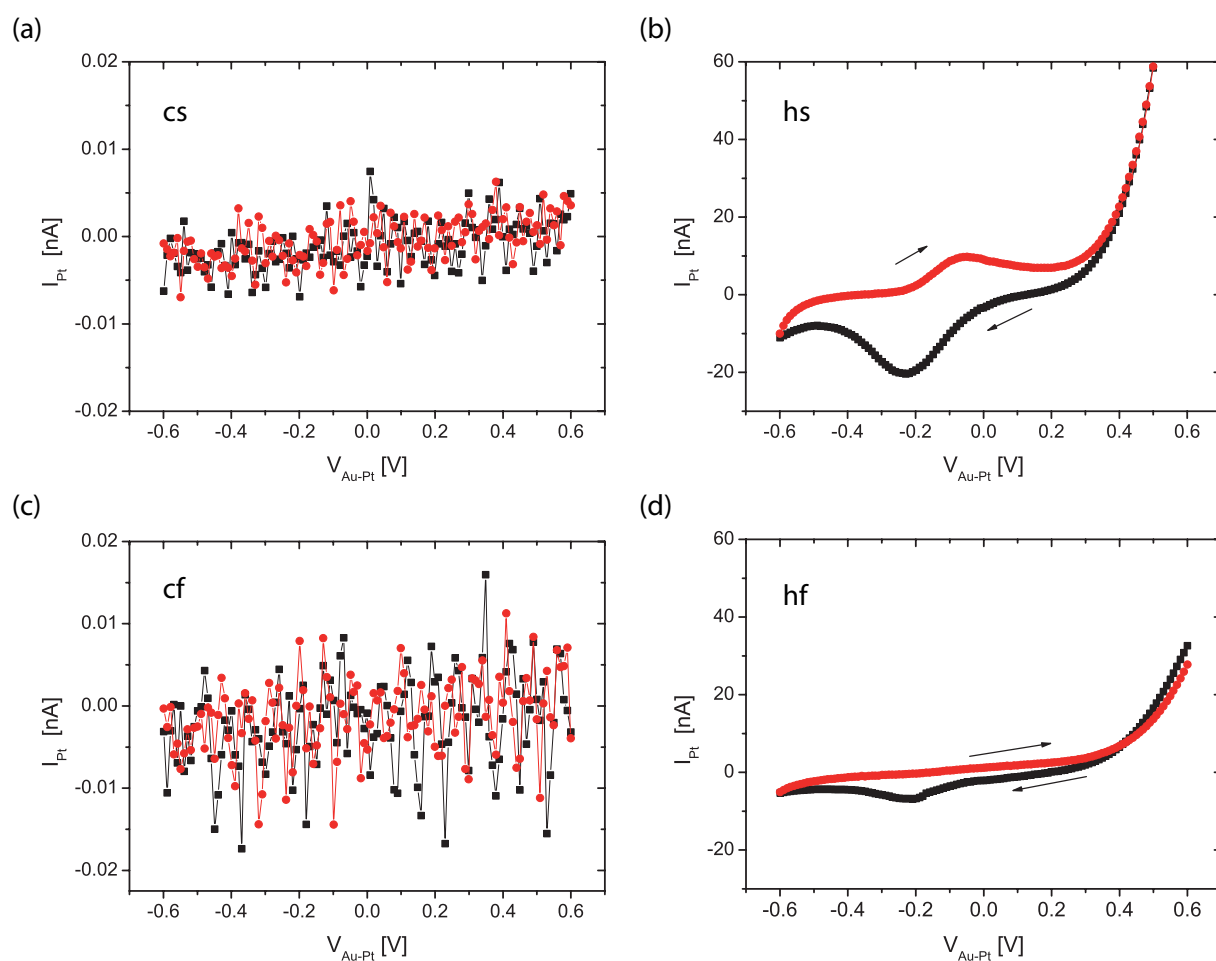


Figure 4.16: Leakage Current Measurements for Pentacene capped by TTC. The TTC was either deposited (a) with a low rate and low substrate temperature (cs), or (b) with a low rate and high substrate temperature (hs), or (c) with a high rate and low substrate temperature (cf), or (d) with a high rate and high substrate temperature (hf).

Contact Angle Measurements

As the penetration of water molecules in the pentacene layer either results in the formation of defects (see section 4.1) or changes the electric field at the pentacene / insulator interface, due to its dipole character it is desirable to use a hydrophobic capping layer for pentacene. Therefore, we measured the hydrophobicity of TTC films evaporated on $SiO_2/COC/P$ substrates prepared as described above. For this purpose we used a setup, consisting of a positioning table to adjust the position of the sample, an optical microscope and a mirror, allowing to measure the contact angle of a small water drop on the surface of the sample (see Fig. 4.17 a). By this method photographs of the water drops (see Fig. 4.17 b) on selected substrates (compare section 4.2.2) were made and analyzed by a graphics editing program.

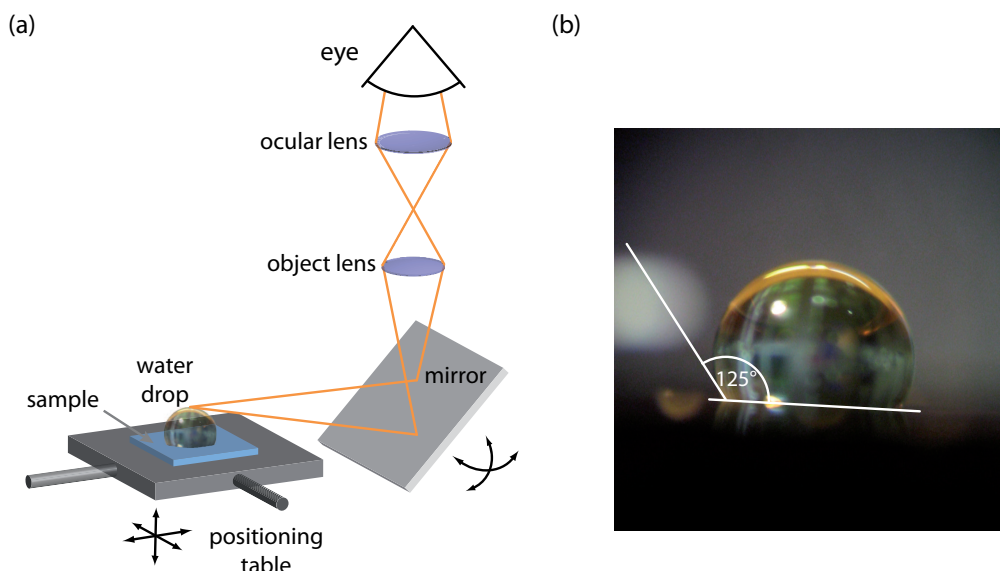


Figure 4.17: (a) Simplified illustration of the setup for the contact angle measurement of a water drop on a TTC surface (b) Photograph of a water drop on a 50 nm TTC film evaporated with a deposition rate of 4 Å/s and a substrate temperature of 300 K on top of a $SiO_2/COC/P$ substrate.

It turns out that the substrates evaporated at a low substrate temperature are more hydrophobic than those deposited at high substrate temperatures. The most hydrophobic TTC surface was achieved for a high deposition rate. The measured contact angles are presented in the following table:

surface	cs	hs	cf	hf
$Au/P/TTC$	111°	101°	125°	99°
Au/TTC	-	-	111°	-
$SiO_2/COC/P/TTC$	-	-	115°	-

4.3 Characterization of the Dielectric Layer

One of the main issues for realizing a sensor device based on OTFTs was the change of the electrical properties of the dielectric layer SiO_2 under the influence of ionic solutions. As the operation in ionic solutions restricts the magnitude of the drain-voltages to very low values, the resulting drain currents are generally very low. Therefore, already very small leakage currents would destroy the OTFT performance. Besides the high demands on the insulating properties of the SiO_2 layer, also the influence of trap-states on the threshold voltage and the hysteresis (see section 2.2.3) plays a crucial role. Additionally, it turned out that especially the penetration of sodium ions (Na^+) change the capacitance of the SiO_2 layer or even cause high leakage currents to the gate electrode. On the one hand, this observation is astonishing as Na^+ is a small ion, causing a high electric field and therefore have a very high hydration energy of 440 kJ/mol [90]. On the other hand the small size of Na^+ allows for a more easy penetration into the SiO_2 lattice. We confirmed the penetration of Na^+ ions into SiO_2 by sweeping a voltage V_{Si} between a Pt-electrode, introduced in a 1 mM NaCl solution, and the highly doped Si layer of a wafer oxidized with 300 nm dry oxide (Active Business Company GmbH) and measured the current I_{Si} across the SiO_2 layer (see inset Fig. 4.18). The measurement was performed with a Keithley 2612 Sourcemeter. The contact area to the NaCl solution was 0.04 cm^2 and the Pt-electrode was set to ground potential.

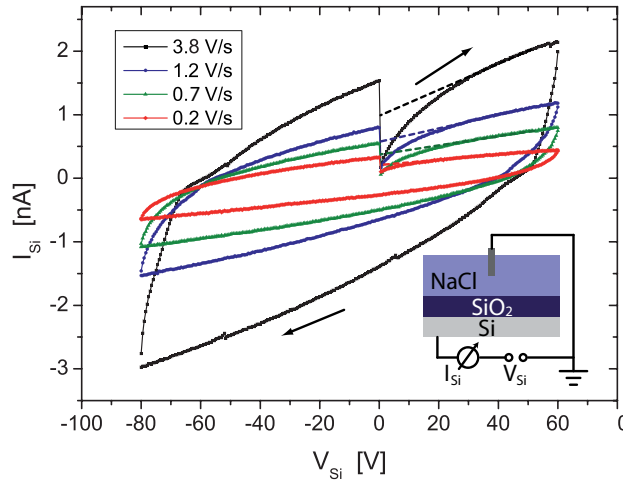


Figure 4.18: Sweep of the voltage across the SiO_2 layer and measurement of the corresponding current for different sweep velocities. The shift at $V_{Si} = 0 \text{ V}$ origins from the penetration of sodium ions into SiO_2 .

When a negative voltage is applied the Na^+ ions are pulled into the SiO_2 layer and increase the permittivity and therefore the capacitance of the SiO_2 layer. The increased current at $V_{Si} = 0 \text{ V}$ after one complete cycle in Fig. 4.18 confirms this assumption. It is easy to see that this change in current ΔI depends on the sweep velocity v_s by the simple relation $\Delta I = v_s \Delta C$. We proofed this linear dependency by performing the sweep

at different sweep velocities. It turned out that the increase of the current is not directly proportional to the sweep velocity, what can be explained by the shorter time the Na^+ ions have to penetrate in the SiO_2 layer for higher sweep velocities and by the influence of leakage currents. Note that the sourcemeter can only apply potential steps and that after every potential step the current originating from redox reactions decreases with the square root of time (see Fig. 3.13 b), while the charging current of the capacitor decreases exponentially. Therefore, in order to estimate the change in the capacitance we choose a very low sweep velocity (0.2 V/s) and obtain a change in the capacitance of $\delta C = 4.1 \text{ nF cm}^{-2}$, what is quite high compared to the total capacitance of SiO_2 (about 11.5 nF cm^{-2}). Due to the simplifications mentioned above the estimated value for the change in capacitance is probably too high. However, the measurement proves that the penetration of Na^+ ions occurs and has an impact on the capacitance of SiO_2 .

We also observed that it is possible to regain the initial state, i.e. pushing the Na^+ ions out of the SiO_2 layer, by applying a very positive voltage. A more serious problem than the change in the capacitance is the drastic decrease of the breakdown voltage.

Besides the substrates with $300 \text{ nm } SiO_2$ dielectric layers, we also used substrates with a stack consisting of $100 \text{ nm } SiO_2$ and $100 \text{ nm } Si_3N_4$, as they have a very positive effect on the performance of our pentacene TFTs. However, this double dielectric layer shows higher leakage currents to the gate. We also observed that a thin COC layer can additionally prevent the penetration of Na^+ ions (see Fig. 4.19). Again, one can see a shift of the current due to the penetration of Na^+ ions. The irregular shape of the curve may be explained by the influence of the SiO_2/Si_3N_4 interface. A similar effect of the COC layer on the current was observed for SiO_2 dielectrics. However, here the current shows a much more abrupt increase at a certain voltage.

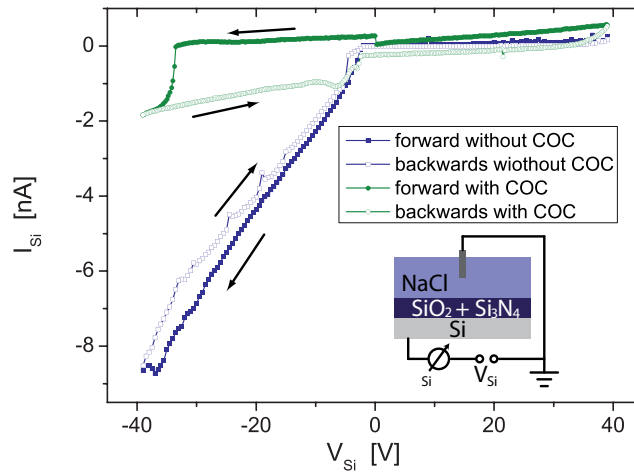


Figure 4.19: Sweep of the voltage across the SiO_2 / Si_3N_4 layer and measurement of the corresponding current. The leakage currents across the dielectric layer can be significantly reduced by spin coating a thin COC layer on top.

Chapter 5

Electrochemical Characterization of Organic Semiconductor Interfaces

In this chapter the basic electrochemical experiments are described we used to characterize the interfaces which are from decisive importance for the realization of a sensing device based on TTC capped pentacene TFTs.

5.1 Setup

For the electrochemical characterization an electrochemical cell made of polytetrafluorethylen (PTFE) was fabricated, see Fig. 5.1 a. The basic principle is that a chip can be placed on a socket and electrically contacted from above by spring contacts (see Fig. 5.1 b). For this purpose usually the whole chip was covered by a thin Au-layer by e-beam deposition, which acted as the working electrode. Depending on the demands of the electrochemical experiment a small area in the center of the chip was covered by the organic material of interest. Next, the chip was sealed by a thin PDMS mat to prevent currents from the electrolyte to the bare Au region. After closing the setup by pressing the electrochemical cell on top of the socket and the sealed substrate, the working electrode can be connected to a potentiostat (Ivium Compactstat) by the electric connectors of the spring contacts. The electrochemical cell allows for the introduction of several electrodes, e.g. counter- and reference electrode. In order to suppress noise in the current measurements caused by electromagnetic fields, we fabricated a shielding box made of aluminum, see Fig. 5.2. The box has two compartments, one for the potentiostat and one for the electrochemical cell, which are separated by an aluminum plate which shields the electrochemical cell from the electromagnetic field of the potentiostat. The cables to the electrodes of the cell are guided via BNC-feedthroughs from one compartment to to the other. A stand was used to introduce reference-electrodes with a high diameter in the electrolyte from the top. For more complex measurements, e.g. the characterization of the influence of the electrolyte potential on TFT performance, additional feedthroughs allow to apply external voltages. The whole box was grounded externally and connected to the chassis of the potentiostat

by the intended plug (green).

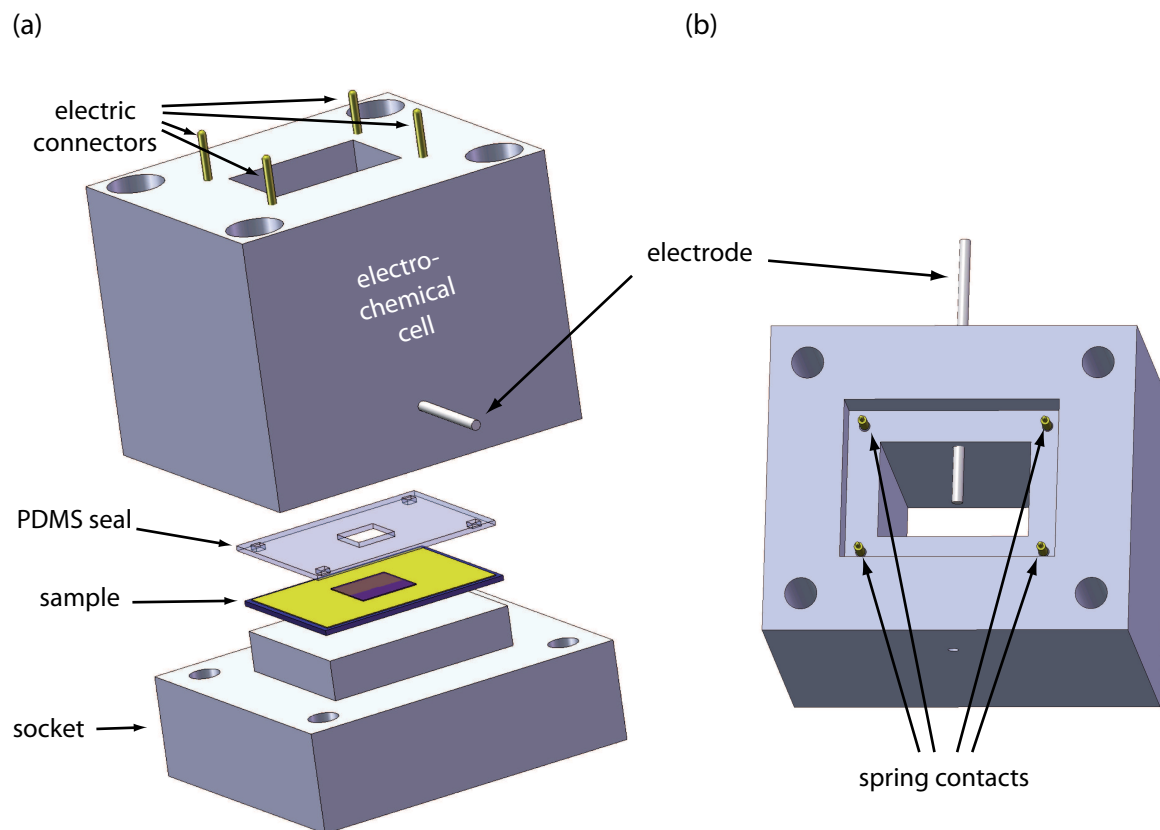


Figure 5.1: Design drawing of the self-made electrochemical cell: (a) Components of the complete setup. (b) View of the inner build-up of the electrochemical cell.

5.2 Transient Measurements

First we tried to get a rough idea of the dynamics occurring at the interface to the electrolyte by performing transient measurements, i.e. applying subsequently potential steps (compare section 3.2.3). For this purpose we used the electrochemical cell described above with a leak free Ag/AgCl reference electrode and a Pt counter electrode. As electrolyte we used a 1 mM NaCl solution. The contact area of the working electrode, i.e. the organic thin film, was 0.04 cm^2 . In order to achieve an equilibrium state of the system we set the potential at 0 V for 60 s before the measurements started. The results for Au/P (50 nm P), Au/TTC (50 nm TTC) and Au/P/TTC (50 nm P and 50 nm TTC) thin films are presented in Fig. 5.3 a-c, respectively. The TTC thin films were evaporated at a substrate temperature of 300 K and a deposition rate of 4.0 Å/s .

According to section 3.2.3 one should expect that the current I_{WE} decays proportional to $t^{-1/2}$. However, as shown in Fig. 5.3 d it is not possible to fit the data (red squares) with

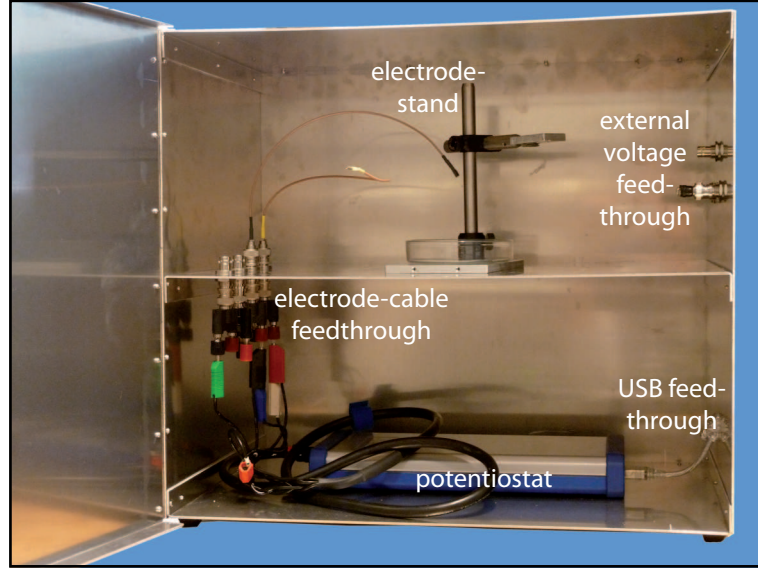


Figure 5.2: Photograph of the self-made shielding box for electrochemical measurements.

the function $I_{WE} = A \cdot t^{-1/2} + I_{\Omega}$ (blue curve), where A is a constant and I_{Ω} is the current offset caused by the ohmic drop. The reason is that the charging currents, which decay exponentially, can not be neglected. However, it is not possible to explain the data by charging currents alone (black curve). In contrast, if one assumes that the total current is composed by the sum of the faradaic current, the charging current and the ohmic drop, one obtains an excellent fit of the data (green curve). Using the function

$$I_{WE} = A_1 \cdot \exp\left(-\frac{t}{\tau}\right) + A_2 \cdot t^{-1/2} + I_{\Omega} \quad (5.1)$$

to fit the data in Fig. 5.3 a-c one obtains the following values for the fitting parameters A_1 , τ , A_2 and I_{Ω} :

V_{WE} [V]	A_1 [nA]	τ [s]	A_2 [nA \cdot s ^{1/2}]	I_{Ω} [nA]	χ^2/DoF	$[X]\sqrt{D} \cdot 10^{-12}$	$[O_2]$ [μM]
-0.2	34.87	0.16	15.13	3.56	0.01	6.95	1.57
0.0	36.76	0.22	10.81	-2.49	0.04	4.96	1.12
0.2	56.47	0.21	24.57	-3.10	0.07	11.28	2.54
0.0	41.28	0.22	10.60	-1.14	0.04	4.87	1.10
-0.2	36.59	0.16	18.67	3.13	0.01	8.57	1.93

for Au/P ,

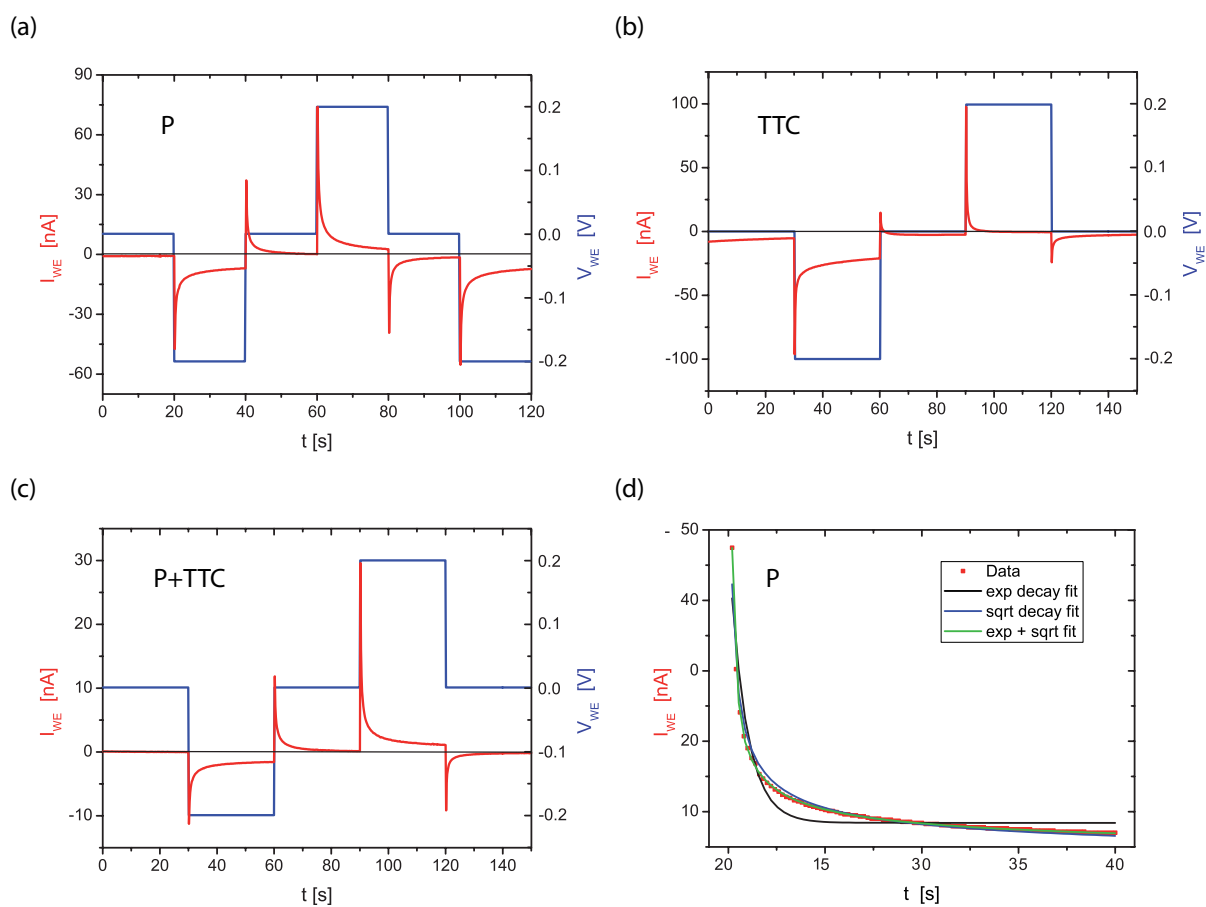


Figure 5.3: Transient measurements of (a) Au/P , (b) Au/TTC and (c) $Au/P/TTC$ thin films. (d) Exemplary fits of the current obtained for the potential step of -0.2 V in Fig. (a).

V_{WE} [V]	A_1 [nA]	τ [s]	A_2 [nA \cdot s ^{1/2}]	I_Ω [nA]	χ^2/DoF	$[X]\sqrt{D} \cdot 10^{-12}$	$[O_2]$ [μ M]
-0.2	124.10	0.12	23.82	18.49	0.218	10.94	2.46
0.0	16.84	0.28	4.54	-3.88	0.219	2.09	0.47
0.2	197.09	0.21	10.19	-2.77	0.747	4.68	1.05
0.0	21.79	0.14	7.96	1.15	0.001	3.66	0.82

for Au/TTC and

V_{WE} [V]	A_1 [nA]	τ [s]	A_2 [nA \cdot s ^{1/2}]	I_Ω [nA]	χ^2/DoF	$[X]\sqrt{D} \cdot 10^{-12}$	$[O_2]$ [μ M]
-0.2	2.69	0.20	4.26	0.72	0.001	1.96	0.44
0.0	5.82	0.28	4.35	-0.83	0.005	2.00	0.23
0.2	32.20	0.20	8.10	-0.57	0.017	3.72	0.84
0.0	10.39	0.22	2.37	-0.37	0.029	1.09	0.25

for $Au/P/TTC$.

In the tables also the χ^2 -values per degree of freedom (indicating the goodness of the fit) are presented, as well as the product of the bulk concentration of the reductant or the oxidant and the square root of the diffusion constant $[X]\sqrt{D}$ (in units of [$mol \cdot 10^{-3} cm^{-2} s^{-1/2}$]) calculated by the Cottrell equation Eq. 3.37 for a one electron reaction. Additionally, the value of the concentration for oxygen $[O_2]$ is calculated, assuming that oxygen is involved in the redox reaction ($D(O_2) = 1.97 \cdot 10^{-5} cm^2 s^{-1}$ [91]). The latter statement is underpinned by voltammetry measurements, see section 5.3. Note that the Na^+ or Cl^- does not contribute to the faradaic current as the standard electrode potential V_0 (see Eq. 3.8) is much higher than the applied voltages. The differences in the values of $[X]\sqrt{D}$ indicates that the oxidants have other diffusion constants than the reductants.

For the pentacene thin film (Fig. 5.3 a) it is probable that one or more defects of pentacene (see section 4.1.1) involving oxygen, hydroxide or hydronium participate. The change of $[X]\sqrt{D}$ for the initial reduction step from 0 V to -0.2 V and the same step in the end is probably caused by a non reversible electrode reaction in one of the foregoing steps. For the Au/TTC film (Fig. 5.3 b) apparently a very slow process is involved, causing that the current does not reach an equilibrium state in the span of time of 30 s. A look on the table reveals that the diffusion of the reductant must be responsible for this behavior. As the TTC layer is chemically inert the electrode reaction must occur at the Au/TTC interface. Hence, it seems that the penetration of the reductant in the TTC layer is much slower than the penetration of the oxidant. For the $Au/P/TTC$ film the values of $[X]\sqrt{D}$ are much lower than for the other films, what confirms that TTC is chemically inert and significantly slow down the penetration of reactants. By changing the concentration of oxygen or the pH value it may be possible to determine which reactants are involved. The origin of the

faradaic currents will be further discussed in section 5.3.

As the second term in Eq. 5.1 describes the discharging of a capacitor the fit parameter τ can be set equal to RC , where R is the resistance and C is the capacitance of the system. Interestingly, RC differs for the Au/P film at $V_{WE} = -0.2\text{ V}$ and the other voltages. This effect may result from a change of the resistivity of the pentacene layer due to the electric field. The changes of RC of the other samples may be caused by the change of the resistance of the TTC film due to the penetration of charged particles. The capacitance and resistance of the organic thin films can be investigated more precisely by impedance spectroscopy and will be treated in section 5.4. In conclusion the transient measurements indicate that it is possible to minimize the faradaic currents at all samples by a low oxygen concentration.

5.3 Cyclic Voltammetry Measurements

Cyclic voltammetry is often called the 'spectroscopy of the electrochemist' because it can be regarded as a kind of finger-print of the electrochemical characteristics of a redox system. [92] As described in section 3.2.4 the shape, the position and the maximum current of the occurring peaks contain information about the redox potentials, the kinetics of electrode reactions or the adsorption of molecules. However, in practice often the high number of unknown parameters, multi-electron transfer reactions and the appearance of non-reversible reactions impede quantitative predictions. For example the electrochemistry of gold in aqueous solution shows an extremely complex behavior [93,94] and strongly depends on the pH value of the solution [95,96]. Nevertheless, due to its high relevance as contact material for organic semiconductors, especially pentacene, we used 50 nm thin Au layers, evaporated on dry oxidized silicon wafers, as starting substrate for all voltammetry measurements.

5.3.1 Experimental

The voltammetry measurements were performed with the setup presented in section 5.1 including a leak free Ag/AgCl reference electrode and a Pt counter electrode. Some of the measurements were also performed with a two-electrode setup, i.e. without the Ag/AgCl-reference electrode. The contact area to the electrolyte was 0.04 cm^2 .

As expected the voltammetry curves (sweep velocity 50 mV/s) of a bare Au film in a 1 mM aqueous NaCl solution shows a very complex behavior and exhibit at least five different redox reactions (marked by the numbers 1-5, see Fig. 5.4 a). Note that, except from redox reaction 2, all reduction peak magnitudes are lower than the oxidation peaks, indicating several non-fully reversible oxidation reactions at the Au interface. The latter conclusion is also the reason for the deviation of the peak separations from the value for a nernstian redox reaction (57 mV , see Eq. 3.40). The cyclic voltammetry measurement of bare Au serve as a kind of reference measurement for the voltammetry measurements of the organic

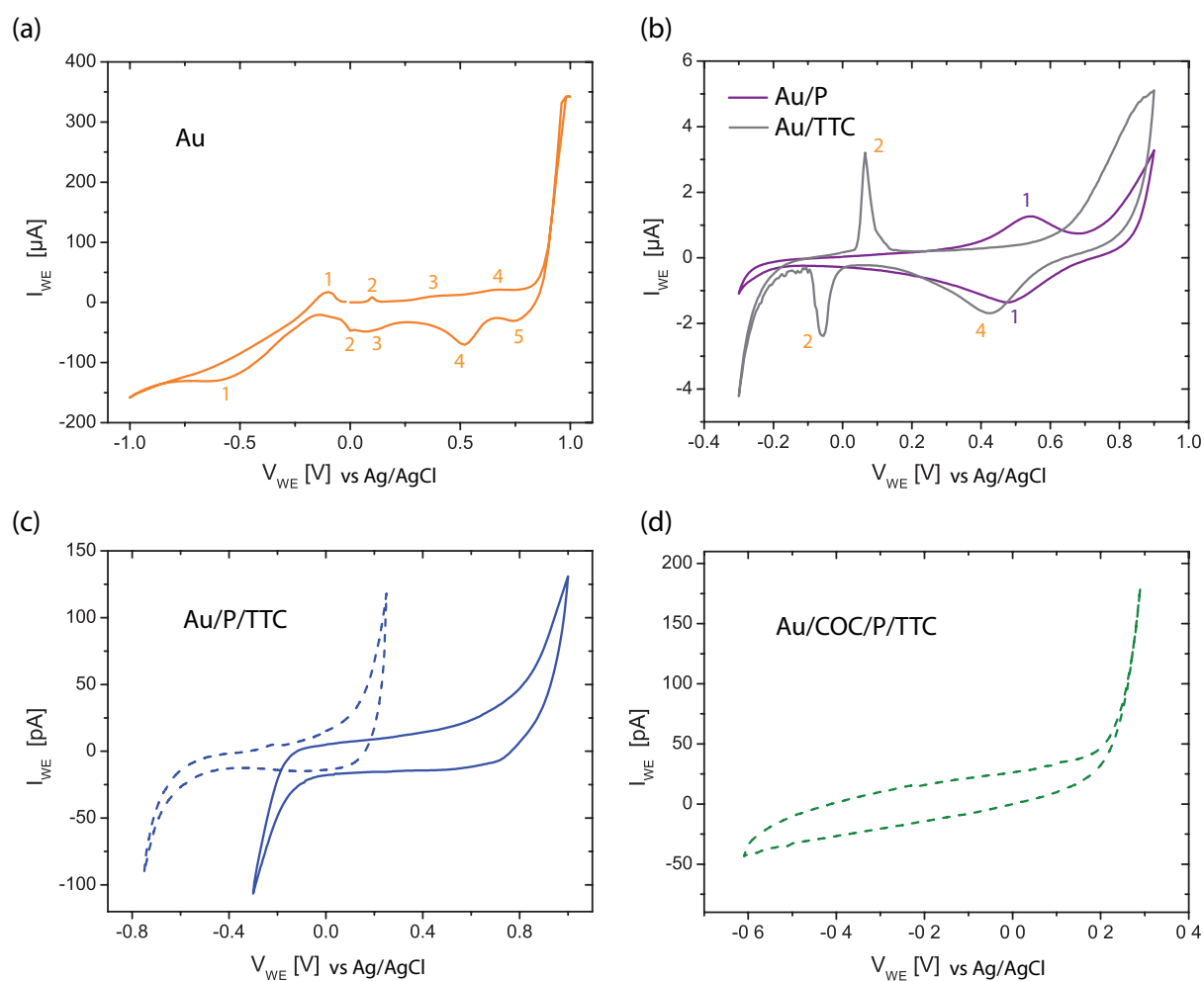


Figure 5.4: Cyclic Voltammetry Measurements of (a) a bare *Au* surface, (b) of *P* and *TTC* thin films on *Au* substrates, (c) of a *P/TTC* stack on a *Au* substrate and (d) of a *COC/P/TTC* stack on a *Au* substrate. The solid curves were recorded with a Ag/AgCl electrode and the dashed curves with a Pt-electrode.

films, i.e. which peaks origins from the surface of the organic material and which from the Au interface.

The cyclic voltammetry measurement of a 50 nm pentacene thin film (sweep velocity 10 mV/s) reveals that the pentacene layer prevents the penetration of reactants to the Au interface and therefore drastically reduces the current (see purple curve in Fig. 5.4 b). Apparently, only one nearly fully reversible redox reaction (the voltage separation is 65 mV) occurs within the applied voltage window. This reaction may either involve one of the defect states discussed in section 4.1.1 or an electron transfer to the valence or conduction band of pentacene as described in section 3.1.4. Using the half-wave potential ($V_{1/2} = 0.51V$) and regarding that the voltage is defined relative to the potential of the SHE electrode (Eq. 3.10) and that the electrode potential of the Ag/AgCl electrode used in this experiment is 0.21V relative to the SHE electrode, it is possible to estimate the energy level which is involved in the charge transfer by $E_{ct} = -4.44 eV - (0.51 + 0.21) eV = -5.16 eV$. This value is quite close to the valence band of pentacene and therefore it is not clear if there is a charge transfer to the valence band or if a defect state near the valence band edge is responsible for the redox reaction observed in Fig. 5.4 b. In contrast, the cyclic voltammetry measurement of a 50 nm thin TTC film on Au (sweep velocity 10 mV/s, see gray curve in Fig. 5.4 b) shows no redox reaction of the TTC film, as all peaks can be assigned to the Au interface (see Fig. 5.4 a). Note that the position of the peaks have shifted due to the different sweep velocity. The measurement confirms the inert nature of TTC which was already demonstrated by the transient measurements (see section 5.2). Also in this case the current is significantly reduced compared to the bare Au surface. This surface is relevant for the contact region of a top contact OTFT capped by TTC.

For a stack of a 50 nm pentacene film and a 50 nm TTC film on a Au substrate the currents of the voltammetry measurement (10 mV/s, Fig. 5.4 c) are suppressed by a factor 10^6 compared to a bare Au surface. This surface corresponds to the contact region of a bottom contact OTFT capped by TTC. The currents in the voltammetry measurement for the stack which is relevant for the channel region, i.e. a thin COC layer with 50 nm pentacene film and a 50 nm TTC film on top, are in the same range. Note that the curves recorded with a two electrode setup (dashed curves) allow for another voltage window than the curves recorded with a three electrode setup.

In conclusion one can say that a 50 nm TTC layer on top can efficiently prevent an interaction of the electrolyte with Au or pentacene. Here, the TTC layer grown on pentacene seems to have better sealing properties than a TTC layer directly grown on Au.

5.3.2 Discussion

The pentacene/electrolyte interface is from general interest, because the considerations made for this interface allows for an optimization of sensing devices based on pentacene or other organic semiconductors. A semiconductor is inert if no redox reaction occurs within the applied voltage range, e.g. there is no overlap of the Gaussian distribution of the redox states (see Fig. 3.7) with the valence or conduction band or a surface state. In order to determine the voltage window available for a certain setup it is important to realize at

which electrode the limiting reactions take place. The conversion of the voltage at the working electrode V_{WE} in respect to a Ag/AgCl electrode, a normal hydrogen (NHE) and vacuum is illustrated in Fig. 5.5 a. In the two electrode setup $V_{Pt} = -V_{WE}$, while in the three electrode setup $V_{Ag/AgCl} = -V_{WE}$ and V_{Pt} is shifted by 0.21 V in respect to the Ag/AgCl electrode. In the present case the limiting reactions seem to be $2H^+ + 2e^- \rightleftharpoons H_2$ and $O_2 + 2H_2O + 4e^- \rightleftharpoons 4OH^-$ (dominating in basic conditions) or $O_2 + 4H^+ + 4e^- \rightleftharpoons 2H_2O$ (dominating in acidic conditions). As shown in Fig. 5.5 b the available voltage window (green double arrow) in aqueous solutions is largely situated in the band-gap of pentacene. The reversible redox reaction observed in Fig. 5.4 b at 0.51 V, what corresponds to -5.16 eV (see red mark in Fig. 5.5 b), is probably a charge transfer to the valence band. When the working electrode voltage is swept towards positive voltages, there is an electron transfer from the valence band to the reduced states causing an upward bending of the bands and an accumulation of holes at the semiconductor interface until all available electron states at the interface are empty.

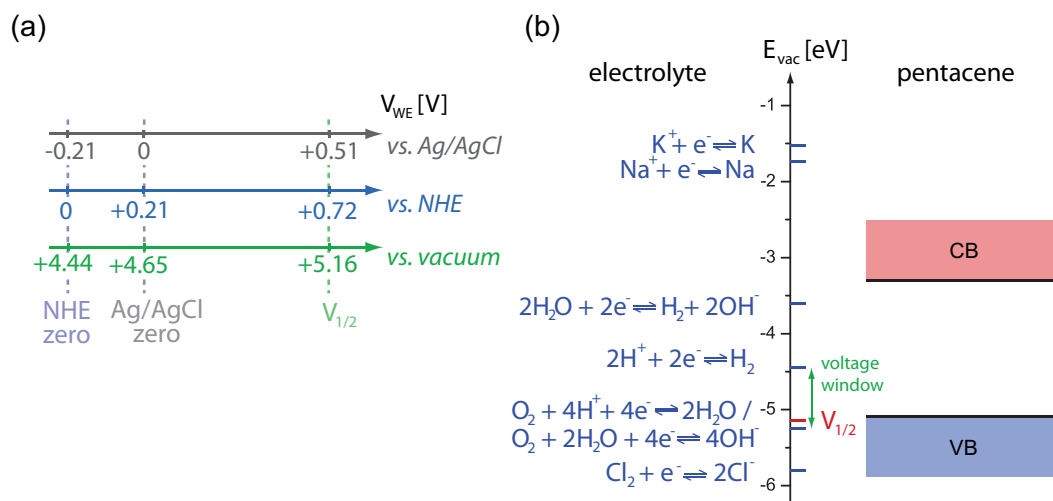


Figure 5.5: (a) The potential axes of the working electrode voltage V_{WE} of an Ag/AgCl-electrode, a normal hydrogen electrode (NHE) and vacuum. (b) Location of pentacene band structure relative to the redox potentials of all relevant redox reactions. The voltage window for an Ag/AgCl-electrode is illustrated by a green double arrow and the half-wave potential $V_{1/2}$ for the redox reaction observed for pentacene is marked red.

Another possibility is that there is a charge transfer to surface states or that the redox reaction mentioned above is coupled to the formation of $(C - H_2)$ -defects (see section 4.1.1). In this case the electrons cross the interface until a dihydropentacene passivation layer prevents a further formation of $(C - H_2)$ -defects. Opposite to the charge transfer to the valence band, the conductivity of pentacene decreases with the formation of dihydropentacene. In agreement to this we observed a decrease of the drain current of insufficiently capped pentacene TFTs in aqueous solutions. According to Northrup et al. the $(C - H_2)$ -defect occurs at 0.34 eV above the valence band edge [79]. However, due to surface states it is probable that the bands are bended upwards at the interface, allowing for the formation

of dihydropentacene. The redox reaction involving the pentacenehydroquinone ($C_{22}H_{14}O$) defect is unlikely as a pH value of 8.4 would be necessary to drive the redox reaction $O_2 + 4H_2O + 4e^- \rightleftharpoons 4OH$ at -5.16 eV (calculated according to [97]). From the redox reactions marked in Fig. 5.5 b it is apparent that also the formation of pentacenequinone or the reactions involving sodium or chloride can be excluded.

5.4 Impedance Measurements

As the sensing mechanism of potentiometric sensor devices is based on capacitive coupling (see section 1.2.1), the determination of the capacitances of the involved organic layers are of special interest. The most suitable electrochemical tool for this intent is electrochemical impedance spectroscopy (see section 3.2.5). As it turned out that top contact pentacene TFTs show much higher mobilities as bottom-contact pentacene TFTs, what is from special importance for low operation voltages, we restrict our investigation on the impedance of the $Au/COC/P/TTC$ and the Au/TTC stack. Here, the thickness of the COC layer was 8 nm , the thickness of pentacene 20 nm and the thickness of TTC 50 nm . The impedance spectroscopy were performed with the setup discussed in section 5.1 with a two electrode configuration, i.e. the $Au/COC/P/TTC$ or the Au/TTC stack as working electrode and a Pt-electrode as counter electrode, in a 1 mM aqueous KCl solution. Here, we used no additional reference electrode, because the control of the potential by the leak free $Ag/AgCl$ electrode we used otherwise is too slow for impedance measurements at high frequencies in dilute solutions. The contact area to the electrolyte was 0.04 cm^2 , the DC voltage was set to 0 V and the AC amplitude to 10 mV . The resulting Bode Plot of the impedance is shown in Fig. 5.6 a.

According to section 3.2.5 a phase of -90° corresponds to a pure capacitive response. Therefore, the behavior is dominated by the capacitances over a wide range (about 1 Hz to 1 kHz) and thus also well suited for the detection of fast processes at the interface. For a quantitatively analysis we used an equivalent circuit, consisting of a lead resistance R_e and four RC units in series, to fit the data of Fig. 5.6 a. The resulting values for the resistances as defined in the upper scheme of Fig. 5.6 d, are $R_e = 1.2 \cdot 10^4\ \Omega$, $R_{TTC} = 8.7 \cdot 10^9\ \Omega$, $R_P = 1.4 \cdot 10^6\ \Omega$, $R_{COC} = 5.9 \cdot 10^7\ \Omega$, indicating good sealing properties. For the capacitances one obtains $C_{TTC} = 2.6 \cdot 10^{-8}\text{ Fcm}^{-2}$, $C_P = 1.8 \cdot 10^{-7}\text{ Fcm}^{-2}$, and $C_{COC} = 2.3 \cdot 10^{-7}\text{ Fcm}^{-2}$. The indices ' e ' corresponds to the electrolyte, ' TTC ' to the TTC thin film, ' P ' to the pentacene film and ' COC ' to the COC layer. For assigning the values to the different layers, we first made an impedance spectroscopy measurement of a COC layer on a Au substrate (see Fig. 5.6 b) and modeled the data by the equivalent circuit shown in Fig. 5.6 d. The fit yields $R_e = 1.1 \cdot 10^4\ \Omega$, $R_{COC} = 3.0 \cdot 10^8\ \Omega$ and $C_{COC} = 2.3 \cdot 10^{-7}\text{ Fcm}^{-2}$, in good agreement to the assignment for the COC layer chosen above. The value can also be confirmed by calculating the capacitance from the relative permittivity, which is specified by the supplier to $\epsilon_{COC} = 2.35$. The choice of the capacitance for the pentacene layer can be confirmed by assuming a reduced layer thickness of 15 nm , resulting from the high roughness of the

pentacene film and a relative permittivity of $\epsilon_P = 3.0$. As the capacitance of the electrical double layer is several magnitudes higher than the capacitances above, the remaining capacitance of $2.3 \cdot 10^{-7} \text{ Fcm}^{-2}$ can be assigned to the TTC layer. The corresponding resistance of $R_{TTC} = 8.7 \cdot 10^9 \Omega$ affirms the good sealing properties of TTC.

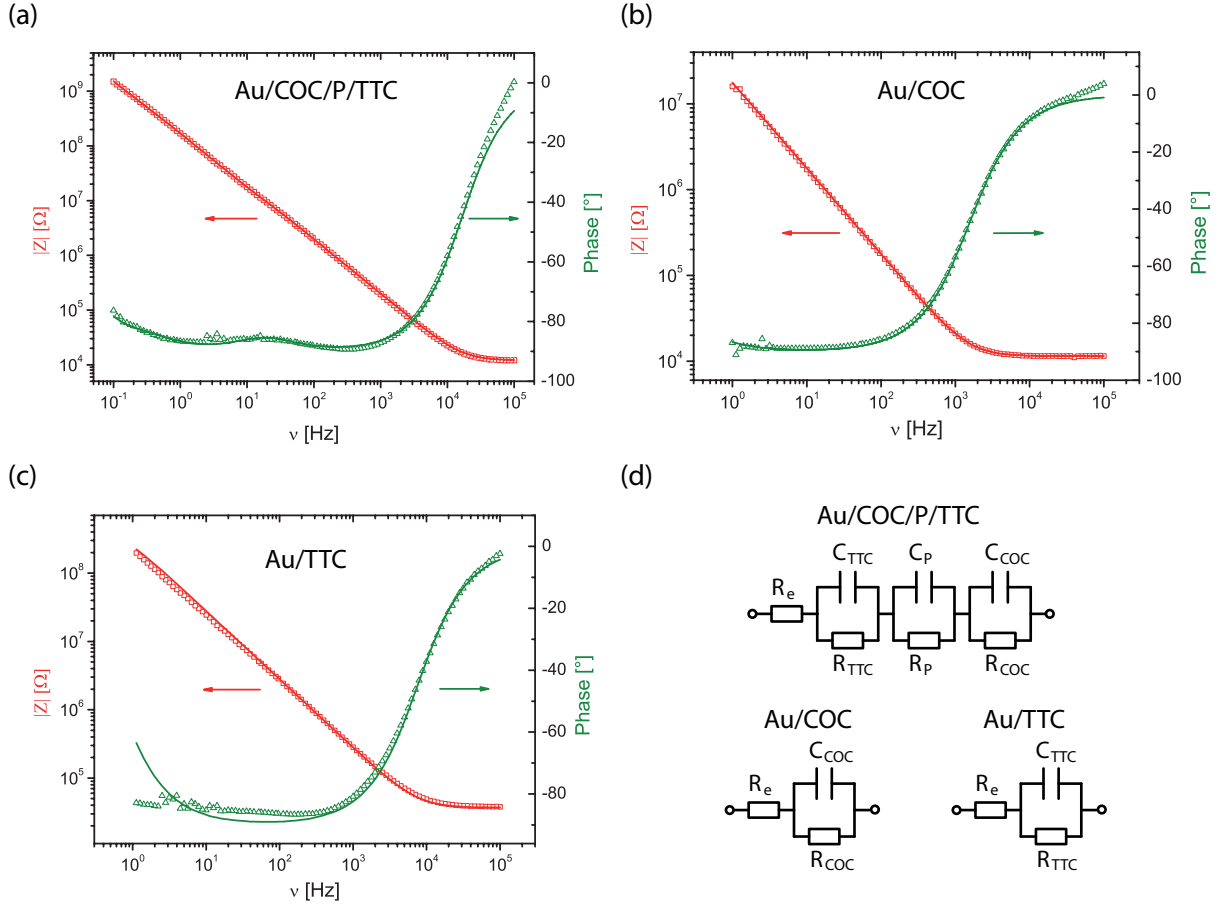


Figure 5.6: Impedance spectroscopy measurements of (a) a *COC/P/TTC* stack on a *Au* substrate (b) a *COC* thin film on a *Au* substrate, (c) of a *TTC* film on a *Au* substrate. The corresponding fits are drawn in as continuous lines.

In order to investigate the properties of the contact region, we additionally performed an impedance spectroscopy measurement of a single *TTC* layer on a *Au* substrate, see Fig. 5.6 c. Using the equivalent circuit in Fig. 5.6 d, one obtains $R_e = 3.7 \cdot 10^4 \Omega$, $R_{TTC} = 5.0 \cdot 10^8 \Omega$ and $C_{TTC} = 1.4 \cdot 10^{-7} \text{ Fcm}^{-2}$. The results confirm that the sealing properties of a *TTC* film grown on pentacene are much better than those of a *TTC* film grown on bare gold.

Chapter 6

Transducer Devices based on Double-Gate Thin Film Transistors

In this chapter a sensing device based on the principle of a DGTFT (see section 2.3) is presented. The basic idea is to use the electrolyte as top-gate and a TTC layer as top-gate dielectric. The adsorption of charged particles at the TTC interface change the effective top-gate field and therefore give rise to a change in the drain current of the DGTFT (Fig. 6.1). Here, one of the gate is used to set a working point, while the other gate is used to obtain the transfer characteristics of the DGTFT. From the shift of the transfer characteristic it is possible to determine the amount of adsorbed charges at the electrolyte/TTC interface.

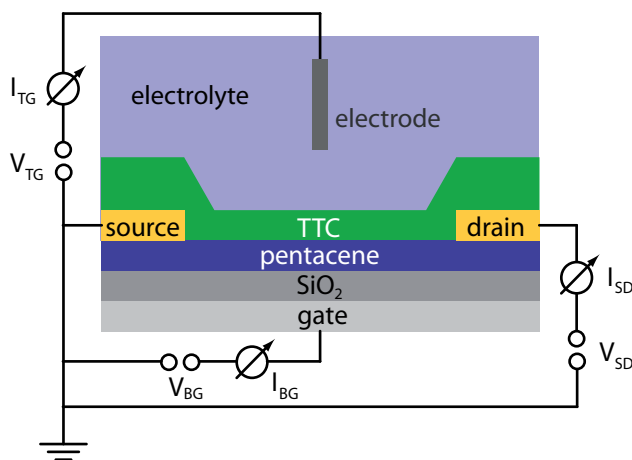


Figure 6.1: Basic principle of a DGTFT sensor device.

6.1 Sample Preparation

6.1.1 Substrates

The fabrication of DGTFT transducers has to meet many requirements. One of the most crucial issues is the quality of the bottom dielectric layer. It must assure small leakage currents to the gate, little influence on the threshold voltage, a low surface roughness and stable dielectric properties in aqueous ionic environment (see section 4.3). Although we tested several oxidized Si-wafers with different oxide layer thicknesses from different manufacturers, it was not possible to fulfill all the requirements mentioned above in a satisfactory manner. As also the oxide layers we fabricated ourself in a RTP furnace were not dense enough, we choose highly doped Si-wafers with the maximum available dry oxide thickness (300 nm, Active Business Company GmbH) and a capacitance of $1.15 \cdot 10^{-8} \text{ F/cm}^2$. The low surface roughness of dry oxidized wafers allows for a good growth of the pentacene thin film and the high thickness guarantee low leakage currents to the gate. On the other hand the voltage drop across the SiO_2 layer is quite high and it also turned out that the pentacene TFTs fabricated with these substrates show a very negative threshold voltage, what is undesirable for a low voltage operation.

To contact the highly doped silicon substrates ($15 \times 20 \text{ mm}$), which acted as the bottom-gate contact of the transistor, we first removed the oxide from the back side by etching with hydrogen fluoride. Here, it is very important to avoid any contact with the SiO_2 layer on the opposite side of the chip.

6.1.2 Cleaning Methods

Before the we proceeded with the fabrication of the DGTFTs, the substrate must be thoroughly cleaned in order to facilitate an ordered growth of pentacene. After sonicating the samples subsequently in deionized (DI) water, acetone, isopropanole and DI-water for 10 minutes, respectively, we either used RCA or piranha cleaning to remove organic matter. As the use of most tweezers would contaminate the cleaning solutions of both methods we used a self-made PTFE-holder which allows for the cleaning of ten samples at the same time, see Fig. 6.2 a. The RCA cleaning procedure includes the following steps:

- Base step: Samples are put in a 1 : 1 : 5 solution of H_2O_2 (30%) : NH_4OH (25%) : DI for 20 min
- Samples are sonicated in DI-water for 10 minutes
- Acid step: Samples are put in a 1 : 1 : 5 solution of H_2O_2 (30%) : HCl (37%) : DI for 20 min
- Samples are sonicated in DI-water for 10 minutes
- Repeat Base step

- Samples are sonicated in DI-water for 10 minutes, rinsed with DI water and dried with nitrogen

As the base steps cracks silicon-oxygen bonds at the surface and in the acid step OH groups are formed, the resulting surface is very hydrophilic.

The Piranha solution (peroxymonosulfuric acid, H_2SO_5) was made by a 3:1 mixture of sulfuric acid (H_2SO_4 , 98%) and hydrogen peroxide (H_2O_2 , 30%). The reaction is very exotherm so one has to mix the liquids very carefully. As a Piranha solution with a H_2O_2 concentration higher than 50% is explosive, it is important to add the peroxide to the acid and not vice versa. Also the presence of solvents may cause an explosion. Therefore we sonicated the samples several times in DI water before we put the samples in the piranha solution for 20 minutes. Like the RCA cleaning method the Piranha cleaning dissolve organic contaminants and hydroxylate the SiO_2 layer, resulting in an extremely hydrophilic surface.

Immediately before we started the fabrication of the DGTFTs we put the samples in an oxygen plasma for 3 minutes at a power of 50 W and a pressure of 2 torr. In order to fix shadow masks on the chips without damaging the surface, we used a self made sample holder, which allows for the use of different shadow masks for the evaporation of Au, P and TTC (Fig. 6.2 b).

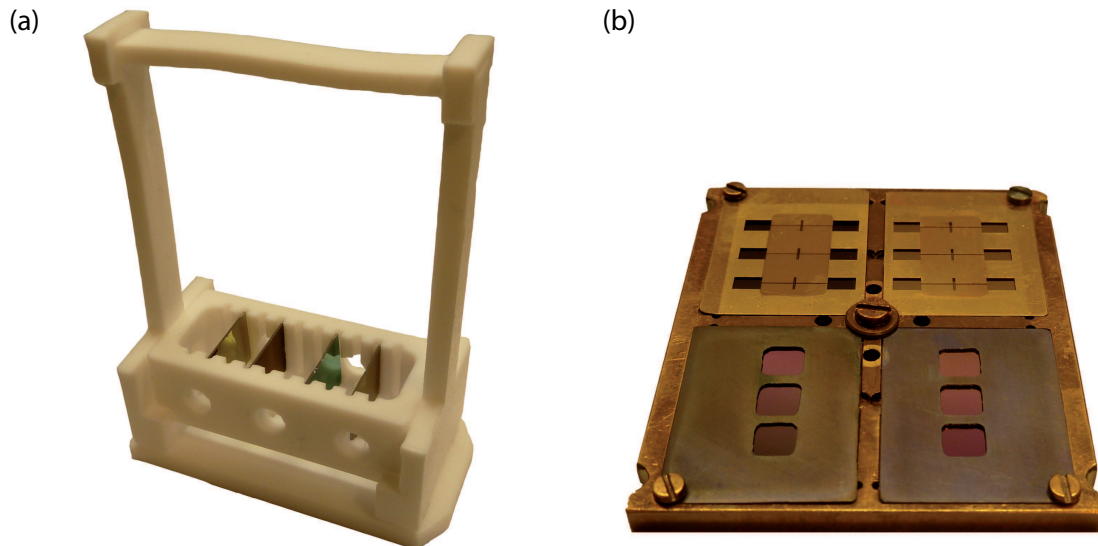


Figure 6.2: Photographs of the tools for the fabrication of DGTFTs: (a) PTFE sample-holder for the cleaning procedure and (b) sample holder for deposition of Au or organic materials via shadow-masks.

6.1.3 Fabrication of DGTFTs

As the cleaning procedure hydroxylate the SiO_2 surface, we spin coated a thin cyclic olefin copolymer (COC) layer dissolved with a mass concentration of 0.25% in toluene for 30 s

and with a rotation speed of 6000 *rpm* (see 6.3 a). The highly hydrophobic COC layer improved significantly the growth of pentacene and therefore the transistor performance. It also turned out that prior centrifugation of the COC solution has a positive effect on the quality of the COC layer. Although the TTC layer shows a better growth on pentacene than on Au, we made top contact DGTFTs as they showed much higher mobilities than bottom-contact DGTFTs. Moreover, this design allows for different thicknesses of the TTC layer on the contacts and on the channel region, as described later in this section. In the next step we evaporated pentacene (P) on the COC modified chips via shadow masks. In this way we prevented currents between the different DGTFTs on one chip (Fig. 6.3 b). On the one hand the film thickness should not be too low because the mobility [98] and the protection of the conducting channel from the influence of water or ions increases with the film thickness. On the other hand the film thickness should not be too high as the sensitivity decreases with the distance from the TTC film to the conducting channel of the TFT. Moreover, due to the increasing surface roughness the growth of TTC is less dense for thicker pentacene films. Therefore we tested pentacene film thicknesses of 20 *nm* and 50 *nm*. The deposition rate was 0.1 Å/s, the substrate temperature was about 30 °C and the pressure was about $5 \cdot 10^{-8}$ *mbar*.

After changing the shadow masks, 50 *nm* Au contacts were evaporated via e-beam deposition with a rate of 1 Å/s (Fig. 6.3 c). The areas of the contacts which are in contact to the electrolyte were reduced as much as possible. The resulting channel length was 50 μm and the channel width was 2000 μm . Next, without changing the shadow masks we deposited 200 *nm* TTC on top of the contacts by molecular beam evaporation (Fig. 6.3 d). The deposition rate was about 4 Å/s and the substrate temperature about 25 °C. Finally, after changing the shadow masks, the hole transistor is capped by a 50 *nm* thick TTC film, acting as top gate dielectric (Fig. 6.3 e). Here, we used an additionally shadow mask which protects the contact pads of the DGTFT. Hence, the total TTC thickness on the contacts is 250 *nm*, assuring the prevention of leakage currents to the electrolyte, and the thickness in the channel region is only 50 *nm*, assuring the high sensitivity of the device. The complete DGTFT is shown in Fig. 6.3 f.

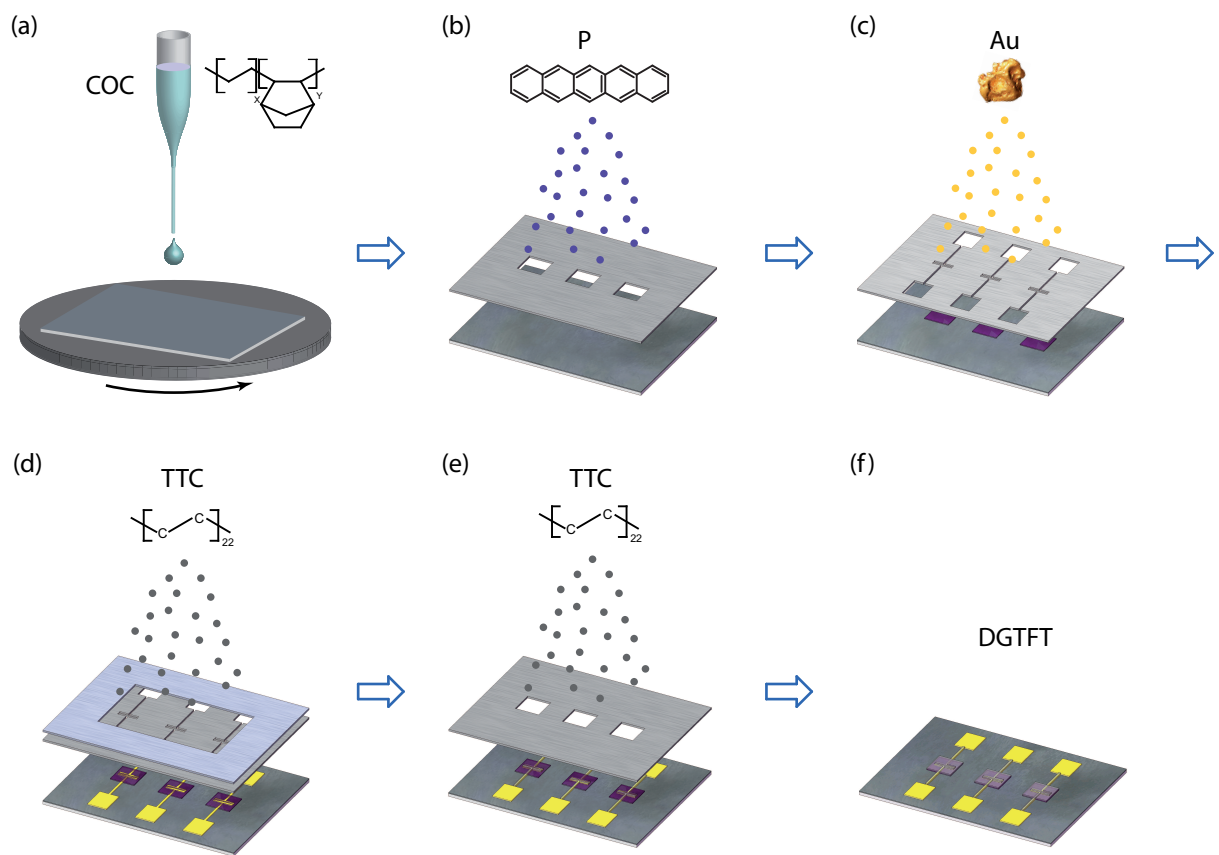


Figure 6.3: Illustration of the fabrication steps of a DGTFT: (a) Spin-coating of the COC layer, (b) evaporation of the pentacene thin film, (c) evaporation of the Au source- and drain contacts, (d) deposition of the TTC capping layer onto the contact area, (e) evaporation of the TTC top dielectric upon the channel area and (f) the finished DGTFT.

6.2 Setup

The main challenge for a precise characterization is given by the simultaneous measurement of at least eight different currents: the current from the electrolyte to the electrode, i.e. to the top-gate, I_{TG} and to the pentacene layer $I_{TG \rightarrow P}$, the currents from the source and the drain contacts to the electrolyte, $I_{S \rightarrow TG}$ and $I_{D \rightarrow TG}$, to the bottom gate contact, $I_{S \rightarrow BG}$ and $I_{D \rightarrow BG}$, to the pentacene layer, $I_{S \rightarrow P}$ and $I_{P \rightarrow D}$. The problem can be simplified by assuming that the ratio $I_{S \rightarrow BG}/I_{D \rightarrow BG}$ is given by ratio of the corresponding potential drops and that $I_{TG \rightarrow P}$ is negligible and therefore $I_{S \rightarrow P} = I_{P \rightarrow D} = I_{S \rightarrow D}$. Furthermore, it is possible to figure out $I_{S \rightarrow TG}$ by setting the drain potential to zero ($I_{S \rightarrow D} = 0$).

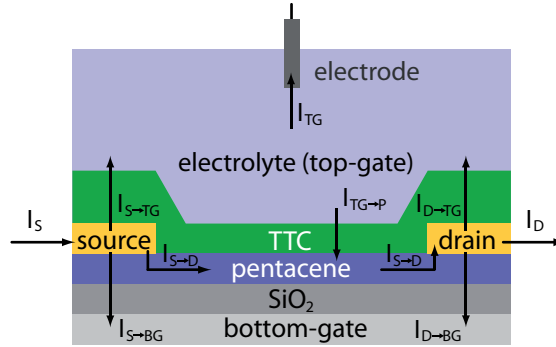


Figure 6.4: Illustration of the currents occurring at a DGTFE transducer device.

The simultaneous use of a Keithley sourcemeter and a potentiostat would allow for a stable control of all voltages and readout of $I_{BG} = I_{S \rightarrow BG} + I_{D \rightarrow BG}$, $I_S = -I_{S \rightarrow D} - I_{S \rightarrow TG} - I_{S \rightarrow BG}$, $I_D = I_{S \rightarrow D} - I_{D \rightarrow TG} - I_{D \rightarrow BG}$ and $I_{TG} = I_{S \rightarrow TG} + I_{D \rightarrow TG}$. For this purpose it is necessary to set the internal ground of the sourcemeter to the ground potential of the potentiostat and control both instruments instantaneously. This was realized with a self written software based on Labview, however it turned out that the ranges of the currents measured by the potentiostat (in the so called bipotentiostat mode) can not be set independently. Additionally, the potentiostat is not suited for the measurement of currents which change by several magnitudes like it is the case for a transfer characteristic of a transistor. Therefore, only one electrode was used and the setting of all potentials and the measurement of all currents were accomplished by two Keithley sourcemeters. The estimation which was used to figure out the change in the source-drain current is given in section 6.3.2.

For the electronic characterization of our DGTFEs we used a self-made measuring station, which allows to fix the sample and contact the source and drain contacts by spring-contacts and the bottom-gate contact by a thin wire. Analogous to the setup used for the measurement of the leakage currents in section 4.2.2 (see Fig. 4.15) we utilized a microfluidic chamber made of PDMS which can be pressed on top of the chip and allows for the introduction of a counter and a reference electrode, see Fig. 6.5. The volume of the microfluidic chamber was about $20 \mu l$ and the contact area to the chip was 0.06 cm^2 .

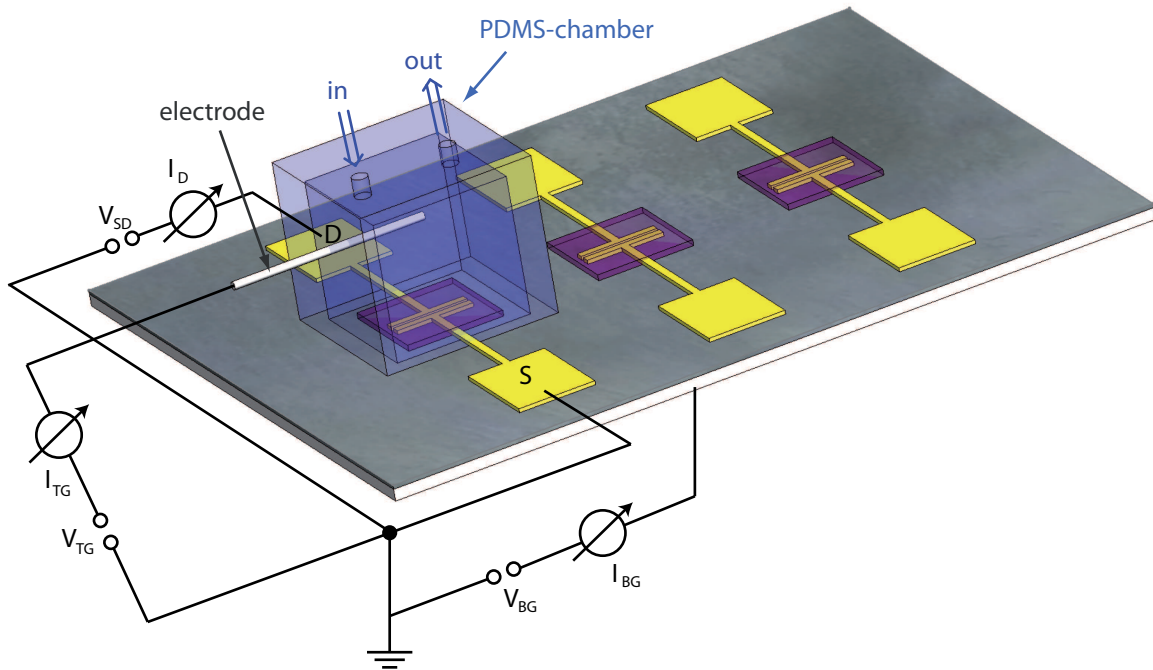


Figure 6.5: Sketch of the setup for the characterization of DGTFTs.

6.3 Stable Operation in Aqueous Ionic Solutions

The most important prerequisite for a transducer device based on a DGTFT is to ensure a stable operation in an ionic aqueous environment. In the first part of this section the operation with a floating electrolyte potential will be discussed. The topic of the second part is the control of the transistor current via the electrolyte potential.

6.3.1 Performance for Floating Electrolyte Potential

A first check how an aqueous environment affects the performance of an uncapped OTFT is to place very carefully a drop of DI water on top of the transistor structure, see Fig. 6.6 a. For top-contact pentacene TFTs we observed that an operation in such an environment is not possible due to large currents between the source and drain contacts through the electrolyte. In contrast, the pentacene layer on the Au contacts of a bottom contact pentacene TFT reduces these currents (compare voltammetry measurements 5.4 b) and allows for a limited operation in DI water. However, we observed a huge hysteresis of the transfer curves and a high offset current (see blue curves in Fig. 6.6 b). The hysteresis probably results from the formation of trap states or the influence of the dipole character of water molecules at the SiO_2 /pentacene interface. As the potential of the DI water is floating also a second channel may occur at the pentacene/water interface due to the mechanism explained in section 3.1.4. The offset current probably results from the leaking currents between the source and drain contact through the electrolyte. Besides the degradation of

pentacene, these effects allowed only for a lifetime between some seconds and a few minutes. After gently removing the water drop the transistor partially regain its performance. The operation in ionic solutions was not possible.

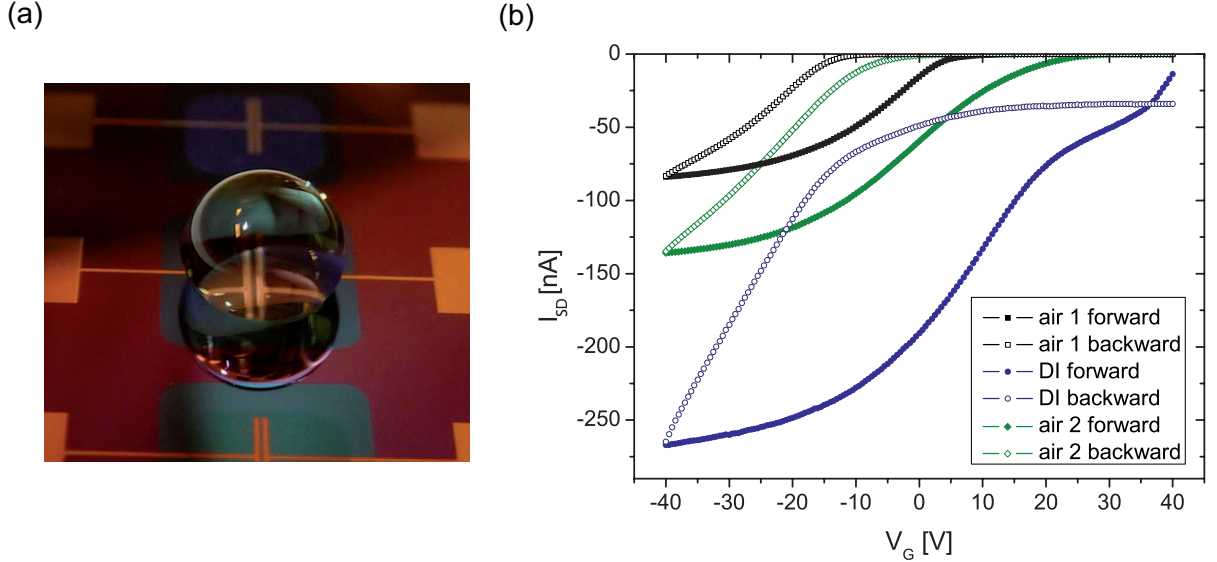


Figure 6.6: (a) Photograph of a DI water drop on a pentacene TFT (b) Transconductance characteristic of an uncapped pentacene TFT in air (air 1), DI water, and in air after removing the water drop (air 2).

In order to show that a thin TTC layer can protect a pentacene TFT from the damaging influence of ionic aqueous solutions, we fabricated a pentacene DGTFET as described above (section 6.1.3). However, for this device the thickness of both, the pentacene film and the TTC layer, was 50 nm and there was no additional capping of the Au contacts. As shown in section 4.2.2 the pentacene thin film structure should be not damaged by the deposition of the TTC layer. This assumption is affirmed by the bottom gate transfer curve of the DGTFET compared to the transfer curve without the TTC layer in ambient conditions at a drain voltage of $V_{SD} = -0.4\text{ V}$ (compare blue and green curve in Fig. 6.7 a). The observation of Jung et al. [86], that the TTC layer enhances the lifetime of pentacene in humid atmosphere explains why the transistor device without the TTC layer on top has a slightly higher off-current and a lower mobility ($\mu^{air} \approx 2 \cdot 10^{-2}\text{ cm}^2/\text{V}$) than the device capped by TTC, see the slopes of the blue and green curve in Fig. 6.7 b. For the deposition of the TTC layer the samples were put in high vacuum and therefore some of the humidity on the device was removed. After the evaporation of TTC the dry state was preserved by the TTC layer. An exact determination of the mobilities is not possible, because the equations for the source-drain current (Eq. 2.31 and 2.34) are imprecise for small drain voltages. After the characterization in ambient conditions we fully immersed the DGTFET in a degassed, aqueous solution of 1 mM NaCl. To measure the performance of the DGTFET under these conditions we used the setup presented in Fig. 6.5 with a platinum electrode at floating potential. The transfer curves in the aqueous ionic solution showed a small in-

crease of the off-current (compare [99]) and a shift towards positive voltages by 3.6 V , see red curves in Fig. 6.7 a and b. in contrast to the uncapped device, the performance of the DGTFT showed a stable performance over many hours and a similar mobility than in ambient conditions. As shown in Fig. 6.7 c the currents to the bottom-gate are nearly unchanged. Thus, the TTC layer also protects the SiO_2 dielectric layer from the influence of ions (see section 4.3). The output curves illustrates that the transistor is in the linear regime for all bottom gate voltages V_G , that for $V_G = 0\text{ V}$ it is possible to operate the DGTFT in the off-mode and that the currents through the electrolyte are negligible, see Fig. 6.7 d.

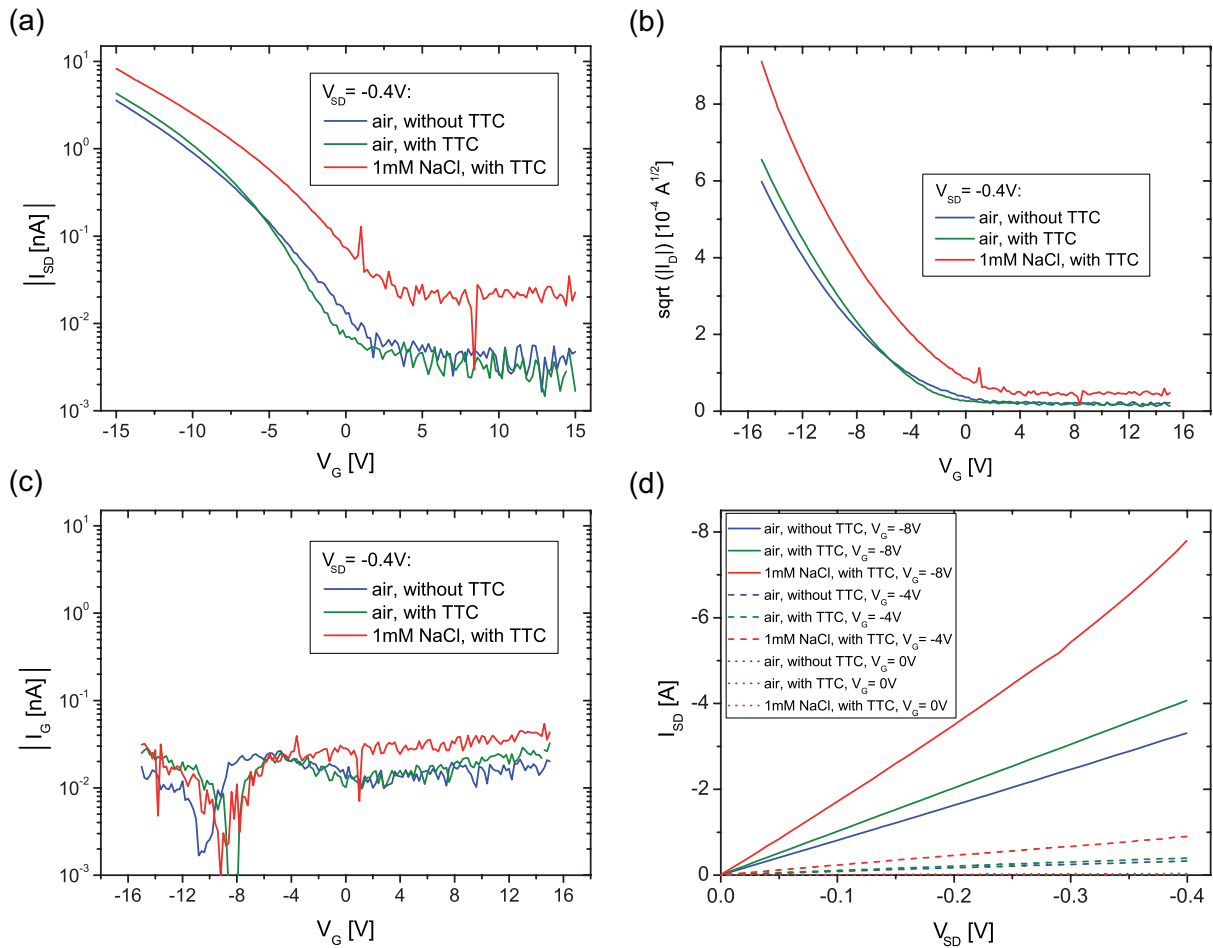


Figure 6.7: Performance of a uncapped pentacene TFT in air, of the same pentacene TFT capped by 50 nm TTC in air and of the capped TFT in 1 mM aqueous NaCl solution: (a) Logarithmic plot of the transconductance curve, (b) square root of the transconductance curve, (c) currents to the gate and (c) conductance characteristic.

We also compared the performance of the DGTFTs in 1 mM NaCl solution with TTC layers evaporated at a low deposition rate (0.1 \AA/s) and with a high deposition rate (4 \AA/s). As expected from the observations made in section 4.2.2 the capping properties of the TTC

layer with a high deposition rate show a superior performance. The detailed results are presented in the supporting information of the publication [100].

6.3.2 Electrolyte Gating of Double-Gate Thin Film Transistors

The next step towards a sensing device is to approve that the electrolyte acts as top-gate and the TTC layer as top-gate dielectric. For this purpose we fabricated DGTFTs as described in section 6.1.3 and used the setup illustrated in section 6.2. As the Na^+ ions seems to reduce the lifetime of the DGTFTs in aqueous environment (see section 4.3) we performed the measurements in a $1\text{ mM } KCl$ solution. Due to the problems caused by the use of a potentiostat we used two Keithley sourcemeters to set the potential at the drain contact (V_{SD}), the bottom gate contact (V_{BG}) and the potential of the electrolyte, i.e. the top-gate, V_{TG} via a Ag/Ag-Cl electrode relative to the source contact, while simultaneously measuring the currents to the drain contact (I_D), the bottom-gate contact (I_{BG}) and to the electrode (I_{TG}), see Fig. 6.5. The source contact was set to ground potential.

The V_{TG} -sweeps at $V_{SD} = -400\text{ mV}$ for floating bottom-gate, $V_{BG} = 0\text{ V}$ and $V_{BG} = -32\text{ V}$ are shown in Fig. 6.8 a. Apparently it is possible to deplete the bottom-gate channel by the top-gate. In agreement with the predictions made in section 2.3.2 the top-gate threshold voltage V_T^t is shifted towards positive values with increasing negative V_{BG} . However, the shift is much smaller than one would expect from Eq. 2.47. This observation can be explained by the dependency of the maximum threshold shift on the depletion width (see Fig. 2.15). It is notable that the threshold voltage of the top-gate V_T^t is very small compared to the threshold voltage of the bottom-gate $V_T^b \approx -23\text{ V}$. This phenomena may result from a much lower concentration of deep traps at the top interface (pentacene/TTC) than at the bottom interface (COC/pentacene). [101]

The output curves in Fig. 6.8 b show that it is possible to operate the DGTFT in all modes described in section 2.11, i.e. double depletion (V_{BG} floating and $V_{TG} = 0\text{ V}$: dashed black line, $V_{BG} = 0\text{ V}$ and $V_{TG} = 0\text{ V}$: dashed blue line), double-accumulation ($V_{BG} = -16\text{ V}$ and $V_{TG} = -0.8\text{ V}$: continuous green line, $V_{BG} = -32\text{ V}$ and $V_{TG} = -0.8\text{ V}$: continuous red line) and the two mixed modes (V_{BG} floating and $V_{TG} = -0.8\text{ V}$: continuous black line, $V_{BG} = 0\text{ V}$ and $V_{TG} = -0.8\text{ V}$: continuous blue line, $V_{BG} = -16$ and $V_{TG} = 0\text{ V}$: dashed green line, $V_{BG} = -32\text{ V}$ and $V_{TG} = 0\text{ V}$: dashed red line).

As leakage currents in the range of 1 nA occurs when the transistor is in the off-state (see Fig. 6.9 a), the transfer curves are corrected as follows: First, we performed a V_{TG} -sweeps at $V_{SD} = 0\text{ V}$ and measured the currents I_D , I_{BG} and I_{TG} . This allows to calculate the current $I_{S \rightarrow TG}$:

$$I_{S \rightarrow TG} = I_{TG} - I_{D \rightarrow TG} \quad (6.1)$$

where $-I_{D \rightarrow TG} = I_D + I_{D \rightarrow BG}$ and $I_{D \rightarrow BG} \approx I_{BG}/2$.

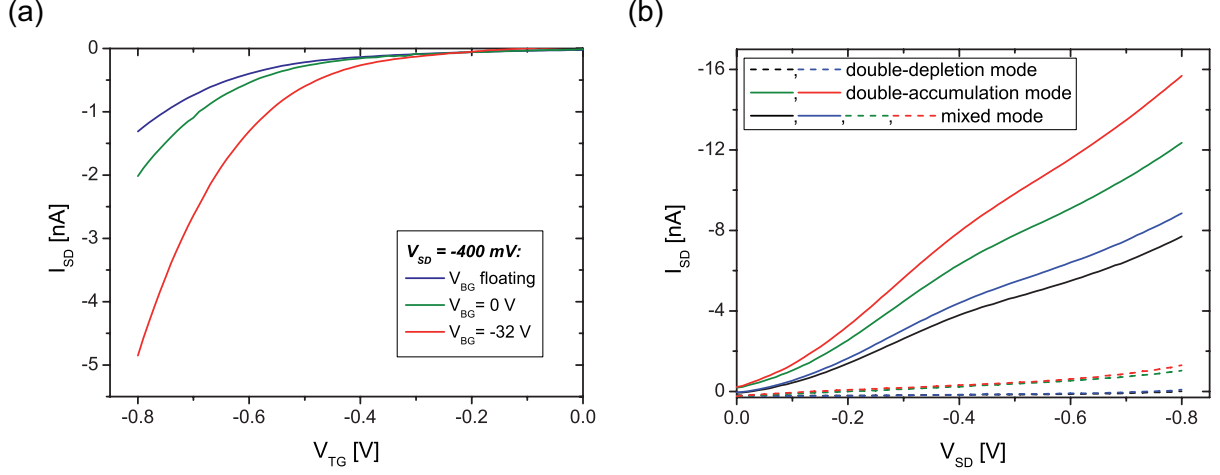


Figure 6.8: Performance of a DGTFT in aqueous ionic environment: (a) V_{TG} -sweeps for floating bottom-gate, for a bottom-gate voltage of $V_{BG} = 0$ V and for $V_{BG} = -32$ V. (b) Output curves for different DGTFT modes.

Assuming that the values yielded for $I_{S \rightarrow TG}$ (see Fig. 6.9 b) are also valid for the V_{TG} -sweeps at $V_{SD} = -400$ mV it is possible to calculate the current from source to drain contact:

$$I_{S \rightarrow D} = I_D + I_{D \rightarrow BG} + I_{D \rightarrow TG} \quad (6.2)$$

where $I_{D \rightarrow BG} \approx I_{BG}/2$ and $I_{D \rightarrow TG} = I_{TG} - I_{S \rightarrow TG}$. We also assumed that the currents from the source to the drain contact through the electrolyte are negligible. Using the currents measured at the electrode I_{TG} (see Fig. 6.9 c) one finally obtains the corrected top-gate transfer curve Fig. 6.9 d. For the output curves the correction is less precisely, what may be the reason for the slightly non-linear behavior in Fig. 6.8 b.

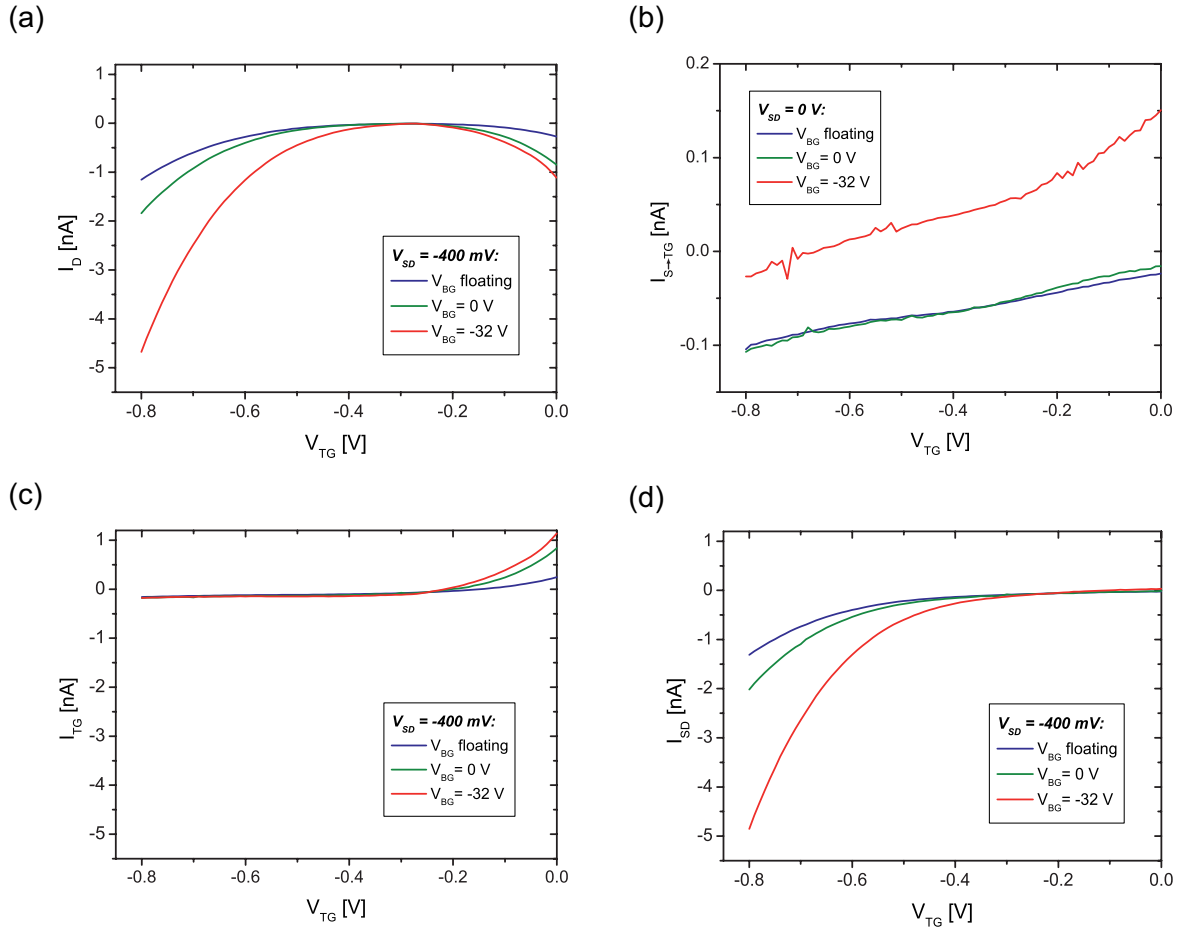


Figure 6.9: (a) Uncorrected measurement of top-gate transfer curve, (b) V_{TG} -sweep and measurement of the drain current from source to the electrode $I_{S \rightarrow TG}$ for $V_{SD} = 0$ V, (c) V_{TG} -sweep and measurement of the top-gate current I_{TG} and (d) corrected measurement of top-gate transfer curve for $V_{SD} = -400$ mV.

6.4 Sensing of Fatty Acid Molecules

The device presented above can be utilized for sensing either by changing the potential of the electrolyte, e.g. by changes in the pH value or by enzymatic reactions, or by the adsorption of charged species at the TTC/electrolyte interface. In both cases the transduction is based on the principle of capacitive coupling. Here, we choose fatty acid molecules to validate the transducer principle. Due to hydrophilic/hydrophobic forces fatty acid molecules readily adsorb to hydrophobic surfaces such as TTC. When the carboxyl group donates a proton to the water molecules ($R - \text{COOH} + \text{H}_2\text{O} \rightarrow R - \text{COO}^- + \text{H}_3\text{O}^+$) the fatty acid molecules carry a single negative net charge. The number of ionized fatty acid molecules depends on the pK_a of the fatty acid and the pH value of the electrolyte via the relation $[R - \text{COO}^-]/[R - \text{COOH}] = 10^{pH - pK_a}$. The pK_a value represents the pH value at which 50% of the hydrogen atoms are removed from the carboxyl groups. It is important to bear in mind that at high concentrations the pK_a value of long chain fatty acids differs from the pK_a value of the carboxyl group (about 4.8) as a result of the formation of aggregates. [102] In this work we use the short chain fatty acid hexanoic acid (HA, $\text{C}_6\text{H}_{12}\text{O}_2$, $pK_a \approx 4.8$) with a solubility of 100 mM and the long chain fatty acid stearic acid (SA, $\text{C}_{18}\text{H}_{36}\text{O}_2$, $pK_a \approx 4.8$ for monomers and $pK_a \approx 10.2$ for aggregates) with a solubility smaller than 1 μM [103]. The advantage in the use of hexanoic acid is that it always occurs in a monomeric state, i.e. the pK_a value is 4.8, and that it is easy to control the concentration. On the other hand, the affinity to adsorb at the TTC interface is smaller than for stearic acid. According to the DGTFT theory (see section 2.3) the change in the threshold voltage resulting from the adsorption of fatty acids is direct proportional to the potential of the top-gate (Eq. 2.52 and Eq. 2.53). However, for making quantitatively conclusions there are two factors which can cause problems. First, it is not always clear which of the two regimes discussed in section 2.3 is valid, i.e. if the threshold voltage of the top interface or the threshold voltage of the bottom interface is applicable. Secondly, the influence of the depletion width strongly affects the magnitude of the threshold voltage shift, see section 2.3.2. The latter phenomena is affirmed by the deviance of the threshold voltage shift in Fig. 6.8 a from the ideal value. Therefore, the quantitative analysis of bottom-gate sweeps to detect changes in the potential of the top-gate is crucial. For this reason, in this section two additional methods will be presented which allow for an alternative use of the DGTFT structure for sensing applications.

6.4.1 Bottom-Gate Voltage Sweep Method

For the quantitative analysis of a threshold voltage shift of a bottom-gate voltage sweep it is important to discriminate the slope originating from the accumulation of holes in the top-channel and the slope resulting from the accumulation of holes at the bottom-interface (compare section 2.3.1). As the top channel of our device opens up at more positive voltages than the bottom-gate voltage, the threshold voltage is given by the voltage one has to apply at the bottom-gate in order to deplete the top channel. Using equation 2.53 and that the change in the top-gate voltage caused by the charged hexanoic acid (HA)

molecules is given by $\Delta V_G^t = qN/C_I^t$, one obtains the following relation for the shift of the threshold voltage:

$$\Delta V_T^b = -\frac{C_P + C_I^b}{C_P C_I^b} \cdot \frac{qN}{A} \quad (6.3)$$

Here, C_P is the capacitance per unit area of the pentacene layer, C_I^t is the capacitance per unit area of the top-gate dielectric ($50 \mu m \times 2000 \mu m$), C_I^b is the capacitance per unit area of the bottom-gate dielectric, A is the area of the active area, q is the charge carried by one adsorbed particle and N is the effective number of charged molecules causing the threshold voltage shift. We demonstrate the principle by the detection of hexanoic acid molecules. For this purpose we prepared a solution of hexanoic acid in phosphate buffered saline (0.1 mM, pH 7.1) with concentrations $c(HA)$ of 0 M, 10 nM, 100 nM and 1 μM . As expected one obtains a threshold voltage shift towards positive voltages with increasing hexanoic acid concentration, see Fig. 6.10.

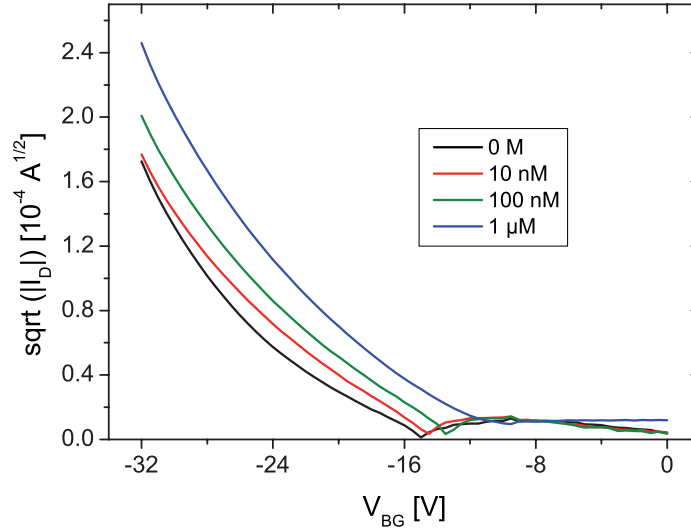


Figure 6.10: Sensing of hexanoic acid by bottom-gate voltage sweep method: V_{BG} -sweep and measurement of the source-drain current I_{SD} for different hexanoic acid concentrations. The source-drain voltage is $V_{SD} = -800 \text{ mV}$ and the top-gate voltage is $V_{TG} = 0 \text{ V}$.

By inserting the observed threshold voltage shift and the capacitances determined by impedance spectroscopy (see section 3.2.5) in Eq. 6.3 one obtains the effective number of charges at the TTC / electrolyte interface contributing to the change in the potential:

$c(HA) [nM]$	$V_T^b [V]$	$N [cm^{-2}]$
0	- 16.2	0
10	- 14.8	$0.9 \cdot 10^{11}$
100	- 13.5	$1.7 \cdot 10^{11}$
1000	- 12.2	$2.6 \cdot 10^{11}$

The result shows that it is possible to achieve concentration sensitivities in the range of 10 nM and therefore in the most relevant detection range for recognition events of biological processes. [16] As typical receptor densities can reach values up to $2 \cdot 10^{12} \text{ cm}^{-2}$ the limit of detection could be further pushed by using an appropriate receptor molecule.

6.4.2 Top-Gate Voltage Sweep Method

A more direct method to detect charged molecules at the TTC interface is to sweep the voltage where the change of potential is occurring, i.e. in this case the potential of the electrolyte. The shift of the threshold due to the adsorption of N charged particles is therefore given by:

$$\Delta V_T^t = -\frac{1}{C_{TTC}} \cdot \frac{qN}{A} \quad (6.4)$$

where q is the charge carried by one adsorbed particle and C_{TTC} is the capacitance of the TTC layer. An advantage of this method is that the bottom-gate voltage V_{BG} can be used to shift the threshold of the top-interface and therefore constitute a very simple way to set the working point of the sensing device to a region of high sensitivity. However, due the small voltage-window it is not always possible to attain an optimal working point.

The described method is demonstrated by measuring a very small quantity of stearic acid (SA) molecules adsorbed at the TTC/electrolyte interface. The stearic acid solution was prepared by adding a sufficient amount of SA to a 1 mM aqueous KCl solution. The solution was put in an ultrasonic bath at 60°C for 15 minutes and after cooling the excess stearic acid material was removed by filtration. Due to the donation of a proton to the water molecules at pH 7 almost all stearic acid molecules in a monomeric state carry a single negative net charge. In agreement to the DGTFT theory, the injection of the SA solution cause a shift of the threshold voltage toward positive voltages (see Fig. 6.11). For the calculation of the effective number of charges at the TTC interface N we compared the transfer curves recorded at $V_{BG} = -32 \text{ V}$, because the transfer curves at a floating bottom-gate or at $V_{BG} = 0 \text{ V}$ do not reach the quadratic regime within the top-gate voltage window. By inserting $C_{TTC} = 2.6 \cdot 10^{-8} \text{ F cm}^{-2}$ for the capacitance of the TTC layer as determined by impedance spectroscopy in section 5.4 and $\Delta V_T^t = 40 \text{ mV}$ in Eq. 6.4 one obtains $N \approx 6.5 \cdot 10^6$ for the number of adhered SA molecules. As the sensing area is $50 \mu\text{m} \times 2000 \mu\text{m}$ this corresponds to $6.5 \cdot 10^9$ SA molecules per cm^2 .

Consequently, a high fraction of the stearic acid molecules must be in the monomeric state and therefore carry negative charge at pH 7.

6.4.3 Drain-Voltage Step Method

A method which also allows sensing operation for imperfect sealed devices is to set fixed potentials at the bottom- and top-gate and apply potential steps to the drain contact. The advantage of this method is that both, the source and the drain contact voltage can set

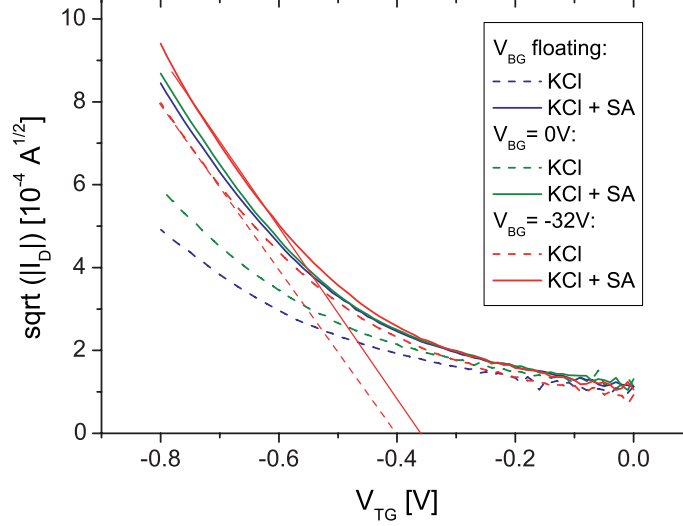


Figure 6.11: Sensing of stearic acid by top-gate voltage sweep method: V_{TG} -sweep and measurement of the source-drain current I_{SD} for a floating bottom-gate, for a bottom-gate voltage of $V_{BG} = 0V$ and for $V_{BG} = -32V$. The transfer curves in pure $1mM$ KCl solution are plotted dashed, the transfer curves after the addition of stearic acid (SA) are plotted continuous. The source-drain voltage was $V_{SD} = -400mV$.

by a potentiostat, while the corresponding currents are measured. After the faradaic and charging currents are decayed (compare section 5.2), the current measured at the drain contact should have the same magnitude as the current measured at the source contact but the opposite sign. For these measurements the bottom gate potential was floating, however analogous to the method described above it should be possible to optimize the sensitivity by applying a suitable voltage to the the bottom gate. As shown in Fig. 6.12 a the transistor we used for this measurement showed an excellent performance in ambient conditions for low source drain voltages ($\mu \approx 0.1 cm^2/(Vs)$) and a very low hysteresis. Analogous to the situation explained above the adhesion of SA molecules causes a shift in the threshold voltage, which, according to Eq. 2.31, is associated to the drain current by the relation

$$\Delta I_{SD} = \frac{W}{L} \mu C_{TTC} \Delta V_T^t \Delta V_{SD} \quad (6.5)$$

where ΔV_{SD} is the step height of the drain potential. Using Eq. 6.4 one obtains for the number of adsorbed SA molecules:

$$N = \frac{\Delta I_{SD} L}{W \mu q \Delta V_{SD}} \quad (6.6)$$

It is remarkable that the change in the current does not depend from the capacitance of the top-gate dielectric C_{TTC} and therefore is not needed for the calculation of N .

The experimental data (see continuous curves in Fig. 6.12 b) for the device presented in Fig. 6.12 a, shows that the change of the currents decreases with increasing V_{SD} (the distances are 2.9 pA for the first step, 2.5 pA for the second step and 2.3 pA for the third step). As it is unlikely that this non-linear behavior is caused by the saturation of I_{SD} the irregularity may be caused by contact effects. Note that due to the difficulty to set the right range in the bipotentiostat mode, there is an offset in the total drain current. As expected the injection of stearic acid solution causes an increase of the drain current I_D (see dashed curves in Fig. 6.12 b). Using Eq. 6.6, $\Delta I_{SD} = 8 \text{ pA}$ (corresponding to -500 mV) and $\mu = 0.1 \text{ cm}^2/(\text{Vs})$ one obtains $N = 125 \cdot 10^6$. This value is much higher than the value yielded with the electrode-voltage sweep method discussed above. This may be caused by the fact that the current I_{SD} does not increase proportional to the threshold voltage ΔV_T when the transfer curves not have yet reached the linear regime. Therefore, the use this method is only reasonable when the setup is calibrated before it is used for sensing.

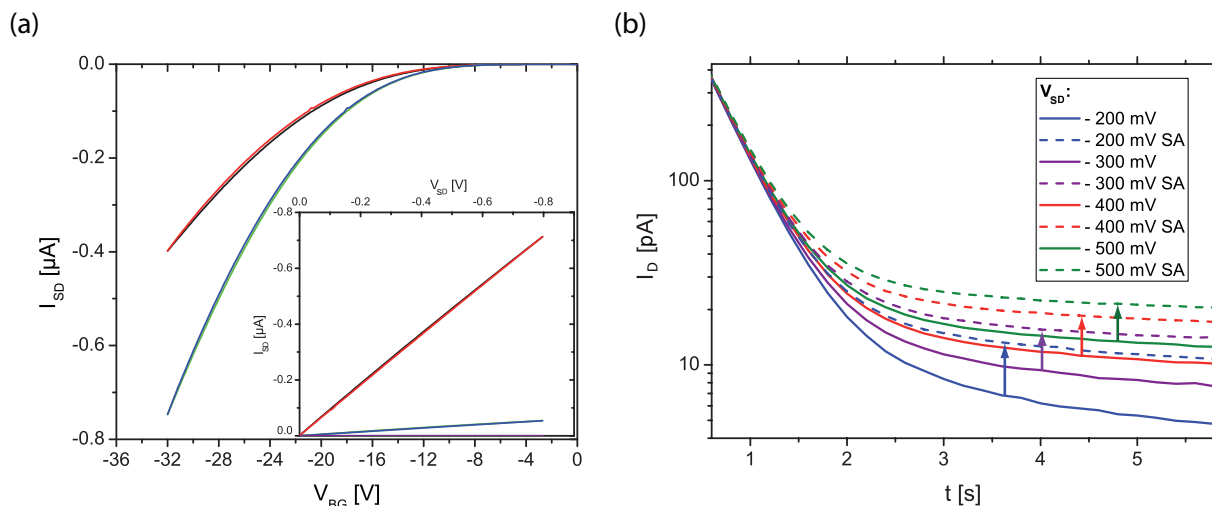


Figure 6.12: (a) Transconductance curve for $V_{SD} = 0.4 \text{ V}$ (red and black curves) and $V_{SD} = 0.8 \text{ V}$ (blue and green curves) of a DGTFT in air. The inset shows the corresponding conductance curves for $V_{BG} = -32 \text{ V}$ (red and black curves), $V_{BG} = -16 \text{ V}$ (blue and green curves) and $V_{BG} = 0 \text{ V}$ (purple curve). (b) Sensing of stearic acid by potential step method. The potential of the Ag/AgCl electrode was set to $V_{TG} = -400 \text{ mV}$

6.4.4 Discussion

The three different methods for using the DGTFT for sensing have shown, that a perfect dielectric layer is not categorical necessary. In fact, the group of Garrido et al. [104] have shown that is possible to gate an α -sexithiophene thin film transistor in an aqueous electrolyte without any top-dielectric layer. It is important to notice that the capacitance of the double layer is not involved in the sensing of molecules adsorbing to the surface. Generally, this approach is suitable to only a limited extent for sensing, because the probability

of charge transfer to the bands or to surface states is very high. Additionally, it is hard to functionalize the semiconductor surface directly. Basically, the interface can be considered as a Schottky diode and therefore such devices work analogous to (normally-off) MESFETs (see [51]). Prerequisite for a successful operation is that the voltage window is situated in the off-state of the characteristic curve of the diode, i.e. the height of the Schottky barrier allows for no charge transfer.

A second interesting aspect is that an insufficient sealing of the top-gate dielectric results in the formation of a MIS-Schottky barrier. Here, the interface can be regarded as a MIS tunnel diode (see [51]) and the influence of the surface states exert a decisive influence on the band bending and the barrier height. Regarding the situation for a MIS-Schottky barrier with an interfacial layer of atomic dimensions as illustrated in Fig. 6.13 a, the general expression for the barrier height $q\phi_{Bp}$ is given by:

$$q\phi_{Bp} = E_g - q(\phi^M + \Delta - \chi^{SC}) - \Delta\phi \quad (6.7)$$

where E_g is the energy gap of the semiconductor, ϕ^M is the work function of the metal, Δ is the potential drop across the interfacial layer, χ^{SC} is the electron affinity of the semiconductor and $\Delta\phi$ is the image force barrier lowering relative to the asymptotic value of the barrier height at zero electric field ϕ_{B0} (compare MS junction in section 2.1.2). In equilibrium the surface-charge density on metal Q_M (marked blue in Fig. 6.13 a) equals the sum of the surface-state charge density Q_{ss} (marked red in Fig. 6.13 a) and the space charge Q_{sc} :

$$Q_M = -(Q_{ss} + Q_{sc}) \quad (6.8)$$

where Q_{ss} is proportional to the density of surface states D_s (see [51] for the exact expression). According to Gauss's law the potential across the interfacial layer is given by $\Delta = -\delta Q_M/\epsilon_I$, where δ is the thickness and ϵ_I is the permittivity of the interfacial layer. For $D_s \rightarrow 0$ one obtains the formula for the ideal Schottky barrier Eq. 2.15 and for $D_s \rightarrow \infty$ one obtains the expression for Fermi-level pinning (see Eq. 2.16). In real devices however the situation lies between these two limits and the barrier height depends on the density of surface states D_s and the thickness of the interfacial layer δ (see [51] for the exact expression). Therefore, the existence of a thin interfacial layer can result in a significant reduction $q\Delta$ of the barrier height. Actually, this effect is utilized for improving the performance of solar cells [105].

In a non-equilibrium state tunnel currents occur from the metal to the conduction band (J_{MC}) and to the valence band (J_{MV}) and vice versa (J_{CM} and J_{VM}), see Fig. 6.13 b. Additionally, there are currents to surface states (J_S). The tunnel currents depend exponentially from the thickness of the interfacial layer δ and cause a splitting of the Fermi level into quasi Fermi levels for holes and electrons (E_F^p and E_F^n). A detailed discussion of this matter is given in the work of Card et al. [106,107]. For sensing applications the tunnel currents and the lowering of the barrier height are very undesirable. Due to reactions with hydrogen, oxygen etc. the formation of a perfect MS junction in liquid environments without any interfacial layer is quite improbable. In conclusion, it is preferable to introduce

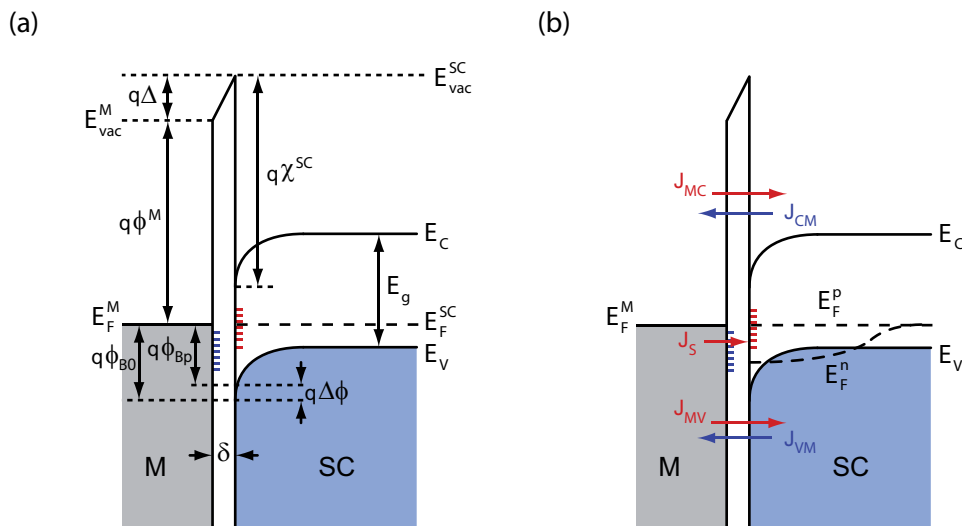


Figure 6.13: (a) Energy band diagram and (b) tunnel currents at a MIS-Schottky barrier.

an insulating layer with good sealing properties, which prevents redox reactions, barrier height lowering or tunnel currents. In order to gain selectivity, the next step towards a sensing device is the functionalization of the interface to the electrolyte.

6.5 Lipid Membranes as a Potential Biofunctionalization Concept

The last step towards a sensor device is to achieve selectivity. Here, our approach is to form a lipid membrane on top of the TTC layer, which allows for a mimicking of the surface structure of a living cell. In the first part of this section we will show that it is possible to establish a fluid and homogeneous lipid membrane on a TTC layer deposited on a pentacene film. The second part illustrates that a DGTFT is sensitive to the formation of a lipid membrane.

6.5.1 Formation of a Lipid Membrane on TTC

For the coating of a stack, consisting of a 50nm pentacene layer and a 20nm TTC film, with a SOPC (1-stearoyl-2-oleoyl-sn-glycero-3-phosphocholine) membrane we used vesicle extrusion. The lipid solution (99.5 mol%) was mixed with labeled TR-DHPE lipids (0.5 mol%) in chloroform, dried in a vacuum oven for four hours and dissolved in a 1 mM aqueous solution of NaCl (1 mg/ml). By extrusion (pore size 100 nm) we produced lipid vesicles. After floating the sample with NaCl solution in a commercial transparent fluidic chamber (μ -Slide I, Ibidi GmbH, Germany), we flushed it with the vesicle solution and incubated for three hours. Finally, in order to remove excess lipids we flushed the chamber several times with NaCl solution. By rinsing with DI-water the remaining vesicles were rup-

tured due to the osmotic pressure, resulting in the formation of a homogeneous lipid layer on the TTC surface. A more precise description of the formation of the lipid membrane can be found in the dissertation of Martin Huth [87], with whom this experiment was arranged.

The properties of the lipid membrane were investigated by fluorescence microscopy. Here, a uniform intensity distribution confirmed a homogeneous coverage. It is not clear if a mono- or a bilayer is formed, however the high hydrophobicity of the TTC film militates in favor of the former. The fluidity of the membrane was analyzed by continuous bleaching, i.e. a circular region the fluorescent dye is bleached by illumination (see Fig. 6.14 a). The diffusion of unbleached fluorophores in the bleached region results in a ring-like region of increased intensity at the outer region (see Fig. 6.14 b). The corresponding intensity profiles are shown in Fig. 6.14 c. The data was analyzed with a Matlab program by Kirstin Fritz [108], which calculates and fits the relative intensities (see Fig. 6.14 d). The program yielded a diffusion constant of $D = 2.6 \pm 0.5 \mu\text{m}^2/\text{s}$, what is in good agreement with the diffusion constant measured on TTC layers directly deposited on SiO_2 [87]. In conclusion, the continuous bleaching experiment verified that it is possible to form a homogeneous and fluid lipid membrane on a pentacene/TTC stack, i.e. the surface which is relevant for the active area of a DGTFT sensor.

6.5.2 Sensing of a Lipid Membrane by a DGTFT Transducer

The next step is to investigate the influence of a lipid membrane on the DGTFT performance. We chose a SOPC membrane, which bear a small negative charge [109]. For this purpose we operated a DGTFT with floating top-gate and performed bottom-gate sweeps at $V_{SD} = -0.8 \text{ V}$. Here, the use of Si_3N_4 substrates resulted in a threshold voltage close to zero ($+0.51 \text{ V}$ in 1 mM NaCl solution, see black curve in Fig. 6.15). After flushing the sample with a SOPC vesicle solution, which was produced in the same way described above, the threshold shifted towards negative voltages by 0.81 V (see blue curve in Fig. 6.15). In order to form a lipid membrane we rinsed the chamber with DI-water. After flushing one last time with the NaCl solution, the transfer curve has shifted back to more positive voltages (threshold voltage $+0.33 \text{ V}$, see green curve in Fig. 6.15). Note that the transistor open up more early and then cross the black curve at about -3.18 V . This behavior can be explained by the two threshold regimes discussed in section 2.3.2. Therefore, the threshold determined by a linear fit of the curve between $V_G = -4 \text{ V}$ and $V_G = -6 \text{ V}$ can be assigned to the bottom-interface threshold V_T^b . Assuming that the top gate voltage originating from the charge Q is given by $V_G^t = Q/C_I^t$, Eq. 2.47 yields:

$$Q = \frac{C_I^b(C_{SC} + C_I^t)}{C_{SC}} V_T^b \quad (6.9)$$

Using the capacitances resulting from the impedance measurements in section 5.4 and a threshold voltage shift of $V_T^b = 0.18 \text{ V}$ one obtains a charge of $Q = 3.2 \cdot 10^{-8} \text{ As} \cdot \text{cm}^{-2}$, i.e. $N \approx 2.0 \cdot 10^8$ charges in the active area. Taking into account that the area of one SOPC lipid in a bilayer is about 67 \AA^2 [110, 111] one obtains the number of charges per lipid is

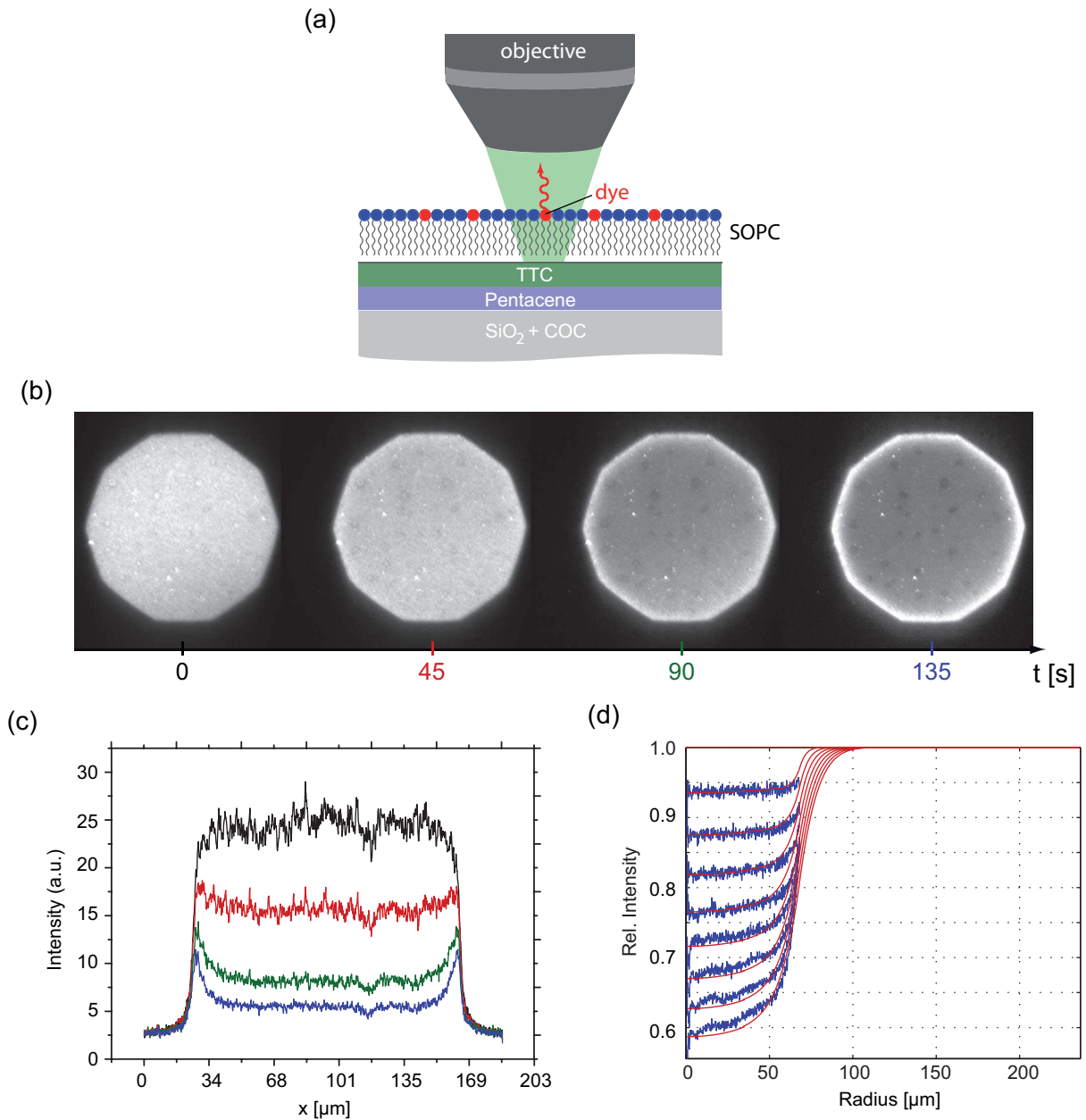


Figure 6.14: Determination of the diffusion constant by continuous bleaching: (a) Sketch of the setup. (b) Captures after 0, 45, 90 and 135 seconds of illumination. (c) shows the corresponding intensity profiles and (d) shows the plots of the relative intensity (blue), which fits (red) were used for the determination of the diffusion constant.

1/748. The result is in good agreement with the values obtained by Pincet et al. [109] and suggests that a monolayer is formed at the TTC interface. This is in accordance with the common assumption that lipids tend to form monolayers on highly hydrophobic surfaces.

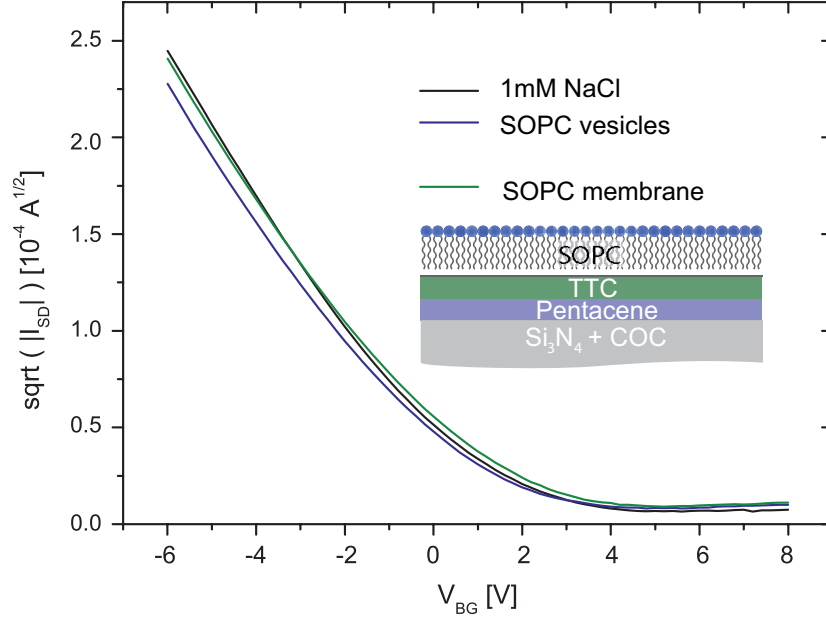


Figure 6.15: Influence of lipid membrane formation on DGTFT transfer curve: Measurement of the bottom gate transfer curves in 1 *mM NaCl* solution (black curve), in a SOPC vesicle solution (blue curve) and after flushing with DI-water and refilling with 1 *mM NaCl* solution (green curve).

In summary, we have shown that a pentacene DGTFT with an alkane top dielectric in aqueous ionic solution is capable to detect very small quantities of charges adsorbing to the interface. Additionally, we propose the functionalization of the device by a lipid membrane. In this line we have shown that it is possible to establish a homogeneous and fluid SOPC membrane on the active area of a DGTFT, and that this event results in a small but measurable change in the threshold voltage.

Chapter 7

Conclusion and Outlook

The scope of this work was to realize a transducer method for biosensing applications, which basically rests on the principle of an organic double-gate transistor. Although this device is well understood in inorganic semiconductor physics, the theory for organic double-gate transistors is mostly limited to qualitative considerations so far. Hence, the first challenge was to transfer the existing theory of double-gate transistors working in the inversion regime to organic devices working in the accumulation regime. We succeeded in formulating quantitative expressions for the threshold voltage for all operation modes of a DGTFT, which are in agreement with the more qualitative predictions of other groups. Additionally, we showed that the depletion width exerts a decisive influence on the maximum threshold voltage shift. This finding is very important for the interpretation of organic double-gate transistors and was neglected in most works to date.

To utilize the device for biosensing applications, it is inevitable to ensure a stable operation in biological relevant environments, e.g. blood. In this line, we showed that a 50 nm thin layer of the alkane tetratetracontane allows for a good passivation of the organic semiconductor pentacene in aqueous ionic solution and has the capability to act as a top gate dielectric. Deposited by molecular beam evaporation, tetratetracontane forms highly ordered layers. However, the sealing properties strongly depend on deposition parameters like the evaporation rate and the substrate temperature. We investigated the growth of tetratetracontane on the relevant substrates for a wide range of parameters with atomic force microscopy, x-ray reflectometry, contact angle and current-voltage measurements. The most smooth and dense layers are obtained at a high deposition rate (4 Å/s) and a low substrate temperature (about room temperature).

To understand the electronic characteristics of an organic sensor device in an aqueous ionic environment the electrochemical behavior of organic materials is of significant importance. We investigated the electrochemistry of the organic semiconductor pentacene and of the top-gate dielectric tetratetracontane by transient and cyclic voltammetry measurements. The results show that the commonly observed degradation of pentacene in humid environments supposable arises from the formation of dihydropentacene and that a charge transfer

between the electrolyte and the valence band of pentacene is probable. A passivation of pentacene by tetratetracontane results in a significant decrease of the diffusion constant of the reactants and therefore efficiently suppresses the charge transfer and degradation of pentacene. We verified these findings and determined the capacitances of the pentacene and the alkane layer by impedance spectroscopy. The latter is of decisive importance for the quantitative interpretation of the signal of the transducer device.

Next, we verified the transducer principle of a pentacene double-gate transistor. For this purpose, we controlled the source-drain current by setting the potential of the electrolyte via an electrode. Applying a voltage to the electrolyte makes it possible to switch the transistor between the off- and the on-state, while the threshold voltage can be adjusted by the bottom gate voltage. The high sensitivity of the device was demonstrated by detecting very small quantities of fatty acid molecules, which adsorb at the alkane/electrolyte interface.

Finally, we propose a new approach to gain selectivity of the discussed sensor device by forming a lipid membrane on top of the alkane layer. We demonstrated that it is possible to establish a homogeneous and fluid lipid membrane on the active area of the sensor device by fluorescence microscopy and continuous bleaching technique. The shift of the threshold voltage, resulting from the small negative charge of the membrane, indicates that the lipids form a monolayer.

In future experiments one may achieve a functionalization of the transducer device e.g. by embedding anchors for certain proteins in the lipid membrane. Possibly, the sensing concept may permit the combination of the high sensitivity of conventional detection methods like ELISA with the fast analysis time of capacitive coupling. Another exciting vision is to detect action potentials of living cells. Here, the fluidity of the lipid membrane would allow for a closer contact to the cell. In order to realize in vivo measurements it is highly desirable to aspire a fully organic device, i.e. to use flexible, biodegradable substrates and bottom-gate dielectrics.

Bibliography

- [1] D. Heyers, M. Manns, H. Luksch, O. Güntürkün, and H. Mouritsen. A visual pathway links brain structures active during magnetic compass orientation in migratory birds. *PLOS ONE*, 2(9):e937, 2007.
- [2] W. Broad. It's sensitive. Really. *New York Times, Science Times, December, 13*, 2005.
- [3] H. Scheich, G. Langer, C. Tidemann, R. B. Coles, and A. Guppy. Electoreception and electrolocation in platypus. *Nature*, 30(6052):401, 1986.
- [4] L. Buck and R. Axel. A novel multigene family may encode odorant receptors: A molecular basis for odor recognition. *Cell*, 65(1):175, 1991.
- [5] L. C. Clark. Monitor and control of blood and tissue oxygen tensions. *ASAIO Transactions*, 2:41, 1956.
- [6] L. C. Clark and C. Lyons. Electrode systems for continuous monitoring in cardiovascular surgerys. *Ann. N.Y. Acad. Sci.*, 102(1):29, 1962.
- [7] M. Irimia-Vladu, N. S. Sariciftci, and S. Bauer. Exotic materials for bio-organic electronics. *J. Mater. Chem.*, 21(5):1350, 2011.
- [8] P. Heiduschka and S. Thanos. Implantable bioelectronic interfaces for lost nerve functions. *Prog. in Neurobiol.*, 55(5):433, 1998.
- [9] T. Sekitani, U. Zschieschang, H. Klauk, and T. Someya. Flexible organic transistors and circuits with extreme bending stability. *Nat. Mater.*, 9(12):1015, 2010.
- [10] D. Feili, M. Schuettler, T. Doerge, S. Kammera, and T. Stieglitz. Encapsulation of organic field effect transistors for flexible biomedical microimplants. *Sens. Actuators, B*, 120(1):101, 2005.
- [11] J. A. Rogers, T. Someya, and Y. Huang. Materials and mechanics for stretchable electronics. *Nat. Mater.*, 327(5973):1603, 2010.
- [12] E. Bystrenova, M. Jelital, I. Tonazzini, A. N. Lazar, M. Huth, P. Stoliar, C. Dionigi, M. G. Cacace, B. Nickel, E. Madarasz, and F. Biscarini. Neural networks grown on organic semiconductors. *Adv. Funct. Mater.*, 18(12):1751, 2008.

-
- [13] G. Scarpa, A. Idzko, S. Götz, and S. Thalhammer. Biocompatibility studies of functionalized regioregular poly(3-hexylthiophene) layers for sensing applications. *Macromol. Biosci.*, 10(4):378, 2010.
- [14] C. R. Lowe. Biosensors. *Trends Biotechnol.*, 2(3):59, 1984.
- [15] S. P. J. Higson, S. M. Reddy, and P. M. Vadgama. Enzyme and other biosensors: Evolution of a technology. *Eng. Sci. Educ. J.*, 3(1):41, 1994.
- [16] J. L. Arlett, E. B. Myers, and M. L. Roukes. Comparative advantages of mechanical biosensors. *Nat. Nanotechnol.*, 6(4):203, 2011.
- [17] G. Zeck and P. Fromherz. Noninvasive neuroelectronic interfacing with synaptically connected snail neurons immobilized on a semiconductor chip. *Proc. Natl. Acad. Sci. U. S. A.*, 98(18):10457, 2001.
- [18] D. Grieshaber, R. MacKenzie, J. Vörös, and E. Reimhult. Electrochemical biosensors - sensor principles and architectures. *Sensors*, 8(3):1400, 2008.
- [19] C. J. Bettinger and Z. Bao. Organic thin-film transistors fabricated on resorbable biomaterial substrates. *Adv. Mater.*, 22(5):651, 2010.
- [20] C. J. Bettinger and Z. Bao. Biomaterials-based organic electronic devices. *Polym. Int.*, 59(5):563, 2010.
- [21] U. Lange, N. V. Roznyatouskaya, and V. M. Mirsky. Conducting polymers in chemical sensors and arrays. *Anal. Chim. Acta*, 614(1):1, 2008.
- [22] M. Gerad, A. Chaubey, and B. D. Malhotra. Application of conducting polymers to biosensors. *Biosens. Bioelectron.*, 17(5):345, 2001.
- [23] H. Muguruma, Y. Shibayama, and Y. Matsui. An amperometric biosensor based on a composite of single-walled carbon nanotubes, plasma-polymerized thin film, and an enzyme. *Biosens. Bioelectron.*, 32(6):827, 2008.
- [24] U. Yogeswaran and S. M. Chen. A review on the electrochemical sensors and biosensors composed of nanowires as sensing material. *Sensors*, 8(1):290, 2008.
- [25] D. A. Bernardis, D. J. Macaya, M. Nikolou, J. A. DeFranco, S. Takamatsu, and G. G. Malliaras. Enzymatic sensing with organic electrochemical transistors. *J. Mater. Chem.*, 18(1):116, 2007.
- [26] E. Bakker and E. Pretsch. Potentiometric sensors for trace-level analysis. *Trends Anal. Chem.*, 24(3):199, 2005.
- [27] A. J. Bard and L. R. Faulkner. *Electrochemistry at Metal and Semiconductor Electrodes*, 2nd ed. John Wiley and Sons Inc.

- [28] P. Bergveld. Thirty years of ISFETOLOGY What happened in the past 30 years and what may happen in the next 30 years. *Sens. Actuators, B*, 88(1):1, 2003.
- [29] M. J. Schöning and A. Püoghossian. Recent advances in biologically sensitive field-effect transistors (BioFETs). *Analyst*, 127(9):1137, 2002.
- [30] S. Caras and J. Janata. Field effect transistor sensitive to penicillin. *Anal. Chem.*, 52(12):1935, 1980.
- [31] M. Voelker and P. Fromherz. Signal transmission from individual mammalian nerve cell to field-effect transistor. *Small*, 1(2):206, 2005.
- [32] H. U. Khan, M. E. Roberts, W. Knoll, and Z. Bao. Pentacene based organic thin film transistors as the transducer for biochemical sensing in aqueous media. *Chem. Mater.*, 23(7):1946, 2011.
- [33] M. J. Spijkman, J. J. Brondijk, T. C. T. Geuns, E. C. P. Smits, T. Cramer, F. Zerbetto, P. Stoliar, F. Biscarini, P. W. M. Blom, and D. M. de Leeuw. Dual-gate organic field-effect transistors as potentiometric sensors in aqueous solution. *Adv. Funct. Mater.*, 20(6):898, 2010.
- [34] W. Zhang and G. Li. Third-generation biosensors based on the direct electron transfer of proteins. *Anal. Sci.*, 20(4):603, 2004.
- [35] A. Voller, A. Bartlett, and Bidwell D. E. Enzyme immunoassays with special reference to elisa techniques. *J. Clin. Pathol.*, 31(6):507, 1978.
- [36] B. B. Haab. Applications of antibody array platforms. *Curr. Opin. Biotechnol.*, 17(4):415, 2006.
- [37] K. Jans, K. Bonroy, R. De Palma, G. Reekmans, H. Jans, W. Laureyn, M. Smet, G. Borghs, and G. Maes. Stability of mixed PEO-thiol SAMs for biosensing applications. *Langmuir*, 24(8):3949, 2008.
- [38] T. Ahujaa, I. A. Mira, D. Kumara, and Rajesh. Biomolecular immobilization on conducting polymers for biosensing applications. *Biomaterials*, 28(5):791, 2007.
- [39] S. N. Kim, J. F. Rusling, and F. Papadimitrakopoulos. Carbon nanotubes for electronic and electrochemical detection of biomolecules. *Adv. Mater.*, 19(20):3214, 2007.
- [40] J. M. Pingarron, P. Yanez-Sedeno, and A. Gonzalez-Cortes. Gold nanoparticle-based electrochemical biosensors. *Electrochim. Acta*, 53(19):5848, 2008.
- [41] A. D. Howard, G. McAllister, S. D. Feighner, Q. Liu, R. P. Nargund, L. H. T. Van der Ploeg, and A. A. Patchett. Orphan G-protein-coupled receptors and natural ligand discovery. *Trends Pharmacol. Sci.*, 22(3):132, 2001.

- [42] I. Czolkos, A. A. Jesorka, and O. Orwar. Molecular phospholipid films on solid supports. *Soft Matter*, 7(10):4562, 2011.
- [43] M. Tanaka and E. Sackmann. Polymer-supported membranes as models of the cell surface. *Nature*, 437(7059):656, 2005.
- [44] S. Gritsch, P. Nollert, F. Jähnig, and E. Sackmann. Impedance spectroscopy of porin and gramicidin pores reconstituted into supported lipid bilayers on indium-tin-oxide electrodes. *Langmuir*, 14(11):3118, 1998.
- [45] C. Steinem, A. Janshoff, W. P. Ulrich, M. Sieber, and H. J. Galla. Impedance analysis of supported lipid bilayer membranes: a scrutiny of different preparation techniques. *Biochim. Biophys. Acta, Biomembr.*, 1279(2):169, 1996.
- [46] E. Sackmann. Quantal concept of t-cell activation: adhesion domains as immunological synapses. *New J. Phys.*, 13:065013, 2011.
- [47] D. Braun and P. Fromherz. Fluorescence interferometry of neuronal cell adhesion on microstructured silicon. *Phys. Rev. Lett.*, 81(23):5241, 1998.
- [48] Y. Huang, P. V. Palkara, L. Li, H. Zhangb, and P. Chena. Integrating carbon nanotubes and lipid bilayer for biosensing. *Biosens. Bioelectron.*, 25(7):1834, 2010.
- [49] S. Hunklinger. *Festkörperphysik, 2. Aufl.* Oldenburg Verlag, München, 2009.
- [50] A. Rose. Space-charge-limited currents in solids. *Phys. Rev.*, 97(6):1538, 1955.
- [51] S. M. Sze. *Physics of Semiconductor*. John Wiley and Sons Inc., New York, 1981.
- [52] N. Sato. *Electrochemistry at Metal and Semiconductor Electrodes*. Elsevier Science and Technology, Amsterdam, 1998.
- [53] G. Horowitz. Organic field-effect transistors. *Adv. Mater*, 10(5):365, 1998.
- [54] C. D. Dimitrakopoulos and D. J. Masearo. Organic thin-film transistors: A review of recent advances. *IBM J. Res. and Dev.*, 45(1):11, 2001.
- [55] A. R. Brown, C. P. Jarrett, D. M. de Leeuw, and M. Matters. Field-effect transistors made from solution-processed organic semiconductors. *Synth. Met.*, 88(1):37, 1997.
- [56] G. Hadziioannou and P. F. van Hutten. *Semiconducting Polymers*. Wiley-VCH, New York, 2000.
- [57] W. Deng, X. Zheng, R. Chend, and Y. Liu. Subthreshold characteristics of polysilicon TFTs. *Solid-State Electron.*, 52(5):695, 2008.
- [58] C. Erlen and P. Lugli. Analytical model of trapping effects in organic thin-film transistors. *IEEE Trans. El. Dev.*, 56(4):546, 2009.

- [59] H.-K. Lim and J. G. Fossum. Threshold voltage of thin-film silicon-on-insulator (soi) MOSFET's. *IEEE Trans. El. Dev.*, 30(10):1244, 1983.
- [60] F. Maddalena, M. Spijkman, J. J. Brondijk, P. Fonteijn, F. Brouwer, J. C. Hummelen, D. M. de Leeuw, P. W. M. Blom, and B. de Boer. Device characteristics of polymer dual-gate field-effect transistors. *Org. Electron.*, 9(5):839, 2008.
- [61] L. L. Chua, Friend. R. H., and K. H. H. Ho. Organic double-gate field-effect transistors: Logic-AND operation. *Appl. Phys. Lett.*, 87(25):253512, 2005.
- [62] M. Schwörer and H. C. Wolf. *Organische Molekulare Festkörper*. Wiley-VCH, Weinheim, 2005.
- [63] G. R. Desiraju and A. Gavezzotti. Crystal structures of polynuclear aromatic hydrocarbons. classification, rationalization and prediction from molecular structure. *Acta Cryst.*, 45(5):473, 1989.
- [64] K. Hannewald, V. M. Stojanovic, Schellekens J. M. T, P. A. Bobbert, G. Kresse, and J. Hafner. Theory of polaron bandwidth narrowing in organic molecular crystals. *Phys. Rev. B*, 69(7):075211, 2004.
- [65] W. Warta, R. Stehle, and N. Karl. Ultrapure, high mobility organic photoconductors. *Appl. Phys. A-Mater. Sci. Process.*, 36(3):163, 1985.
- [66] W. Shockley and W. T. Read. Statistics of the recombinations of holes and electrons. *Phys. Rev.*, 87(5):835, 1952.
- [67] D. C. Hoesterey and G. M. Letson. The trapping of photocarriers in anthracene by anthraquinone, anthrone and naphthacene. *J. Phys. Chem. Solids*, 24(12):1609, 1963.
- [68] H. Baessler. Charge transport in disordered organic photoconductors a monte carlo simulation study. *Phys. Status Solidi B*, 175(1):15, 1993.
- [69] A. D. McNaught and A. Wilkinson. *IUPAC. Compendium of Chemical Terminology*, 2nd ed. Blackwell Scientific Publications.
- [70] P. A. Sterne and J. C. Inkson. Exchange-correlation potential in semiconductors and insulators. *J. Phys. C: Solid State Phys.*, 17(9):1497, 1984.
- [71] H. Gerischer and W. Mindt. The mechanisms of the decomposition of semiconductors by electrochemical oxidation and reduction. *Electrochim. Acta*, 13(6):1329, 1968.
- [72] A. R. Murphy and J. M. J. Frechet. Organic semiconducting oligomers for use in thin film transistors. *Chem. Rev.*, 107(4):1066, 2007.

- [73] V. M. Kenkre. Finite-bandwidth calculations for charge carrier mobility in organic crystals. *Phys. Lett. A*, 305(6):443, 2002.
- [74] N. Koch, A. Vollmer, I. Salzmann, B. Nickel, H. Weiss, and J. P. Rabe. Evidence for temperature-dependent electron band dispersion in pentacene. *Phys. Rev. Lett.*, 96:156803, 2006.
- [75] J. Lee, S. S. Kim, K. Kim, J. H. Kim, and S. Im. Correlation between photoelectric and optical absorption spectra of thermally evaporated pentacene films. *Appl. Phys. Lett.*, 84(10):1701, 2004.
- [76] P. G. Schroeder, C. B. France, J. B. Park, and B. A. Parkinsona. Energy level alignment and two-dimensional structure of pentacene on Au 111 surfaces. *J. Appl. Phys.*, 91(5):823, 2002.
- [77] A. Troisi and G. Orlandi. Charge-transport regime of crystalline organic semiconductors: Diffusion limited by thermal off-diagonal electronic disorder. *Phys. Rev. Lett.*, 96:086601, 2006.
- [78] K. Gmucova, M. Weis, M. Della Pirriera, and J. Puigdollers. A comparative study of hydrogen- and hydroxyl-related pentacene defect formation in thin films prepared by Langmuir-Blodgett technique and thermal evaporation. *Phys. Status Solidi A*, 206(7):1404, 2009.
- [79] J. E. Northrup and M. L. Chabinye. Gap states in organic semiconductors: Hydrogen- and oxygen-induced states in pentacene. *Phys. Rev. B*, 68:041202, 2003.
- [80] Z. Zhu, J. T. Mason, R. Dieckmann, and G. G. Malliaras. Humidity sensors based on pentacene thin-film transistors. *Appl. Phys. Lett.*, 81(24):4643, 2002.
- [81] B. Nickel, M. Fiebig, S. Schiefer, M. Göllner, M. Huth, C. Erlen, and P. Lugli. Pentacene devices: Molecular structure, charge transport and photo response. *Phys. Status Solidi A*, 205(3):526, 2008.
- [82] S. Schiefer, M. Huth, A. Dobrinevski, and B. Nickel. Determination of the crystal structure of substrate-induced pentacene polymorphs in fiber structured thin films. *J. Am. Chem. Soc.*, 129(34):10316, 2007.
- [83] D. Käfer, L. Ruppel, and G. Witte. Growth of pentacene on clean and modified gold surfaces. *Phys. Rev. B*, 75(8):085309, 2007.
- [84] J. Fenrych, E. C. Reynhardt, and I. Basson. Temperature dependence of the structures of solution-grown and melt-grown samples of n-hexatetracontane. *Powder Diff.*, 12(1):49, 1997.
- [85] Ed: R. C. Weast. *Handbook of Chemistry and Physics*, 55 th ed. CRC Press, Cleveland Ohio, 1974.

- [86] H. Jung, T. Lim, Y. Choi, M. Yi, J. Won, and S. Pyo. Lifetime enhancement of organic thin-film transistors protected with organic layer. *Appl. Phys. Lett.*, 92(16):163504, 2008.
- [87] M. Huth. *X-ray and neutron scattering study of organic-organic heterolayers for organic electronics and biointerfaces*. Dissertation, Ludwig-Maximilians-Universität München, Germany, 2010.
- [88] S. R. Craig, G. P. Hastie, K. J. Roberts, and J. N. Sherwood. Investigation into the structures of some normal alkanes within the homologous series C₁₃H₂₈ to C₆₀H₁₂₂ using high-resolution synchrotron X-ray powder diffraction. *J. Mater. Chem.*, 4(6):977, 1994.
- [89] S. C. Nyburg and J. A. Potworowski. Prediction of unit cells and atomic coordinates for the n-alkanes. *Acta Cryst.*, 29(2):347, 1973.
- [90] B. Hille. *Ionic Channels of Excitable Membranes*. Sinauer Associates Inc., Massachusetts, 1992.
- [91] C. R. Wilke and P. Chang. Correlation of diffusion coefficients in dilute solutions. *AIChE J.*, 1(2):264, 1955.
- [92] J. Heinze. Cyclovoltammetrie die Spektroskopie des Elektrochemikers. *Angew. Chem.*, 96(11):823, 1984.
- [93] L. D. Burke and P. F. Nuget. The electrochemistry of gold: I the redox behaviour of the metal in aqueous media. *Gold Bullet.*, 30(2):43, 1997.
- [94] L. D. Burke and P. F. Nuget. The electrochemistry of gold: II the electrocatalytic behaviour of the metal in aqueous media. *Gold Bullet.*, 31(2):39, 1998.
- [95] M. J. Nicol. The anodic behaviour of gold part I - Oxidation in acidic solutions. *Gold Bullet.*, 13(2):46, 1980.
- [96] M. J. Nicol. The anodic behaviour of gold part II - Oxidation in alkaline solutions. *Gold Bullet.*, 13(3):105, 1980.
- [97] V. Chakrapani, J. C. Angus, A. B. Anderson, S. D. Wolter, B. R. Stoner, and G. U. Sumanasekera. Charge transfer equilibria between diamond and an aqueous oxygen electrochemical redox couple. *Science*, 318(5855):1424, 2007.
- [98] M. Fiebig. *Spatially resolved electronic and optoelectronic measurements of pentacene thin film transistors*. Dissertation, Ludwig-Maximilians-Universität München, Germany, 2010.
- [99] D. Li, E. Borkent, R. Nortrup, H. Moon, H. Katz, and Z. Bao. Humidity effect on electrical performance of organic thin-film transistors. *Appl. Phys. Lett.*, 86(4):042105, 2005.

-
- [100] M. Göllner, M. Huth, and B. Nickel. Pentacene thin-film transistors encapsulated by a thin alkane layer operated in an aqueous ionic environment. *Adv. Mater.*, 22(39):4350, 2010.
- [101] M. Fiebig, D. Beckmeier, and B. Nickel. Thickness-dependent in situ studies of trap states in pentacene thin film transistors. *Appl. Phys. Lett.*, 96(8):083304, 2010.
- [102] J. R. Kanicky and D. O. Shah. Effect of premicellar aggregation on the pKa of fatty acid soap solutions. *Langmuir*, 19(6):2034, 2003.
- [103] P. Khuwijitjaru, Y. Kimura, R. Matsuno, and S. Adachi. Solubility of oleic and linoleic acids in subcritical water. *Food Sci. Technol. Res.*, 10(3):261, 2004.
- [104] F. Buth, D. Kumar, M. Stutzmann, and J. A. Garrido. Electrolyte-gated organic field-effect transistors for sensing applications. *Appl. Phys. Lett.*, 89(15):153302, 2011.
- [105] H. C Card and E. S. Yang. MIS-Schottky theory under conditions of optical carrier generation in solar cells. *Appl. Phys. Lett.*, 29(1):51, 1976.
- [106] H. C Card and E. H. Rhoderick. Studies of tunnel MOS diodes I. Interface effects in silicon schottky diodes. *J. Phys. D: Appl. Phys.*, 4(10):1589, 1971.
- [107] H. C Card and E. H. Rhoderick. Studies of tunnel MOS diodes II. Thermal equilibrium considerations. *J. Phys. D: Appl. Phys.*, 4(10):1602, 1971.
- [108] K. Fritz. *unpublished*. Dissertation, Ludwig-Maximilians-Universität München, Germany, 2011.
- [109] F. Pincet, S. Cribier, and E. Perez. Bilayers of neutral lipids bear a small but significant charge. *Eur. Phys. J. B*, 11(1):127, 1999.
- [110] A. I. Greenwood, J. Pan, T. T. Mills, J. F. Nagle, R. M. Epand, and S. Tristram-Nagle. CRAC motif peptide of the HIV-1 gp41 protein thins SOPC membranes and interacts with cholesterol. *Biochim. Biophys. Acta*, 1778(4):1120, 2008.
- [111] B. W. Koenig, H. H. Strey, and K. Gawrisch. Membrane lateral compressibility determined by NMR and X-ray diffraction: Effect of acyl chain polyunsaturation. *Biophys. J.*, 73(4):1954, 1997.

Publications

- *Pentacene devices: Molecular structure, charge transport and photo response*
B. Nickel, M. Fiebig, S. Schiefer, M. Göllner, M. Huth, C. Erlen, P. Lugli
Phys. stat. sol. (a) **205**, no. 3, 526 (2008)
- *Spatially Resolved Photoresponse Measurements on Pentacene Thin-Film Transistors*
M. Fiebig, C. Erlen, M. Göllner, P. Lugli, B. Nickel
Applied Physics A: Organic Materials for Electronic Applications **95**, no. 1, 113 (2009)
- *Pentacene thin film transistors encapsulated by a thin alkane layer operated in an aqueous ionic environment*
M. Göllner, M. Huth, B. Nickel
Advanced Materials **22**, no. 39, 4350 (2010)
- *Aquatic - paraffin coated - pentacene transistors for biosensing*
M. Göllner, M. Huth, B. Nickel
Photon science highlights, DESY (2011)
- *An Electrochemical Transducer based on a Pentacene Double-Gate Thin-Film Transistor*
M. Göllner, G. Glasbrenner, B. Nickel
Electroanalysis **24**, no. 2, 214 (2012)

Danksagung

Ich möchte mich herzlich bei allen bedanken die mich bei der Verwirklichung dieser Arbeit unterstützt haben. Mein besonderer Dank gilt

Prof. Dr. Joachim Rädler und dem gesamten Lehrstuhl für die Möglichkeit meine Arbeit in einem so angenehmen Umfeld durchführen zu dürfen.

PD Dr. Bert Nickel für seine kompetente Betreuung und die Möglichkeit an einem internationalen Projekt mitwirken zu dürfen. Deine Geduld und Gelassenheit haben sehr zum Gelingen dieser Arbeit beigetragen.

Prof. Dr. Fabio Biscarini und allen Mitgliedern des BIODOT Projektes, für die fachübergreifende Zusammenarbeit und den interessanten Meetings.

Prof. Dr. Jörg Kotthaus und dessen Lehrstuhl für die Möglichkeit zur Nutzung des Reinraums.

Dr. Martin Huth für die exzellente und unterhaltsame Zusammenarbeit.

Dr. Matthias Fiebig für seine Unterstützung und die Einführung in wissenschaftliches Arbeiten.

Georg Glasbrenner für die harmonische Zusammenarbeit, sein großes Engagement und die gemeinsamen Feierabende.

Der gesamten **Arbeitsgruppe Nickel**, insbesondere Christian Westermeier für seine guten Ratschläge und Hilfsbereitschaft.

Dr. Susi Kempter und **Gerlinde Schwake** für ihre Fürsorge, Geduld und Toleranz.

Stefan Manus für seine Hilfe bei elektronischen Messaufbauten.

Philipp Altpeter für seine qualifizierte Hilfestellung bei Reinraumangelegenheiten.

Dr. David Fermin für die erhellenden Gespräche auf dem Gebiet der Elektrochemie und die Möglichkeit in seinem Labor arbeiten zu dürfen.

Simon Noever für gutes Essen und für seine Freundschaft.

Meinen Eltern für ihre bedingungslose Unterstützung.

Lebenslauf

Martin Göllner

geboren am 19.10.1980 in München

Schulbildung

1987 - 1991	Besuch der Volksschule Oberpfammern
1991 - 2001	Besuch des Gymnasium Ottobrunn

Hochschulbildung

10/2001 - 8/2006	Physik-Studium an der Ludwig-Maximilians-Universität München
8/2006 - 8/2007	Diplomarbeit am Lehrstuhl für Experimentalphysik der LMU München bei Prof. Dr. J. O. Rädler
ab 10/2007	Promotion am Lehrstuhl für Experimentalphysik der LMU München bei PD Dr. B. Nickel